A DETAILED CHANDRA X-RAY STUDY OF THE GALACTIC CORE-COLLAPSE SUPERNOVA REMNANT G292.0+1.8

by

JAYANT BHALERAO

Presented to the Faculty of the Graduate School of
The University of Texas at Arlington in Partial Fulfillment
of the Requirements for the Degree of

DOCTOR OF PHILOSOPHY

THE UNIVERSITY OF TEXAS AT ARLINGTON
August 2018

Supervising Committee:

Dr. Sangwook Park, Supervising Professor

Dr. Manfred Cuntz

Dr. Yue Deng

Dr. Zdzislaw Musielak

Dr. Qiming Zhang

To my parents.

And to my family.

"The nitrogen in our DNA, the calcium in our teeth, the iron in our blood, the carbon in our apple pies were made in the interiors of collapsing stars. We are made of starstuff." – Carl Sagan

ACKNOWLEDGEMENTS

I am deeply grateful to Professor Sangwook Park for making all of this possible, and for his exceptional scientific guidance, unfailing support, patience and encouragement throughout this thesis process.

I thank all my colleagues, past and present, at UTA. I particularly thank Doctors Andrew Schenck, Seth Post, Carola Ellinger, Neslihan Alan and Zhaopeng Wang, and my present colleagues Matthew Millard and Aravind Pazhayath for valuable discussions, advice, support, and encouragement.

A special note of thanks to Dr. Daniel Dewey for providing priceless insight into the art and science of astronomy. I thank our scientific collaborators, Professor John P. Hughes, Professor Koji Mori and Dr. Jae-Joon Lee for their valued contributions.

I especially thank my committee members at UTA, Professors Manfred Cuntz, Yue Deng, Zdzislaw Musielak and Qiming Zhang for their support, encouragement, guidance and for providing such wonderful learning opportunities.

I thank Professor Kaushik De and Dr. Mark Sosebee for access to the superb computing resources of the UTA High Energy Physics Group.

I would like to thank Professor Alex Weiss and the UTA physics department for their constant support, encouragement and for a learning environment that made such a big difference in my life. I thank UTA for outstanding, unfailing support in every possible way and for a learning experience I will value forever.

I thank the Texas Space Grant Consortium for their support. I also thank members of the Chandra X-ray Center and MIT HETG technical support groups. This work was supported in part by the Smithsonian Astrophysical Observatory (SAO) through *Chandra* grant GO1-12077X.

28 August 2018

ABSTRACT

A DETAILED CHANDRA X-RAY STUDY OF THE GALACTIC CORE-COLLAPSE SUPERNOVA REMNANT G292.0+1.8

Jayant Bhalerao, Ph.D.

The University of Texas at Arlington, 2018

Supervising Professor: Dr. Sangwook Park

In this thesis, we describe our detailed analysis of the core-collapse supernova remnant (CCSNR) G292.0+1.8 (G292 hereafter) using data collected by NASA's *Chandra* X-ray Observatory (*Chandra*). In the first part of this thesis, we use data collected by *Chandra's* grating spectrometer to study the motion of the SNR's ejecta. We study this motion by measuring Doppler shifts of atomic spectral emission lines. We measure the radial velocities (v_r) of 33 emission features in the remnant. We find that the ejecta have high v_r ($-2300 \lesssim v_r \lesssim 1400$ km s^{-1}). We also find that most of the ejecta are moving towards us (17 of the 24 ejecta knots have negative or blueshifted v_r). This asymmetry in the kinematic structure of the ejecta gas may have originated from an asymmetric SN explosion. Based on our measured v_r-distribution, we qualitatively locate the positions of the reverse shock (RS) and contact discontinuity (CD). We analyze the dynamics of the remnant using theoretical models, and estimate a total ejecta mass of $\lesssim$8 M$_\odot$. Considering the previously estimated mass of the circumstellar medium (CSM), we place an upper limit of $\lesssim$35 M$_\odot$ on the mass of the G292 progenitor star.

In the second part of this thesis, we analyze the chemical composition and physical properties of G292 in detail. We use data from a long exposure (∼530 ks) of G292 collected using *Chandra's* ACIS-I detector. We use our adaptive mesh method to divide the remnant into 2147 smaller rectangular regions. We analyze the emission from each of these regions by extracting spectra, and fitting these spectra with a model appropriate for shocked, hot ionized SNR gas. Based on our model fits we identify ∼1400 *ejecta-dominated* regions and ∼700 *CSM-dominated* regions. The spatial distribution of the *CSM-dominated* regions reveals the structure and morphology of the shock-heated CSM in G292. We create maps revealing the detailed spatial distribution of the abundances of O, Ne, Mg, Si, S and Fe, the absorbing column (N_H), and the plasma physical parameters: electron temperature (kT), ionization timescale ($n_e t$), and the electron density (n_e), and thermal pressure (P). For the first time, we detect and localize the Fe-rich ejecta in G292 using *Chandra* data. We find that the O-, Ne-, Mg-rich ejecta are preferentially expelled in the NW-SE direction. On the other hand, the heavier inner ejecta, represented by the elements Si, S and Fe, are almost exclusively found in the northwestern hemisphere with hardly any in the southeast. This suggests that the heavier ejecta in G292 were expelled in the opposite direction to which the associated pulsar (PSR J1124-5916) was presumably kicked. We provide the first observational evidence that Fe, a key explosive nucleosynthesis product, was ejected opposite to the neutron star in G292. Also, for the first time in X-rays, we identify the northern component of the equatorial ring, a dense, bright, ring-like CSM structure that runs east-west along the remnant's "equator." From our analysis of the dynamics of the remnant, our measured elemental abundance ratios, and calculated masses of the ejecta and CSM, we estimate a G292 progenitor mass of 13–30 $M_\odot$.

TABLE OF CONTENTS

ACKNOWLEDGEMENTS iv

ABSTRACT vi

LIST OF ILLUSTRATIONS xi

LIST OF TABLES xiii

Chapter Page

1. INTRODUCTION 1

1.1 A Universe of Stars 1

1.2 Explosion Mechanisms of Supernovae 3

1.3 Classification of Supernovae 5

1.4 Core-Collapse Mechanism: Open Questions 7

1.5 Neutron Star Kicks 8

1.6 Supernova Remnants 8

1.7 Evolution of Supernova Remnants 9

1.8 Core-Collapse Supernova Remnants 12

1.9 Galactic Core-Collapse Supernova Remnant G292.0+1.8 13

1.10 The *Chandra* X-ray Observatory 15

1.10.1 The X-ray Telescope 15

1.10.2 The Science Instruments 16

1.11 Data Processing and Analysis Methods 18

1.11.1 Data and software 18

1.11.2 Spectral Analysis 18

1.12 Thesis Composition 20

REFERENCES 21
2. X-Ray Ejecta Kinematics of the Galactic Core-Collapse Supernova Remnant G292.0+1.8 34
2.1 ABSTRACT 35
2.2 INTRODUCTION 35
2.3 OBSERVATIONS & DATA REDUCTION 37
2.4 ANALYSIS & RESULTS 38
2.5 DISCUSSION 42
2.6 SUMMARY 48
REFERENCES 50
3. Detailed X-ray Mapping of the Shocked Ejecta and Circumstellar Medium in the Galactic Core-Collapse Supernova Remnant G292.0+1.8 61
3.1 ABSTRACT 62
3.2 INTRODUCTION 63
3.3 OBSERVATIONS & DATA REDUCTION 66
3.4 ANALYSIS & RESULTS 67
3.4.1 Characterization of the Outermost Shocked CSM 67
3.4.2 Origin of the Regional Emission (Ejecta vs. CSM) 68
3.4.3 Spatial Distribution of the Elemental Abundances and NEI Plasma Parameters 70
3.4.4 Fe-Rich Emission Regions 71
3.5 DISCUSSION 73
3.5.1 Spatial Structure of Ejecta Elements and NEI Plasma Parameters 73
3.5.2 Ejecta Mass 76
3.5.3 Properties of the CSM 78
3.5.4 Ejecta Asymmetry in the Remnant 81

3.5.5 Progenitor Mass 84
3.6 SUMMARY & CONCLUSIONS 87
REFERENCES 89
4. Summary & Conclusions 118

LIST OF ILLUSTRATIONS

Figure Page

1.1 Stellar evolution 29

1.2 SNR Structure 30

1.3 G292 RGB Image 31

1.4 The *Chandra* X-ray Observatory 32

1.5 Advanced CCD Imaging Spectrometer(ACIS) 33

2.1 HETG spectrum 56

2.2 Gaussian model fits 57

2.3 Radial velocity distribution 58

2.4 Image: measured radial velocities 59

2.5 PWN image 60

3.1 Adaptive mesh image 102

3.2 Example ACIS spectra 103

3.3 Elemental abundance maps 105

3.4 Elemental abundance ratio maps 106

3.5 NEI plasma parameter maps 107

3.6 Radial profiles 108

3.7 Fe K shell-line regions 109

3.8 Example Fe L complex spectrum 110

3.9 Detected Fe K emission line 111

3.10 Fe K line center energy 112

3.11 Spatial divisions of the SNR 113

3.12 Ejecta mass fractions - hemispheres 114
3.13 Ejecta mass fractions - combined quadrants 115
3.14 Abundance ratio plots 116
3.15 Ejecta yield plots 117

LIST OF TABLES

Table		Page
2.1	Emission Lines used for Doppler Shift Measurements	53
2.2	Radial Velocities of X-ray Emission Features in G292.0+1.8	54
2.2	Radial Velocities of X-ray Emission Features in G292.0+1.8	55
3.1	*Chandra* Observations of G292	95
3.2	Average CSM Abundances	96
3.3	Line and Continuum Energy Ranges for the EWI Images	97
3.4	Estimated Ejecta Masses	98
3.5	Estimated CSM Masses	99
3.6	Average Ejecta Abundances	100
3.7	Estimated Ejecta Masses - Shell Regions	101

CHAPTER 1

INTRODUCTION

1.1 A Universe of Stars

We live in a universe with billions of galaxies, each galaxy flush with billions of stars (e.g., Conselice et al. 2016). These stars may harbor one or more planets, and planetary systems like our own may be quite common. Stars and planets are formed from gas and dust, which are other constituents of the visible universe. As humans, we therefore wonder: how did life originate on Earth, and is there life elsewhere in the universe? Through advances made in astronomy, we learn that supernovae (SNe, spectacular stellar explosions) are key players in the history of life (e.g., Hester & Desch 2005; Boss 2017a, b).

SNe are powerful forces that shape the universe (e.g., Mac Low et al. 2005). The universe began with about 75% hydrogen, 25% helium and traces of lithium, beryllium and boron (Frebel & Norris 2015). From this primordial gas, the first generation of stars were born (Population III stars). Feedback from stars as they evolve and release their nuclear-fusion products into the environment, enriches the universe with heavier elements or "metals." Gas and dust enriched with metals made by the Population III stars subsequently formed the next generation of stars (Population II stars). The process continues to form the most metal-rich stars, such as our Sun (Population I stars) (Karlsson et al. 2013; Nomoto et al. 2013).

SNe are stellar endpoints, they mark the deaths of certain types of stars. They are among the most spectacular, violent and energetic explosions in the universe. A SNe typically releases $\sim 10^{53}$ ergs of gravitational potential energy during the

explosion. Most of this energy is carried away by neutrinos. About 10^{51} ergs of this energy becomes the kinetic energy of the exploded material, ($\sim 10^{51}$ ergs is defined as the unit of 1 Bethe or 1 B). Material from the blast can reach speeds of $\sim$30,000 km s^{-1} (approaching the speed of light, e.g., Alsabti & Murdin 2017, p. 17). About 10^{50} ergs of the gravitational potential energy can be imparted to cosmic rays (e.g., Vink 2012), and $\sim 10^{49}$ ergs is converted to light (e.g., Branch & Wheeler 2017, p. 9). This extraordinary amount of luminous energy is responsible for a typical SN luminosity of 10^{43} ergs s^{-1} or $\sim 10^{9}$ $L_{\odot}$, released over the period of about a month (e.g., Maoz 2007, pp 85-88). During this brief period, the SN can outshine its entire host galaxy.

During a supernova, elements created by the star by nuclear fusion (hydrostatic nucleosynthesis products) and elements synthesized by the intense energy of the explosion (explosive nucleosynthesis products) are released into interstellar space (e.g., Nomoto et al. 2013, Thielemann et al. 2018). These elements enrich the interstellar medium, from which the next generation of stars and planets form (e.g., Nittler & Ciesla 2016). Shock waves produced by SN explosions can trigger the collapse of clouds of gas and dust leading to the birth of new stars and planets (e.g., Herbst & Assousa 1977; Balazs et al. 2004; Boss 2017a). The heavy elements that constitute our bodies, such as the Ca in our bones and the Fe in our blood, originate from SNe.

Although our knowledge of SNe has increased over the past century, numerous questions remain. In this thesis, we provide new insights into the properties of an important type of SN and its remnant (a supernova remnant or SNR is what remains after the SN explosion, see Section 1.6). The SNR we study in this thesis is called G292.0+1.8 (G292 hereafter). We start, in this chapter, with a brief introduction to the field. We also introduce our topic, so as to provide a perspective on its usefulness in addressing some of these open questions.

1.2 Explosion Mechanisms of Supernovae

The term supernova was first proposed by Baade and Zwicky (1934a), who also suggested that they were explosions of stars as they transformed to neutron stars (Baade & Zwicky 1934b). Hoyle and Fowler (1960) first identified two different mechanisms for stellar explosions: core-collapse, and the ignition of degenerate stellar material. Currently there are several suggested mechanisms for SNe explosions:

i) Core-collapse SNe (CCSNe): stars on the main sequence withstand the inward pull of gravity through gas and radiation pressure generated by the hydrostatic nuclear burning of hydrogen in the stellar core. Massive stars, those with a zero-age main sequence mass (ZAMS) of more than eight times the mass of our Sun ($\gtrsim$ 8 $M_{\odot}$), consume hydrogen fuel at a rapid rate and deplete their reserves of core hydrogen in a few $\sim$10 to 100 million years. Energy production is sustained by the successive burning of heavier elements in the core and its overlying shells. When Fe is formed in the core, further nuclear fusion consumes energy rather than produces it, and the energy balance begins to favor gravity. When the mass of the Fe-core exceeds the Chandrasekhar mass ($\sim$ 1.4 M $_{\odot}$) it collapses under the force of gravity. The inner core ($\sim$0.4-0.6 M$_{\odot}$) is squeezed to nuclear densities ($\gtrsim 2\times10^{14}$ g cm^{-3}) (e.g., Couch 2017). At this point neutron degeneracy pressure kicks in and the the inner core stiffens and rebounds. The rebound sends a shock wave through the in-falling outer core setting the stage for a SN explosion. The details of what causes a successful explosion are not fully understood. The shock wave is believed to stall a few milliseconds after bounce because of energy losses to neutrinos and photodisintegration (the break up of nuclei by radiation, e.g., Bethe 1994). Neutrinos escaping from the proto-neutron star (PNS) formed in the inner core, and carrying $\gtrsim 3\times10^{53}$ ergs of gravitational energy released during the core's collapse, are thought to re-energize the shock wave so that it eventually blows apart the outer layers of the star in a spectacular SN

explosion (Bethe & Wilson 1985; Bethe 1994). The compressed iron core can collapse into a neutron star (NS) if it has a mass of about 1.4-3 $M_{\odot}$, or a black hole if its mass exceeds $\sim$3 $M_{\odot}$ (e.g., reviews by Woosley & Weaver 1986; Burrows 2000; Woosley & Janka 2005; Couch 2017) (Fig. 1.1).

Stars in the ZAMS mass range of 8–12 $M_{\odot}$ may explode as electron capture SNe (ECSNe) instead of iron-collapse CCSNe as discussed above. When these stars evolve off of the main sequence, before O-burning (that leads to Si-production and the formation of an iron core) takes place, a degenerate O + Ne + Mg core is formed instead. Electrons are captured on ^{24}Mg and ^{20}Ne in this degenerate core, which leads to loss of pressure. The reduced pressure in the core cannot withstand gravity, and the core collapses. This collapse is followed by a SN explosion, in which a NS may be formed. This explosion mechanism may have been responsible for the Crab SN and SN 1054 (Miyaji et al. 1980; Nomoto 1984; Woosley & Heger 2015; Doherty et al. 2017; Branch & Wheeler 2017, pp. 188-189; Foglizzo 2017, p. 1059).

ii) Thermonuclear SNe: stars with ZAMS $\lesssim$ 8 $M_{\odot}$, after running out of hydrogen fuel in the core, evolve off of the main sequence into red giants. During the red giant phase, energy is generated by helium core-burning and hydrogen shell-burning. After helium is exhausted in the core, the star is not massive enough to produce the temperatures required for fusing the heavier carbon and oxygen nuclei ($T \sim 6{\times}10^8$ K). The star transitions to an asymptotic giant branch star (AGB star), and burns helium and hydrogen in shells surrounding the core. The star eventually loses its outer layers to form a planetary nebula, while the core contracts and cools to form a white dwarf (WD, e.g., Iben & Renzini 1983; Iben 1985; Herwig 2005). The WD typically consists of carbon and oxygen and is supported by electron degeneracy pressure (e.g, Hillebrandt & Niemeyer 2000). An alternate way in which a WD may be

formed is through mass-loss of the aging star to a binary companion. When WDs accrete material, for example from nearby stellar companions, they may reach the Chandrasekhar limit (1.4 $M_{\odot}$), undergo runaway nuclear fusion within their degenerate interiors, and explode. The explosion may be mediated by a supersonic shock wave (called a *detonation*), or by subsonic combustion (called a *deflagration*), or by a combination of the two. The explosion is believed to destroy the entire star with no compact object left behind (e.g., reviews by Hillebrandt & Niemeyer 2000; Branch & Wheeler 2017, pp. 437-481; Ropke 2017, pp. 1185-1209).

iii) Pair instability SNe (PISN): this explosion mechanism is proposed for stars with ZAMS $\gtrsim$ 100 $M_{\odot}$ (e.g., Heger & Woosley 2002; Chatzopoulos & Wheeler 2012; Branch & Wheeler 2017, p. 15). When these very massive stars run out of hydrogen fuel in their cores, helium burning follows. This leads to the formation of a degenerate oxygen-rich core. The large mass of the star creates extremely high temperature within this degenerate core. At these high temperatures, electron-positron pairs are created from gamma rays. This results in reduced pressure in the core and causes it to contract. Contraction causes the temperature in the core to rise further, which leads to explosive oxygen burning and a thermonuclear explosion that completely destroys the star. Pair instability SNe may have been more common among massive Population III stars in the early universe (e.g., Woosley et al. 2002; Langer 2012; Branch & Wheeler 2017, p. 15 & pp. 211-218; Kozyreva et al. 2018).

1.3 Classification of Supernovae

As described above, SNe are generally classified into two main categories: core-collapse supernovae (CCSN) and thermonuclear supernovae. In addition to this theoretical classification based on their explosion mechanism, SNe are also classified based

on their observed spectra and light curves. SNe that show hydrogen absorption lines are classified at Type II SNe, while those that do not are classified as Type I. Type II SNe are subdivided into several sub-classes depending on their spectra, and the shapes of their light curves. The light curves of Type IIP SNe show a plateau phase that follows the peak of the light output. During the plateau phase, the light output remains constant for about 3 months. This phase is powered by the release of energy deposited by the SN blast wave into the H-rich envelope, and by the decay of radioactive elements such as ^{56}Co (e.g., Arcavi 2017, pp. 239-276). Type IIL SNe have light curves that show a linear decline in time. Type IIb SNe have linearly declining light curves, but they exhibit a transitional nature since their spectra change over time from those resembling hydrogen-rich Type II SNe to those resembling helium-rich Type Ib SNe (e.g., Taubenberger et al. 2011). Type IIn SNe are a subclass characterized by narrow emission lines. These emission lines may originate from dense circumstellar material lost by the progenitor star. The explosion mechanism leading to Type IIn SNe is not clear (e.g., Schlegel 1990; Vink 2012). Type II superluminous SNe (SLSNe) are a new class of exceptionally bright SNe with hydrogen in their spectra, and luminosities that may reach 100$\times$ that of a typical SN (Gal-Yam 2012). The origin of these SLSNe is not clear. Type IIP, IIL and IIb SNe are core-collapse SNe. SNe similar to SN 1987A (with light curves that show a long steady rise for $\sim$80 days) are classified as 87A-likes (for reviews see Minkowski 1941; Filippenko 1997; Vink 2012; Branch & Wheeler 2017, pp. 6-8; Zampieri 2017; Arcavi 2017, pp. 239-276).

Type I SNe can result from stars that have lost their outer layers and contracted to form WDs, or from stars that have lost their hydrogen-rich envelope through stellar winds and/or binary interactions (Podsiadlowski et al. 1992). The thermonuclear explosions of white dwarfs are classified as Type Ia SNe, and their spectra show the

presence of Si absorption lines. Type I SNe that do not show the presence of hydrogen or Si absorption lines are CCSNe, and they are classified as Type Ib (if they show He absorption lines) or Type Ic (if they do not show He absorption lines) (Filippenko 1997; Branch & Wheeler 2017, pp. 6-8).

1.4 Core-Collapse Mechanism: Open Questions

The details of the CCSN explosion are not fully understood (e.g., Vink 2012; Burrows 2013; Burrows et al. 2018). Some of the open questions are:

(1) Why is there a standard explosion energy of $\sim 10^{51}$ ergs, with a generally observed range of 10^{50-52} ergs?

(2) Escaping neutrinos, accretion instabilities, acoustic power, and amplified magnetic fields are believed to contribute towards a successful explosion. What makes for a successful explosion, and what causes the explosion mechanism to fail?

(3) What mechanisms produce remnants of different types such as neutron stars and black holes, and how do they relate to the properties of the progenitor star?

(4) What are the nucleosynthesis yields of the elements formed during hydrostatic burning before the explosion, and those that are formed during the explosion itself through explosive nucleosynthesis?

(5) What are the mechanisms leading to the observed high transverse velocities of pulsars ($\sim$350–1000 km s^{-1}) and what is the role of asymmetry in the explosion?

(6) What is the relation between asymmetry in the explosion and the structure and morphology of the resulting SNR? Can the spatial distributions of the ejecta and shock-heated CSM inform about asymmetries in the explosion?

1.5 Neutron Star Kicks

NSs can be created from the collapsed cores of massive stars during the CCSN explosion (see Section 1.2). NSs have been observed with transverse velocities of up to ~ 1000 km s^{-1} (Chatterjee et al. 2005). This motion is believed to originate from forces (or "kicks") imparted to the NS during the explosion (Lai 2001). Numerical simulations indicate that NS-kicks are caused by the gravitational pull of slower-moving inner ejecta resulting from an asymmetric SN explosion (Scheck et al. 2006; Wongwathanarat et al. 2013; 2017). During such an explosion, most of the inner, heavier ejecta (produced by explosive nucleosynthesis) are expelled in the direction opposite to that in which the NS is kicked. This "anti-alignment" between the NS and the innermost ejecta has been observed in the remnants of several CCSN (Holland-Ashford et al. 2017; Katsuda et al. 2018).

1.6 Supernova Remnants

The direct observational study of SNe is limited by several factors: i) SNe are rare events for a given galaxy, occurring every 35 years or so in a spiral galaxy like our Milky Way Galaxy. ii) They have a small angular size, they are essentially point-sources at distances beyond the local group of galaxies. This makes it difficult to discern details in their 3D emission structure and kinematics. iii) They are short-lived, their optical luminosity fades away in a few months.

On the other hand, supernova remnants (SNRs) have a larger angular size compared to SNe that produced them, they radiate for long periods of time (several 10^3 yr), and they can provide valuable information about the chemical makeup of the progenitor star and its explosion. There are about 300 known SNRs in our Galaxy (Green 2014). They generally have an angular size of a few to $\sim 50'$ (diameters of a

few to 100 parsecs or pc, where 1 pc $\sim$ 3.26 ly). This allows for the study of structural details with the resolution offered by modern-day telescopes. All of these SNRs have been detected in radio, and over 30% of them can be studied at multiple wavelengths: infrared, optical, X-rays and γ-rays. Emission at these different wavelengths reveals different properties of the SNR including morphology, chemical composition, kinematics and thermodynamic properties of the gas. Among the known SNRs, young SNRs (age $\lesssim$ several 10^3 yr) are especially useful, since they have not undergone extensive mixing with the interstellar medium (ISM). The stellar debris (ejecta) in these young SNRs can be studied to obtain valuable clues about the progenitor star and its explosion (e.g., Branch & Wheeler 2017, pp. 115-134).

Some open questions regarding SNe that can be effectively studied using SNRs are: i) the explosion mechanism ii) nucleosynthesis yields iii) properties of the progenitor star and its evolution iv) properties of the CSM and the ISM v) properties of the compact remnant, the physics of extreme states (NS, black hole etc.), the link between different types of collapsed compact objects and their progenitors vi) shock physics vii) cosmic rays viii) signatures of asymmetry in the explosion and the environment and ix) energy and matter redistribution in the host galaxy and beyond (e.g., Vink et al. 2012; Branch & Wheeler 2017; Patnaude & Badenes 2017, pp. 2233-2249).

1.7 Evolution of Supernova Remnants

Supernova remnants are dynamic, constantly evolving objects. This change is driven by the kinetic energy of the explosion. As supernova remnants expand and interact with their environments, they typically go through four evolutionary phases (Woltjer 1970; Chevalier 1977). The phase that immediately follows the explosion is the *ejecta-dominated* or "*free-expansion phase*." During this phase, the mass of the stellar ejecta is much larger than the swept-up mass of the surrounding interstellar

medium (ISM) and the ejecta expand outward virtually unimpeded at constant velocity. This phase may last $\sim 10^{2-3}$ yr, and the SNR can expand to tens of parsecs in size, depending on the details of the explosion and the density of the ISM (Woltjer 1972; Branch & Wheeler 2017, p. 118).

The second phase in an SNR's evolution is the *Sedov-Taylor* phase. During this phase, the mass of the swept-up ISM is comparable to the mass of the ejecta. The expansion of the shock wave (forward shock or FS) leads to adiabatic cooling of the ejecta, and the pressure in the ejecta behind the FS is less that the pressure of swept-up ISM. This pressure difference generates a reverse shock (RS) wave that moves inwards towards the center of the remnant and heats the ejecta. The boundary separating the FS-heated ISM and the RS-heated ejecta is known as the contact discontinuity (CD) (Fig. 1.2). As the RS forms, the ejecta begin to decelerate. Rayleigh-Taylor (RT) instabilities may form, leading to fragmentation of the ejecta. Temperatures of the shock-heated ejecta and ISM are $>10^6$ K (corresponding to electron temperatures of kT $\sim$ 0.5-2 keV, Borkowski et al. 2001), and they radiate strongly in X-rays. Due to the high temperature, energy conservation applies since energy-loss through radiative processes are small. Emission observed from the SNR in this phase can be the superposition of emission produced by the FS-heated ISM, and the RS-heated ejecta. The dynamic evolution of the SNR in this phase can be described by the self-similar *Sedov-Taylor* solutions, giving this phase its name. These are one-dimensional solutions for the simple approximation of a point-like explosion expanding adiabatically and with spherical symmetry, in an ambient medium of uniform density and minimal pressure (Sedov 1959). These one-dimensional solutions are summarized in Equations 1.1, 1.2 and 1.3:

$$E_0 = \xi^{-1} r^5 t^{-2} \rho \tag{1.1}$$

$$v_{shock} = \frac{dr}{dt} = \frac{2}{5} E_0^{\frac{1}{5}} \rho^{-\frac{1}{5}} t^{-\frac{3}{5}} = \frac{2}{5} \frac{r}{t} \tag{1.2}$$

$$r = \xi^{\frac{1}{5}} E_0^{\frac{1}{5}} \rho^{-\frac{1}{5}} t^{\frac{2}{5}} \tag{1.3}$$

where r is the radius of the FS, t is the time since the explosion, ρ is the mass density of the ambient medium, E_0 is the kinetic energy of the explosion, v_{shock} is the FS-velocity and ξ is a dimensionless constant depending on the adiabatic index (e.g., Vink 2012). The Sedov-Taylor phase may last $\sim 10^{3-4}$ yr (Woltjer 1972), and most observed SNRs are in this phase (Bandiera & Petruk 2010). During this time the SNR evolves self-similarly, maintaining a constant ratio between the radii of the FS, RS and CD. If the RS encounters a pulsar wind nebula (PWN) in the central regions on the SNR (see Section 1.8), then there will a series of interactions between the outer boundary of the PWN and the RS. This can result in a complex, asymmetric structure involving the RS and PWN (e.g., Gaensler & Slane 2006).

The third phase in the evolution of an SNR, is the *pressure-driven*, *radiative*, *isothermal* or "*snow-plough*" phase. The shock velocity has slowed down to $v_{shock} \lesssim$ 200 km s^{-1}. During this phase rapid and efficient cooling through radiative losses takes place. Temperatures drop below 10^6 K, radiation in X-rays declines, while UV and optical emission increases. The cooling causes the shell of expanding swept-up ISM to become thin and dense. The cool shell now carries most of the mass and kinetic energy of the SNR, while the low-density interior gas carries most of the thermal energy. The evolution of the SNR during this phase is described by conservation of momentum. This phase can last for $\sim 10^{5-6}$ yr.

The fourth and final phase of the SNR's evolution is the *merging phase*. During this phase the velocity and temperature of the SNR become comparable to those

of the surrounding ISM. The SNR loses its identity and merges with the ISM. This phase may occur $\gtrsim 10^6$ yr after the explosion.

1.8 Core-Collapse Supernova Remnants

A CCSNR is what is left behind by a CCSN explosion. CCSNe are the most common type of supernova explosion, accounting for ∼75% of all SNe. They are found in galactic regions with high densities of young stars, such as the spiral arms of galaxies, consistent with them being the explosions of young ($\lesssim 10^8$ yr), massive stars ($\gtrsim 8$ $M_\odot$) (e.g., Branch & Wheeler 2017, pp. 16-18). A typical CCSNR consists of circumstellar material (CSM) that was shed by the star through stellar winds before it exploded, and stellar debris from the explosion called ejecta (Fig. 1.2). For a young SNR (age $\lesssim$ several 10^3 yr), the shock-heated CSM and ejecta are at high temperatures (several 10^6 K), which makes them radiate in X-rays. In the central regions of the SNR can be found the collapsed stellar remnant, which may be a NS or black hole. There are a variety of NSs, among which pulsars are rotating NSs with strong magnetic fields. When particles such as electrons are accelerated along these magnetic fields at high speeds, they emit bipolar beams of synchrotron radiation (Hoyle et al. 1964; Pacini 1967). As the pulsar rotates, these beams can be detected as pulses when they align along the line of sight (e.g., Hewish et al. 1968). The pulsar may be surrounded by a PWN, a "bubble" of relativistic, magnetized plasma that produces synchrotron radiation and is confined by the surrounding SNR ejecta (e.g, Amato 2003; Gaensler & Slane 2006; Kirk 2009; Slane 2017, pp. 2159-2179). A pulsar may also be associated with a torus and jet, structures produced by the strong magnetic fields of the rotating NS (e.g, Gaensler & Slane 2006).

CCSNRs can be produced from a wide range of progenitor masses ($\gtrsim 8$ $M_\odot$, see Section 1.2). As a result, they can have a wide range of properties, such as differences

in morphology, chemical composition and the masses of the ejecta and CSM. The morphology and mass of the CSM can be largely influenced by mass loss during the progenitor star's late evolutionary phases such as the red supergiant (RSG) and Wolf-Rayet (WR) phases. Other factors that can affect the properties of an SNR are rotation rate of the progenitor, its metallicity, and binary interactions (e.g., Patnaude & Badenes 2017, pp. 2241-2244). Observation-based studies of CCSNRs, such as measurements of nucleosynthesis yields, pre-SN mass loss estimates, and analysis of asymmetry and morphology of the ejecta, can provide valuable insight into the nature of the progenitor and its explosion.

1.9 Galactic Core-Collapse Supernova Remnant G292.0+1.8

In this thesis, we perform a detailed observation-based study of the Galactic *textbook-type* CCSNR G292.0+1.8 also called MSH 11–54 (G292 hereafter) (Fig. 1.3). G292 is the only SNR in our Galaxy that has all the textbook features of a CCSNR. These features include shock-heated CSM (Gonzalez & Safi-Harb 2003; Park et al. 2002, 2004), metal-rich ejecta (Gonzalez & Safi-Harb 2003; Park et al. 2002, 2007; Yang et al. 2014), a rotation powered pulsar (Camilo et al. 2002; Hughes et al. 2003), whose strong magnetic fields produce a synchrotron-emitting PWN (Hughes et al. 2001; Gaensler & Wallace 2003). These textbook features, make G292 valuable for studying how massive stars evolve, explode, and modify their environments. G292 is relatively young with an age of $\sim$3000 yr. This age was estimated based on the SNR's observed rate of expansion in the optical band (Ghavamian et al. 2005; Winkler et al. 2009), from the analysis of its X-ray emission spectrum (Gonzalez & Safi-Harb 2003) and from the spin-down rate of its pulsar (Camilo et al. 2002). G292 has been studied through observations in the radio, infrared, optical and X-ray wavelengths. It was first discovered in a radio survey of the southern sky (Mills et al. 1961; Milne

1969; Shaver & Goss 1970). It is one of only three known Galactic oxygen-rich CCSNRs (Goss et al 1979). Oxygen-rich CCSNRs are believed to be the remnants of the most massive stars ($M_{ZAMS} \gtrsim 18 M_{\odot}$), and they are characterized by high oxygen abundances and yields relative to other elements (e.g., Vink 2012).

The shocked-CSM in G292 forms distinctive morphological features. These are the dense equatorial belt or ring (a ring-like feature that runs east-west across the "equator" of the remnant), thin circumferential filaments (narrow arcs of soft emission near the outer boundary) and the diffuse, spectrally soft emission at the outer edge of the SNR marking where the FS is interacting with the RSG winds of the progenitor (Gonzalez & Safi-Harb 2003; Ghavamian et al. 2005, 2012, 2016; Lee et al. 2009; Lee et al. 2010; Park et al. 2002, 2004, 2007). The origin of these morphological features is not clear. Structures such as the dense equatorial ring may have originated from a rotating RSG progenitor and/or from binary interactions (e.g., Chevalier 1992; Morris & Podsiadlowski 2009; Smith et al. 2013).

The ejecta in G292 form a complex network of O-, Ne- and Mg-rich knots and filaments across the face of the SNR (Figure 1.3). Elemental abundance ratios of O, Ne, Mg, Si, S and Fe from several bright ejecta knots (Gonzalez & Safi-Harb 2003; Park et al. 2004) or from spectra of the entire remnant (Hughes & Singh 1994; Kamitsukasa et al. 2014; Yang et al. 2014) have suggested a progenitor mass of 25 $M_{\odot} \lesssim$ M $\lesssim$ 40 $M_{\odot}$.

G292 has a "normal" rotation powered pulsar (PSR J1124-5916, Camilo et al. 2002; Hughes et al. 2003). The pulsar is displaced $\sim$46″ from the expansion center of the SNR to the southeast (Hughes et al. 2003; Winkler et al. 2009). This displacement suggests that the NS in G292 was kicked during the explosion (Park et al. 2007) giving it a transverse velocity of $\sim$440 km s^{-1} (Hughes et al. 2001, 2003; Winkler et al. 2009).

Several previous studies have uncovered evidence for ejecta asymmetry in G292. A temperature gradient has been observed between the northwest and southeast (Park et al. 2007). Larger proper motions of optical ejecta knots have been measured in the north-south direction than in the east-west direction (Winkler et al 2009). An asymmetric distribution of radial velocities for ejecta knots has been observed in the optical band (Ghavamian et al 2005). The detailed spatial distribution of the ejecta in G292 has not been known, and details of radial stratification and/or azimuthal asymmetry in the ejecta have also been unknown.

1.10 The *Chandra* X-ray Observatory

Young SNRs like G292 radiate strongly in X-ray and can therefore be effectively studied at this wavelength. In this work, we utilize data collected by NASA's *Chandra* X-ray Observatory (*Chandra* hereafter). *Chandra* is one of NASA's four Great Observatories (Weisskopf et al. 2002). It was launched and deployed by space shuttle Columbia in July 1999. Here we briefly describe the main instruments on *Chandra*.

1.10.1 The X-ray Telescope

The main components of the telescope are the High Resolution Mirror Assembly (HRMA), the Optical Bench Assembly (OBA), and the transmission gratings. The HRMA consists of 4 pairs of cylindrically-shaped mirrors that nudge the incoming X-rays at very shallow angles so that they converge on the focal plane. The OBA is a long, narrow tube-like structure that shields the incoming X-rays as they travel to the focal plane (Fig. 1.4).

1.10.2 The Science Instruments

Chandra has four instruments, two diffraction gratings, that diffract or redirect incoming X-ray photons based on their energies (or wavelengths), and two detectors placed at the focal plane that capture the X-rays and produce electronic signals.
The *Advanced CCD Imaging Spectrometer (ACIS)* consists of two arrays of charge coupled devices (CCDs), the ACIS-I array, and the ACIS-S array. Each CCD is 2.5-cm square in size and has 1024×1024 pixels. The function of the CCDs is to record the number, position, energy and arrival-time of the detected X-ray photons.

The ACIS-I array is a 2×2 CCD array, used for high-resolution ($\sim 0.5''$) imaging and spectroscopic studies. It has a $17' \times 17'$ field of view. All four of the CCDs are front-illuminated. Front-illuminated CCDs have their gate structures facing the incoming X-ray photons. This gives them slightly higher quantum efficiency in photon energies of $E \gtrsim 3$ keV compared to the back-illuminated CCDs (ones that have their their gate structures facing away from the incoming X-ray photons).
The ACIS-S is a 6×1 array of CCDs providing a $8.3' \times 50.6'$ field of view. This array serves as an optimized read-out detector for the High Energy Transmission Grating. Four of its CCDs are front-illuminated, and two of them (S1 and S3) are back-illuminated. The back-illuminated CCDs have a slightly higher quantum efficiency for lower photon energies ($E \lesssim 3$ keV) compared to the front-illuminated ones. The central back-illuminated S3 CCD can be placed at the best focus of the telescope, and can be used for high-resolution ($\sim 0.5''$) imaging and spectroscopic studies, but with a smaller ($8.3' \times 8.3'$) field of view (Fig. 1.5).

The *High Resolution Camera (HRC)* contains two microchannel plate (MCP) imaging detectors. The MCPs contain millions of 10 μm-wide lead oxide glass tubes that convert incoming X-ray photons to electronic signals. The HRC consists of two detectors: HRC-I has a large field of view ($30' \times 30'$) and is used for imaging. HRC-S

has a $6' \times 99'$ field of view and is used for spectroscopy. The HRC-S serves as the read-out detector for the Low Energy Transmission Grating (LETG).

There are two diffraction grating spectrometers. They can be inserted in the optical path (after the mirrors) to disperse the incoming X-rays and produce high-resolution spectra. The amount of diffraction depends on the wavelength of the X-ray photons and is given by the equation:

$$sin\beta = m\lambda/p \tag{1.4}$$

where β is the angle of diffraction, m is the order number, λ is the photon wavelength and p is the period of the gratings (Canizares et al. 2005).

The *High Energy Transmission Grating (HETG)* consists of an array of 336 diffraction grating facets. Each facet is ∼2.5-cm square and consists of microscopic gold bars (∼100s nm) aligned at intervals of a few hundred nm. The advantage of this design is its ability to diffract the incoming X-rays at high efficiency. The HETG consists of two types of grating facets: a) Medium Energy Gratings (MEG) consist of 192 facets with the gold bars arranged at 400 nm intervals, they provide high-resolution spectroscopy (0.023 Å FWHM) in the 0.4 to 4 keV range (3 nm to 0.3 nm). b) High Energy Gratings (HEG) consist of 144 facets with the gold bars arranged at 200 nm intervals to provide high-resolution spectroscopy (0.012 Å FWHM) in the 0.8 keV to 8 keV range (1.5 nm to 0.15 nm) (Weisskopf et al. 2000, 2005). The MEG and HEG are aligned with a 10° offset between their dispersion axes so that their spectra are distinct, and form an "X-shaped" pattern on the ACIS-S detector.

The *Low Energy Transmission Grating (LETG)* consists of 540 1.6-cm-wide gold facets arranged on a ring structure. The gold bars in the facets are arranged with a period of 991 nm. The LETG provides high-resolution spectroscopy (0.05 Å FWHM) in the 0.08 keV to 2 keV range (15 nm to 0.6 nm) (Weisskopf et al. 2000, 2005).

1.11 Data Processing and Analysis Methods

1.11.1 Data and software

We acquired *Chandra* X-ray data for G292 in two separate observations, a 114 ks (∼32 hr) HETG & ACIS-S observation in 2011, and a 509 ks (∼6 days) ACIS-I observation in 2006. We performed data processing and analysis using the Chandra Interactive Analysis of Observations (CIAO)[1] software, a standard software package provided by NASA's Chandra X-ray Center (Galle et al. 2005; Fruscione et al. 2006). For the spectral analysis of G292 we use two packages: XSPEC, a spectral fitting package, part of the HEAsoft suite[2] provided by NASA's High Energy Astrophysics Science Archive Research Center at the Goddard Space Flight Ceter (HEASARC, Arnaud, 1996), and the Interactive Spectral Interpretation System (ISIS) software package[3] provided by MIT through the Chandra X-ray Center (Houck & Denicola, 2000). ISIS has built-in access to all XSPEC spectral analysis models and databases, and was developed for the analysis of high-resolution *Chandra* gratings data, which we use in the first part of this study. ISIS also offers parallel-processing capability which is very useful for the high-volume spectral analysis we perform in the second part of this thesis. In the second part of this thesis, we use adaptive mesh software developed by our SNR group at UTA for the automated spectral analysis of *Chandra* SNR data (Schenck et al. 2016).

1.11.2 Spectral Analysis

In the first part of this work, we estimate radial velocities of ejecta features in G292 by measuring Doppler shifts in the emission lines of Ne, Mg and Si ions.

[1] http://cxc.harvard.edu/ciao/

[2] http://heasarc.nasa.gov/lheasoft/

[3] http://space.mit.edu/asc/isis/

We measure these line shifts using Gaussian model fits to the spectra extracted from small ($\sim$2″–9″) emission features in G292. From our measured Doppler shifts, we calculate the radial velocity (v_r) of these features:

$$v_r = \frac{c(\lambda_{obs} - \lambda_{rest})}{\lambda_{rest}} \tag{1.5}$$

where c is the speed of light ($\sim 3\times10^5$ km s^{-1}), λ_{obs} is the measured wavelength of the emission line, and λ_{rest} is its rest wavelength . The software tools we use for these v_r measurements are CIAO (TGCat[4]) and ISIS. Throughout this work we study the physical and chemical properties of the SNR, by performing spectral model fits to the observed emission spectra. We perform these spectral model fits using the absorbed non-equilibrium ionization (NEI) plane-parallel shock model (Borkowski et al. 2001) with varied abundances (VPSHOCK, NEI versions 2.0 & 3.0 with augmented ATOMDB in XSPEC and ISIS, Houck & Denicola 2000; Smith et al. 2001; Badenes et al. 2006; Foster et al. 2012). These spectral models characterize the emission from shock-heated, optically-thin plasmas. The model parameters include the electron temperature (kT, where k is the Boltzmann constant), ionization timescale ($n_e t$, which is a product of the electron density, n_e, and the time, t, since the plasma was shocked), and the normalization ($norm$) which is the scaled volume emission measure (EM),

$$norm = \frac{10^{-14} EM}{4\pi D^2} \tag{1.6}$$

where D is the distance to the source in cm,

$$EM = \int n_e n_H dV \tag{1.7}$$

where n_H is the post-shock hydrogen number density, and V is the volume of the X-ray emitting gas. The model also includes parameters for the abundances of common elements: O, Ne, Mg, Si, S, Ar, Ca and Fe.

[4]http://tgcat.mit.edu/

1.12 Thesis Composition

This thesis describes our detailed study of the Galactic core-collapse supernova remnant G292. It has two main parts. In Chapter 2, we study the kinematics of the X-ray-emitting ejecta in G292 based on our ∼120 ks *Chandra* HETGS data. We infer the shock-structure of the remnant, we discuss our detection of ejecta v_r-asymmetry, and based on the SNR's observed dynamics, we place constraints on the the G292 progenitor mass and the total ejecta mass. This part of the thesis has been published in *The Astrophysical Journal* (Bhalerao et al. 2015). In Chapter 3, we reveal the detailed structure of the ejecta and CSM in G292 based on our ∼530 ks archival *Chandra* ACIS-I data. We construct high-resolution spatial distribution maps covering the entire remnant for the elemental abundances and the plasma physical parameters. We detect significant asymmetry in the ejecta distribution, and for the first time we detect the spatial distribution of Fe at high resolution. We estimate the masses of the ejecta and the CSM. Based on our measured abundance ratios and the ejecta masses, we place constraints on the G292 progenitor mass. We will submit this part of the thesis to *The Astrophysical Journal* (Bhalerao et al. 2018, in preparation). Finally, in Chapter 4, we present a summary and conclusion.

REFERENCES

[Alsabti & Murdin (2017)] Alsabti, A. W. & Murdin, P. 2017, in Handbook of Supernovae, ed. A. W. Alsabti & P. Murdin (Cham, Switzerland, Springer International Publishing AG)

[Amato (2003)] Amato, E. 2003, ChJAS, 3, 316

[Arcavi (2017)] Arcavi, I. 2017, in Handbook of Supernovae, ed. A. W. Alsabti & P. Murdin (Cham, Switzerland, Springer International Publishing AG)

[Arnaud (1996)] Arnaud, K. A. 1996, ASPC, 101, 17

[Baade & Zwicky (1934a)] Baade, W. & Zwicky, F. 1934a, PNAS, 20, 254

[Baade & Zwicky (1934b)] Baade, W. & Zwicky, F. 1934b, PhRv, 46, 76

[Badenes et al. (2006)] Badenes, C., Borkowski, K. J., Hughes, J. P., Hwang, U., & Bravo, E. 2006, ApJ, 645, 1373

[Balazs et al. (2004)] Balazs, L. G., Abraham, P., Kun, M. et al. 2004, 425, 133

[Bandiera & Petruk (2010)] Bandiera, R. & Petruk, O. 2010, A&A, 509, 34

[Bethe & Wilson (1985)] Bethe, H. A. & Wilson, J. R. 1985, ApJ, 295, 14

[Bethe (1994)] Bethe, H. A. 1994, RSPTA, 346, 251

[Bhalerao et. al. (2015)] Bhalerao, J., Park, S., Dewey, D. et al. 2015, ApJ, 800, 65

[Borkowski et al. (2001)] Borkowski, K. J., Lyerly, W. J., & Reynolds, S. P. 2001, ApJ, 548, 820

[Boss, A. P. (2017a)] Boss, A. P., 2017, in Handbook of Supernovae, ed. A. W. Alsabti & P. Murdin (Cham, Switzerland, Springer International Publishing AG), 2401

[Boss, A. P. (2017b)] Boss, A. P., ApJ, 2017, 844, 113

[Branch & Wheeler (2017)] Branch, D. & Wheeler, J. C. 2017, Supernova Explosions, Springer-Verlag GmbH, Berlin, Germany

[Burrows, A. (2000)] Burrows, A. 2000, Nature, 403, 727

[Burrows, A. (2013)] Burrows, A. 2013, RvMP, 85, 245

[Burrows et al. (2018)] Burrows, A., Vartanyan, D., Dolence, J. C. et al. 2018, SSRv, 214, 33

[Camilo et al. (2002)] Camilo, F., Manchester, R. N., Gaensler, B. M., Lorimer, D. R., & Sarkissian, J. 2002, ApJ, 567, L71

[Canizares et al. (2005)] Canizares, C. R., Davis, J. E., Dewey, D. et al. 2005, PASP, 117, 1144

[Chatterjee (2005)] Chatterjee, S., Vlemmings, W. H. T., Brisken, W. F., et al. 2005, ApJ, 630, L61

[Chatzopoulos & Wheeler (2012)] Chatzopoulos, E. & Wheeler, J. C. 2012, ApJ, 748, 42

[Chevalier (1977)] Chevalier, R. A. 1977, ARA&A, 15, 175

[Chevalier (1992)] Chevalier, R. A. 1992, Nature, 355, 691

[Conselice et al. (2016)] Conselice, C. J., Wilkinson, A., Duncan, K. & Mortlock, A. 2016, ApJ, 830, 83

[Couch (2017)] Couch, S. M. 2017, RSPTA, 375, 20160271

[Doherty et al. (2017)] Doherty, C. L., Gil-Pons, P., Siess, L. et al. 2017, PASA, 34, 56

[Eldridge (2008)] Eldridge, J. J. 2008, RSPTA, 366, 4441

[Filippenko (1997)] Filippenko, A. V. 1997, ARA&A, 35, 309

[Foglizzo et al. (2015)] Foglizzo, T., Kazeroni, R, Guilet, J. et al. 2015, PASA, 32, 9

[Foglizzo (2017)] Foglizzo, T. 2017, in Handbook of Supernovae, ed. A. W. Alsabti & P. Murdin (Cham, Switzerland, Springer International Publishing AG), 1053

[Foster et al. (2012)] Foster, A. R., Ji, L., Smith, R. K., & Brickhouse, N. S. 2012, ApJ, 756, 128

[Frebel & Norris (2015)] Frebel, A & Norris, J.E. 2015, ARA&A, 53, 631

[Fruscione et al. (2006)] Fruscione, A., McDowell, J. C., Allen, G. E. et al. 2006, SPIE, 6270, 60

[Gaensler & Wallace (2003)] Gaensler, B. M. & Wallace, B. J. 2003, ApJ, 594, 326

[Gaensler & Slane (2006)] Gaensler, B. M. & Slane, P. O. 2006, ARA&A, 44, 17

[Gal-Yam (2012)] Gal-Yam, A. 2012, Science, 337, 927

[Galle et al. (2005)] Galle, E. C., Burke, D. J., Stawarz, C. & Fruscione, A. 2005, ASPC, 347, 473

[Ghavamian et al. (2005)] Ghavamian, P., Hughes, J. P., & Williams, T. B. 2005, ApJ, 635, 365

[Ghavamian et al. (2012)] Ghavamian, P., Long, K. S., Blair, W. P., et al. 2012, ApJ, 750, 39

[Ghavamian & Williams (2016)] Ghavamian, P. & Williams, B. J. 2016, ApJ, 831, 188

[Gonzalez & Safi-Harb (2003)] Gonzalez, M. & Safi-Harb, S. 2003, ApJ, 583, L91

[Goss et al. (1979)] Goss, W. M., Shaver, P. A., Zealey, W. J., et al. 1979, MNRAS, 188, 357

[Green (2014)] Green, D. A. 2014, BASI, 42, 47

[Heger & Woosley (2002)] Heger, A. & Woosley, S. E. 2002, ApJ, 567, 532

[Heger et al. (2003)] Heger, A., Fryer, C. L., Woosley, S. E. et al. 2003, ApJ, 591, 288

[Herbst & Assousa (1977)] Herbst, W. & Assousa, G. E. 1977, ApJ, 217, 473

[Herwig (2005)] Herweg, F. 2005, ARA&A, 43, 435

[Hester & Desch (2005)] Hester, J. J. & Desch, S. J. 2005, ASP Conf. Ser., 341, 107

[Hewish et al. (1968)] Hewish, A., Bell, S. J., Pilkington, J. D. et al. 1968, Nature, 217, 709

[Hillebrandt & Niemeyer (2000)] Hillebrandt, W. & Niemeyer, J. C. 2000, ARA&A, 38, 191

[Holland-Ashford (2017)] Holland-Ashford, T., Lopez, L., Auchettl, K., et al. 2017, ApJ, 844, 84

[Houck & Denicola (2000)] Houck, J. C. & Denicola, L. A. 2000, in ASP Conf. Ser. 216, Astronomical Data Analysis Software and Systems IX, ed. N. Manset, C. Veillet, & D. Crabtree, (San Francisco, CA:ASP), 591

[Hoyle & Fowler (1960)] Hoyle, F. & Fowler, W. A. 1960, ApJ, 132, 565

[Hoyle et al. (1964)] Hoyle, F., Narlikar, J. V. & Wheeler, J. A. 1964, Nature, 203, 914

[Hughes & Singh (1994)] Hughes, J. P. & Singh, K. P. 1994, ApJ, 422, 126

[Hughes et al. (2001)] Hughes, J. P., Slane, P. O., Burrows, D. N., et al. 2001, ApJ, 559, L153

[Hughes et al. (2003)] Hughes, J. P., Slane, P. O., Park, S., Roming, P. W. A., & Burrows, D. N. 2003, ApJ, 591, L139

[Iben & Renzini (1983)] Iben, I. & Renzini, A. 1983, ARA&A, 21, 271

[Iben (1985)] Iben, I. 1985, QJRAS, 26, 1

[Kamitsukasa et al. (2014)] Kamitsukasa, F., Koyama, K., Tsunemi, H., et al. 2014, PASJ, 66, 648

[Karlsson et al. (2013)] Karlsson, T., Bromm, V. & Bland-Hawthorn, J. 2013, 85, 809

[Katsuda et al. (2018)] Katsuda, S., Morii, M., Janka, H.-T., et al. 2018, ApJ, 856, 18

[Kirk et al. (2009)] Kirk, J. G., Lyubarsky, Y & Petri, J. 2009, in Astrophysics and Space Science Library, ed. W. Becker (Cham, Switzerland, Springer International Publishing AG), p.421

[Kozyreva et al. (2018)] Kozyreva, A., Kromer, M., Noebauer, U. M. & Hirschi, R. 2018, MNRAS, 479, 3106

[Lai (2001)] Lai, D. 2001, in Lecture Notes in Physics, ed. D. Blaschke, N. K. Glendenning & A. Sedrakian (Berlin, Springer Verlag), 578, 424

[Langer (2012)] Langer, N. 2012, ARA&A, 50, 107

[Lee et al. (2009)] Lee, H.-G., Koo, B.-C., Moon, D.-S., et al. 2009, ApJ, 706, 441

[Lee et al. (2010)] Lee, J.-J., Park, S., Hughes, J. P., et al. 2010, ApJ, 711, 861

[Mac Low (2005)] Mac Low, M.-M., Balsara, D., Kim, J. & de Avillez, M. A. 2005, ApJ, 626, 864

[Maoz (2007)] Maoz, D. 2007, Astrophysics in a Nutshell (Princeton, NJ, Princeton University Press)

[Mills et al. (1961)] Mills, B. Y., Slee, O. B., & Hill, E. R. 1961, Australian J. Phys., 14, 497

[Milne (1969)] Milne, D. K. 1969, Australian J. Phys., 22, 613

[Minkowski (1941)] Minkowski, R. 1941, PASP, 53, 224

[Miyaji et al. (1980)] Miyaji, S., Nomoto, K., Yokoi, K. & Sujimoto, D. 1980, ApJ, PASJ, 32, 303

[Morris & Podsiadlowski (2009)] Morris, T. & Podsiadlowski, Ph. 2009, MNRAS, 399, 515

[Nittler & Ciesla (2016)] Nittler, L. R. & Ciesla, F. 2016, ARA&A, 54, 53

[Nomoto (1984)] Nomoto, K. 1984, ApJ, 277, 791

[Nomoto et al. (2013)] Nomoto, K., Kobayashi, C. & Tominaga, N. 2013, ARA&A, 51, 457

[Pacini (1967)] Pacini, F. 1967, Nature, 216, 567

[Park et al. (2002)] Park, S., Roming, P. W. A., Hughes, J. P. et al. 2002, ApJ, 564, L39

[Park et al. (2004)] Park, S., Hughes, J. P., Slane, P. O., et al. 2004, ApJ, 602, L33

[Park et al. (2007)] Park, S., Hughes, J. P., Slane, P. O., et al. 2007, ApJ, 670, L121

[Patnaude & Badenes (2017)] Patnaude, D. & Badenes, C. 2017, in Handbook of Supernovae, ed. A. W. Alsabti & P. Murdin (Cham, Switzerland, Springer International Publishing AG)

[Podsiadlowski et al. (1992)] Podsiadlowski, Ph., Joss, P. C. & Hsu, J. J. L. 1992, ApJ, 391, 246

[Ropke (2017)] Ropke, F. K. 2017, in Handbook of Supernovae, ed. A. W. Alsabti & P. Murdin (Cham, Switzerland, Springer International Publishing AG)

[Scheck et al. (2006)] Scheck, L., Kifondis, K., Janka, H.Th. & Muller, E. 2006, A&A, 457, 963

[Schenck et al. (2016)] Schenck, A., Park, S., & Post, S. 2016, AJ, 151, 161

[Schlegel (1990)] Schlegel, E. M. 1990, MNRAS, 244, 269

[Sedov (1959)] Sedov, L. I. 1959, Similarity and Dimensional Methods in Mechanics (New York: Academic)

[Shaver & Goss (1970)] Shaver, P. A., & Goss, W. M. 1970. Australian J. Phys., Astr. Suppl., 14, 133

[Slane (2017)] Slane, P. 2017, in Handbook of Supernovae, ed. A. W. Alsabti & P. Murdin (Cham, Switzerland, Springer International Publishing AG)

[Smith et al. (2001))] Smith, R. K., Brickhouse, N. S., Liedahl, D. A. & Raymond, J. C. 2001, ApJ, 556, L91

[Smith et al. (2013)] Smith, N., Arnett, W. D., Bally, J. et al. 2013, MNRAS, 429, 1324

[Stevenson (2014)] Stevenson, D. 2014, in Extreme Stellar Explosions, Cham, Switzerland, Springer International Publishing AG

[Taubenberger et al. (2011)] Taubenberger, S., Navasardyan, H., Maurer, J. I. et al. 2011, MNRAS, 413, 2140

[Thielemann (2018)] Thielemann, F.-K., Isern, J., Perego, A & von Ballmoos, P. 2018, SSRv, 214, 62

[Vink (2012)] Vink, J. 2012, A&ARv, 20, 49

[Weisskopf et al. (2000)] Weisskopf, M. C., Tananbaum, H., Van Speybroeck, L., & O'Dell, S. 2000, Proc. SPIE, 4012, 1

[Weisskopf et al. (2002)] Weisskopf, M. C., Brinkman, B., Canizares, C., et al. 2002, PASP, 114, 1

[Weisskopf et al. (2005)] Weisskopf, M. C., Aldcroft, T. L., Bautz, M. et al. 2005, CIBu, 162, 5

[Winkler et al. (2009)] Winkler, P. F., Twelker, K., Reith, C. N., & Long, K. S. 2009, ApJ, 692, 1489

[Woltjer (1970)] Woltjer, L. 1970, I.A.U. Symposium, 39, 229, D. Reidel Publishing Co., Dordrecht, Holland

[Woltjer (1972)] Woltjer, L. 1972, ARA&A, 10, 129

[Wongwathanarat et al. (2013)] Wongwathanarat, A., Janka, H.-Th. & Muller, E. 2013, A&A, 552, 126

[Wongwathanarat et al. (2017)] Wongwathanarat, A., Janka, H.-T., Mller, E., Pllumbi, E. & Wanajo, S. 2017, ApJ, 842, 13

[Woosley & Weaver (1986)] Woosley, S. & Weaver, T. A. 1986, ARA&A, 24, 205

[Woosley et al. (2002)] Woosley, S. E., Heger, A. & Weaver, T. A. 2002, Rev. Mod. Phys., 74, 1015

[Woosley & Janka (2005)] Woosley, S. & Janka, T. 2005, NatPh, 1, 147

[Woosley & Heger (2015)] Woosley, S. & Heger, A. 2015, ApJ, 810, 34

[Yang et al. (2014)] Yang, X.-J., Liu, X.-Q., Li, S.-Y., & Lu, F.-J. 2014, RAA, 14, 1279

[Zampieri (2017)] Zampieri, L. 2017, in Handbook of Supernovae, ed. A. W. Alsabti & P. Murdin (Cham, Switzerland, Springer International Publishing AG)

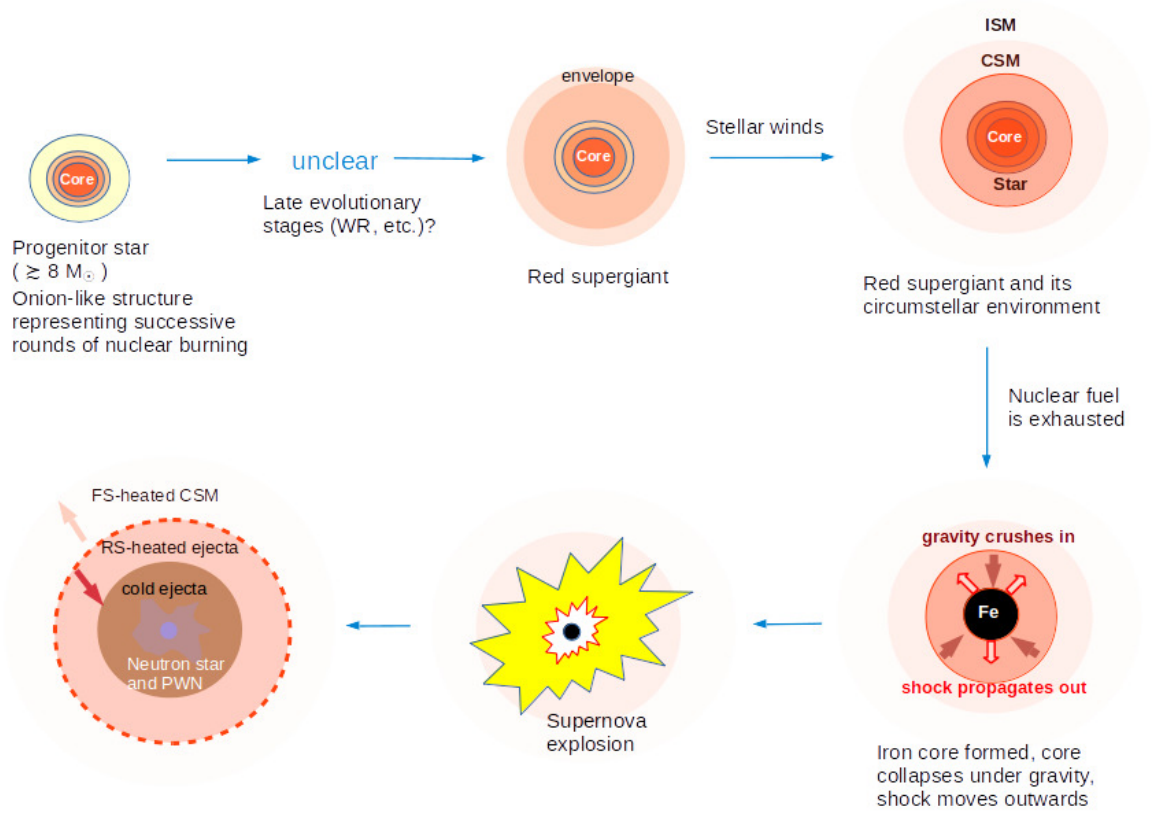

Figure 1.1 Schematic illustration of the end stages in the life of a massive star (Eldridge 2008; Vink 2012; Stevenson 2014; Foglizzo 2017, pp. 1053-1073).

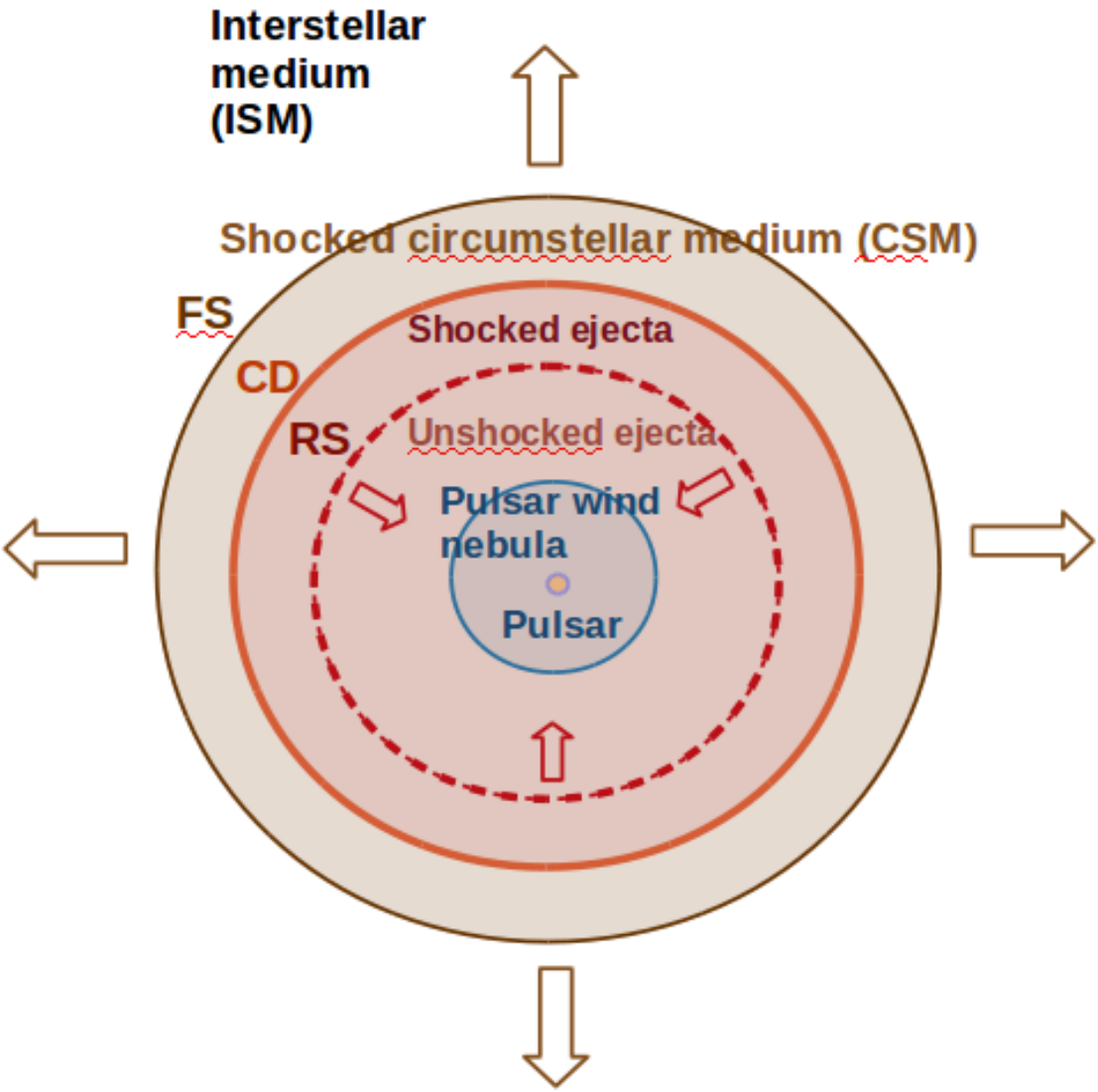

Figure 1.2 Schematic view of the basic structure of a CCSNR. The pulsar is the compact remnant left behind by the explosion. Its rapid rotation and strong magnetic fields power the surrounding pulsar wind nebula. The forward shock (FS) is the outermost blast wave that sweeps up, and heats the surrounding circumstellar medium/interstellar medium (CSM/ISM). The reverse shock (RS) is an inwardly-propagating shock wave that heats up the metal-rich stellar debris (ejecta). The contact discontinuity (CD) is the boundary between the FS and the RS.

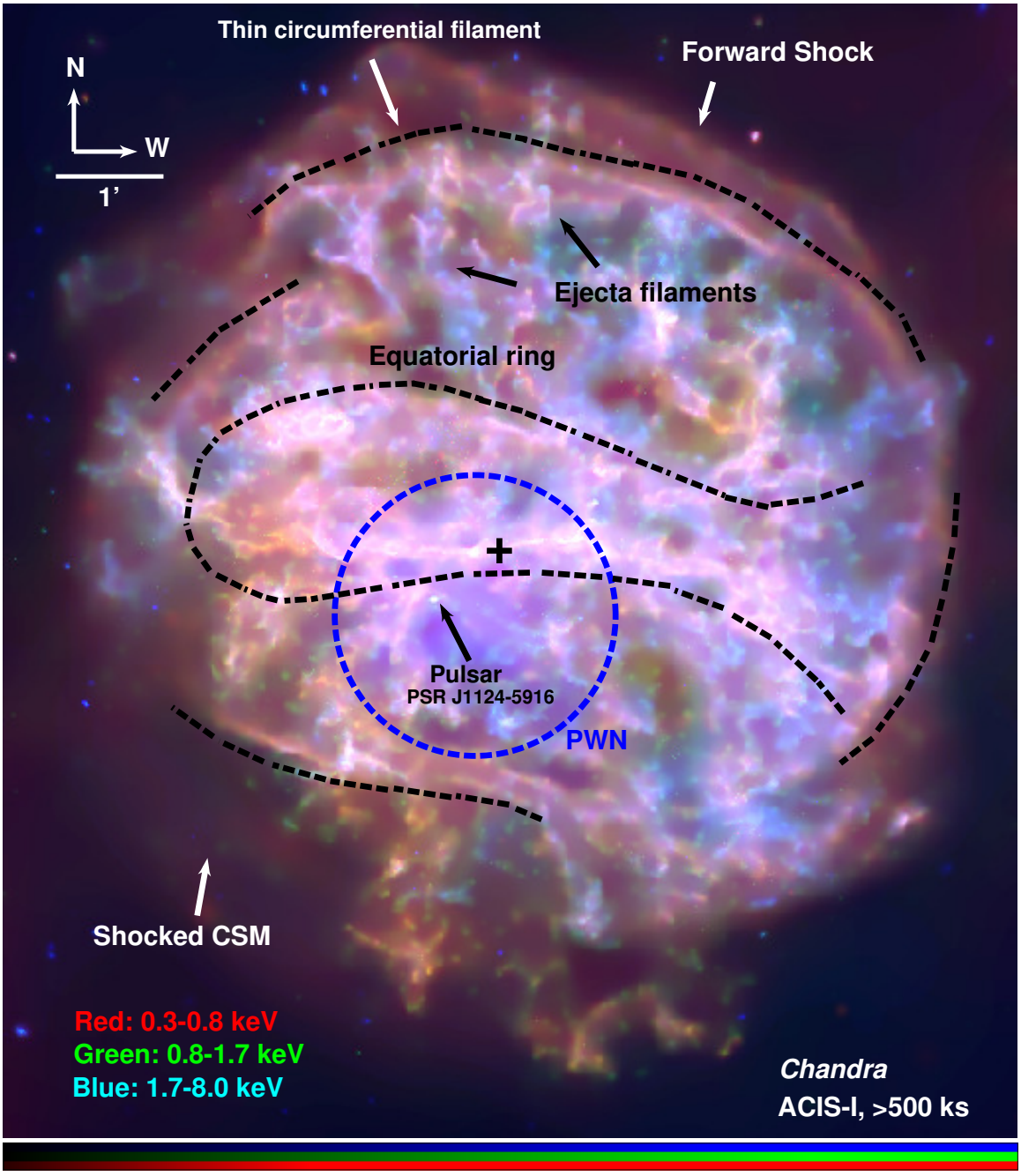

Figure 1.3 *Chandra* ACIS-I three-color image of G292. The colors Red, Green and Blue represent X-ray emission at different energies as labeled on the figure. Prominent structural and morphological features are indicated. The cross marks the optical expansion center of the remnant (Winkler et al. 2009).

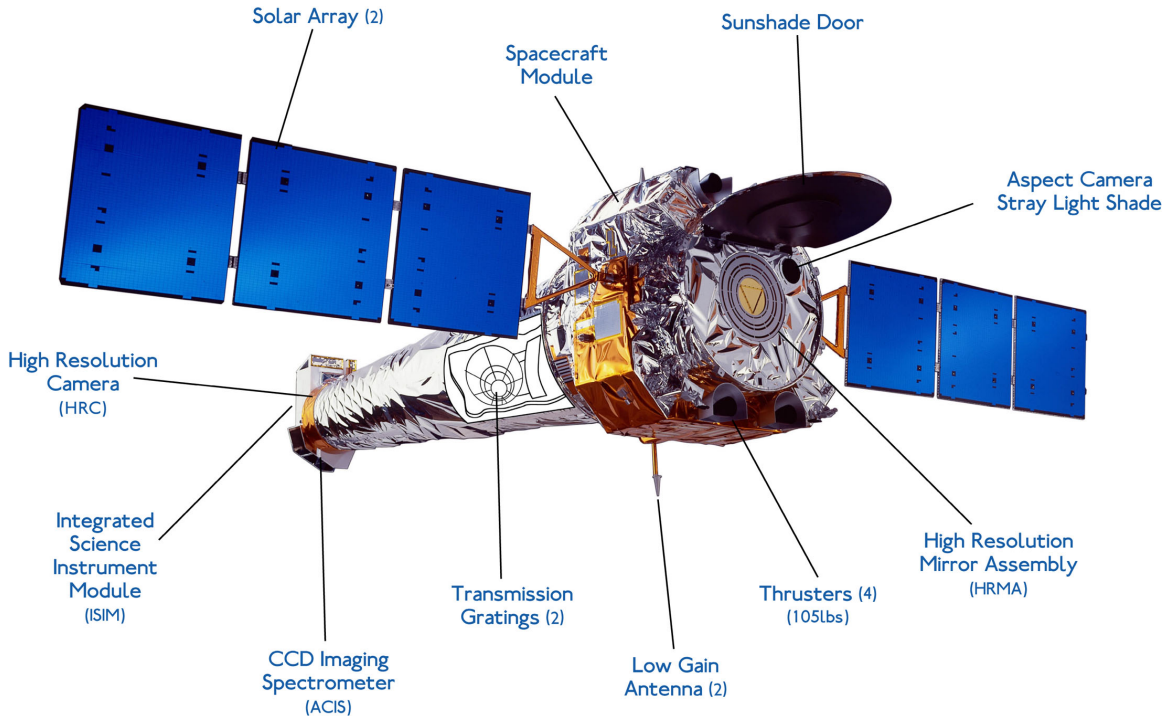

Figure 1.4 Artist's concept of the *Chandra* X-ray Observatory. The spacecraft measures about 13.8 x 19.5 meters with the solar panels deployed, weighs ∼4790 kg, and orbits the Earth at a distance that varies between ∼16,000 to ∼133,000 km (https://www.nasa.gov/centers/marshall/pdf/108075main_chandra_fact_sheet.pdf). Image credit:
`https://www.nasa.gov/sites/default/files/images/704250main_chandra-telescope_full.jpg`.

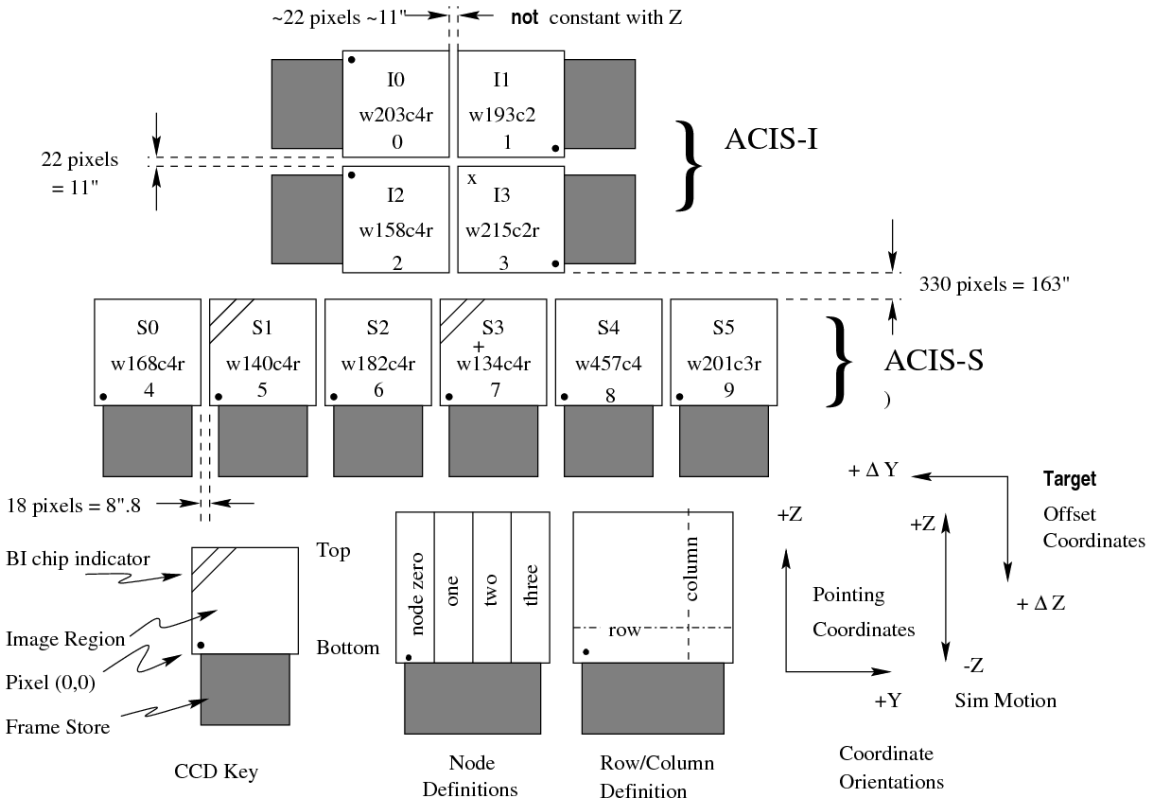

Figure 1.5 Schematic representation of the ACIS CCD arrays viewed along the optical axis. The default aimpoint on the ACIS-I3 CCD is marked by an 'X,' and the default aimpoint on the ACIS-S3 CCD is marked by a '+.' The ACIS-S3 and ACIS-S1 CCDs are back-illuminated, while all the others are front-illuminated. Image credit: CXC/The *Chandra* Proposers' Observatory Guide (http://cxc.harvard.edu/proposer/POG/html/chap6.html)

CHAPTER 2

X-Ray Ejecta Kinematics of the Galactic Core-Collapse Supernova Remnant G292.0+1.8

Jayant Bhalerao[1], Sangwook Park[1], Daniel Dewey[2], John P. Hughes,[3]
Koji Mori[4], and Jae-Joon Lee[5]

[1] Box 19059, Department of Physics, University of Texas at Arlington, Arlington, TX 76019

[2] MIT Kavli Institute, Cambridge, MA 02139

[3] Department of Physics and Astronomy, Rutgers University, 136 Frelinghuysen Road, Piscataway, NJ 08854-8019

[4] Department of Applied Physics, University of Miyazaki, 1-1 Gakuen Kibana-dai Nishi, Miyazaki, 889-2192, Japan

[5] Korea Astronomy and Space Science Institute, Daejeon, 305-348, Korea

---

(Bhalerao et al. 2015, ApJ, 800, 65)

2.1 ABSTRACT

We report on the results from the analysis of our 114 ks *Chandra* HETGS observation of the Galactic core-collapse supernova remnant G292.0+1.8. To probe the 3D structure of the clumpy X-ray emitting ejecta material in this remnant, we measured Doppler shifts in emission lines from metal-rich ejecta knots projected at different radial distances from the expansion center. We estimate radial velocities of ejecta knots in the range of -2300 $\lesssim v_r \lesssim$ 1400 km s^{-1}. The distribution of ejecta knots in velocity vs. projected-radius space suggests an expanding ejecta shell with a projected angular thickness of $\sim$90$''$ (corresponding to $\sim$3 pc at d = 6 kpc). Based on this geometrical distribution of the ejecta knots, we estimate the location of the reverse shock approximately at the distance of $\sim$4 pc from the center of the supernova remnant, putting it in close proximity to the outer boundary of the radio pulsar wind nebula. Based on our observed remnant dynamics and the standard explosion energy of 10^{51} erg, we estimate the total ejecta mass to be $\lesssim$ 8 M$_\odot$, and we propose an upper limit of $\lesssim$ 35 M$_\odot$ on the progenitor's mass.

Key words: ISM: individual objects (G292.0+1.8)– ISM: kinematics and dynamics – ISM: supernova remnants – X-rays: individual (G292.0+1.8)

2.2 INTRODUCTION

G292.0+1.8 is a Galactic oxygen-rich (O-rich) core-collapse supernova remnant (CC SNR) that has been studied at different wavelengths over the past five decades. Previous studies have captured a complex portrait composed of typical elements for a CC SNR – a pulsar (Camilo et al. 2002; Hughes et al. 2003), and its wind-blown nebula or pulsar wind nebula (PWN, Hughes et al. 2001; Gaensler & Wallace 2003 (GW03 hereafter); Park et al. 2007), the blast wave-shocked circumstellar medium

(CSM, Park et al. 2002; Lee et al. 2009; Lee et al. 2010 (L10 hereafter)), and metal-rich ejecta knots strewn across the interior in intricate filamentary networks (Gonzalez & Safi-Harb 2003; Park et al. 2004; 2007; Ghavamian et al. 2005; 2009; 2012; Winkler & Long 2006; Winkler et al. 2009). Yet details about the progenitor star and how its explosion led to the complex patterns of shocked ejecta and CSM seen in the sky today, remain elusive. The mass of the progenitor star has not been tightly constrained ($\sim$20-40 $M_{\odot}$, Hughes & Singh 1994; Gonzales & Safi-Harb 2003; Park et al. 2004; L10; Kamitsukasa et al. 2014; Yang et al. 2014). It is unclear if the progenitor has gone through phases other than the red supergiant (RSG). The presence of the equatorial belt (a bright, belt-like emission feature of shocked dense CSM enhanced along the "equator" of the SNR, Park et al. 2002; Ghavamian et al. 2005; Lee et al. 2009) suggests that the progenitor was probably rapidly rotating and/or in a binary system, but extensive studies on the progenitor system have not been performed. The associated pulsar (PSR J1124-5916) is apparently off the geometric center of the SNR (e.g., Hughes et al. 2001) indicating a significant pulsar-kick which could be related to a non-symmetric SN explosion (Park et al. 2007). The details of the pulsar-kick and its relationships with the progenitor system and explosion mechanism in G292.0+1.8 are not known. In contrast to Cassiopeia A (Cas A, a $\sim$10 times younger cousin of G292.0+1.8), in which abundant Fe-group ejecta material is observed (e.g., Hwang & Laming 2012, HL12 hereafter), such explosive nucleosynthesis products had not been detected in G292.0+1.8. Recently, a *Suzaku* study detected faint Fe K-shell line emission in G292.0+1.8, probably originating from hot Fe-rich ejecta (Kamitsukasa et al. 2014).

A supernova (SN) explosion releases elements synthesized by the life-long efforts of a star (somewhat modified during its explosion) as metal-rich ejecta gas that expands into the surrounding CSM. The interaction of the rapidly expanding ejecta

with the surrounding CSM creates two powerful shock fronts: an outward-moving forward shock (FS) that heats the CSM, and an inward-moving reverse shock (RS) that propagates back heating the metal-rich ejecta near the SNR center (e.g., a recent review by Dewey 2010). The FS is clearly identified in G292.0+1.8 as the outermost boundary of the remnant in X-rays (L10), in radio (GW03), and in infrared (Lee et al. 2009; Ghavamian et al. 2009; 2012). The location of the RS is difficult to ascertain because the 3D ejecta distribution is projected on the plane of the sky.

A useful method to probe the 3D structure of an SNR is to study the line-of-sight distribution of fast-moving ejecta knots by measuring their radial velocities (v_r). Mapping the 3D distribution of ejecta may help locate the RS front. The High Energy Transmision Grating Spectrometer (HETGS) on board *Chandra* provides a powerful high resolution spectroscopy to estimate Doppler shifts in the X-ray spectral lines of metal-rich ejecta knots, a measure of their v_r. The utility of this method has been successfully demonstrated with the bright ejecta-dominated SNR Cas A (e.g., Lazendic et al. 2006). Based on our *Chandra* HETGS observations, we apply a similar method to map the v_r distribution of 33 bright knots and filaments in G292.0+1.8. Here we provide the first insight into the 3D internal architecture of this textbook-type CC SNR in X-rays.

2.3 OBSERVATIONS & DATA REDUCTION

We performed our *Chandra* HETGS observation of G292.0+1.8 between 2011 March 20 and 2011 March 27. The aim point was set at RA(J2000.0) = 11^h 24^m $39^s.5$, Dec(J2000.0) = -595′ 56″.40 to detect a majority of bright ejecta knots within ∼2′ off-axis. The observation was composed of three ObsIDs (12555, 13242, and 13243). In each observation all six ACIS-S CCDs were operated in the full-frame readout mode. We processed the raw event files using CIAO version 4.4 and CALDB

version 4.4.3. We followed the standard data reduction methods involving grade and hot pixel filtering. We found no significant contamination from flaring background. We processed each ObsID individually, and all three ObsIDs were combined for data analysis to yield a total effective exposure of ∼114 ks. As supplementary data (see § 3), we also used the archival ACIS-I data of G292.0+1.8 (Park et al. 2007). We reprocessed all six ObsIDs of the ACIS-I data following standard data reduction procedures with CIAO version 4.3 and CALDB version 4.4.3, which resulted in a total effective exposure of 509 ks.

2.4 ANALYSIS & RESULTS

We extracted source spectra from numerous small regions in G292.0+1.8, and measured line center energies using methods similar to those applied for the study of ejecta knots in Cas A (Lazendic et al. 2006; Rutherford et al. 2013). We used a fixed order-sorting range of ±10% to extract the first-order spectrum (Figure 1). We created the zeroth-order image of the ObsID with the longest exposure (ObsID 12555) in the 0.8–2.2 keV band in which bright Kα lines from He- and H-like Ne, Mg and Si ions are present. Based on this image we identified the zeroth-order locations of bright, compact knots which would have small cross-dispersion widths (∼2″ – 9″ in angular sizes, and ∼4″ on average, for which the angular dispersion of these small source regions do not affect our Doppler line shift measurements). Using these line centers and cross-dispersion widths, we extracted the dispersed spectra from these small knots from all three ObsIDs applying standard CIAO tools – TGCat scripts.[1] We show an example of an HETGS spectrum extracted from a small bright emission feature in Figure 1.

[1] `http://tgcat.mit.edu/`

We analyzed the first-order spectra, corresponding to orders MEG ±1 and HEG ±1, using custom scripts executed in the ISIS software package[2] (Houck & Denicola 2000). For each knot, we combined the spectra extracted from all three ObsIDs. Five emission lines are useful for Doppler shift measurements of individual ejecta knots: atomic emission lines from the K-shell transitions in the He- and H-like ions of Ne and Mg, and in the He-like Si. The rest wavelengths for these lines are listed in Table 1. We detect and characterize these lines in the dispersed spectra of small knots in G292.0+1.8 using simple phenomenological model fits applied to a narrowband around each line. Our model consists of two Gaussians for the Lyα lines (one for the line and the other to approximate the underlying continuum) and four Gaussians for the Heα triplets (three corresponding to the forbidden (f), intercombination (i) and resonance (r) lines, and one for the underlying continuum). We use a sum of broad Gaussians to approximate the underlying continua in the five line-regions that we fit: the Gaussians provide a computationally simple method that allows each local continuum level to be adjusted with reasonable independence, since the Gaussians decrease quickly outside of their wavelength ranges. Free parameters in our model are the line center, the line flux, the line width (σ), and the continuum flux. For the continuum Gaussian component, we fixed the center energy at the rest wavelength of the corresponding line while varying the area of the Gaussian. The model fits for the Heα triplets have the same degrees of freedom as those of the Lyα lines, because the wavelength and fluxes of the f and i lines are set to be proportional to those of the r line. The i/r and f/r flux ratios we used were based on the observed values for Capella and SN 1987A (Canizares et al. 2000; Dewey et al. 2008) in which we assumed a low-density gas (which should also be the case for G292.0+1.8). We list these flux ratios in Table 1. We note that our primary goal of

[2]`http://space.mit.edu/CXC/ISIS/`

line shift measurements is not very sensitive to the exact ratios between these triplet lines. Also, the counting statistics dominate the observed line fluxes, and our Doppler velocity shift measurements are based on several emission line complexes (Table 2). For our Doppler velocity shift measurements, we first fitted each of the five lines listed above to detect a valid line feature. We scaled all the lines in the model to the model wavelength of the Ne IX line. The detected lines were then jointly fitted to estimate a common velocity shift. We fitted 65 small knots with these models, and used 33 knots that show statistically acceptable fits ($\chi^2/\nu < 2$, for a combined fit of all detected lines) for our Doppler shift measurements. We excluded 32 knots from our v_r measurements because their low signal-to-noise ratio did not allow us to detect valid line features. We show extracted spectra and best-fit models for three example regions in Figure 2. Based on the shifts in our measured line centers from the rest wavelengths, we estimate v_r for these knots (Table 2).

To identify the origins (shocked ejecta vs. CSM) of these 33 knots, we investigated their spectral properties using our deep 509 ks ACIS-I observation of G292.0+1.8 (Park et al. 2007). We used the ACIS data to utilize the significantly higher photon statistics (by more than an order of magnitude in the 0.3-5 keV band) than those in the HETG data . We performed spectral model fits for the observed ACIS spectra of these 33 regions to measure their metal abundances. For these spectral model fits we subtracted the background emission spectrum using spectra extracted from nearby source-free (dark, *ejecta-free*) regions within the SNR. We performed spectral model fits using the absorbed (*phabs* in XSPEC) non-equilibrium ionization (NEI) plane-parallel shock model (Borkowski et al. 2001) with variable abundances (*vpshock*, NEI version 2.0 with augmented ATOMDB, Smith et al. 2001; Badenes et al. 2006). We added a power law component for regions projected within or near the PWN. We varied O, Ne, Mg, Si, S and Fe abundances while fixing other

elemental abundances at solar values (Anders & Grevesse 1989). Based on these abundance measurements we identified 24 ejecta knots (showing abundances typically > several times solar for one or more elements). We identified 9 CSM-like features with sub-solar abundances for all fitted elements (Table 2). Most of the CSM features are positioned along the equatorial belt.

We constructed a v_r–r_p distribution for these 33 knots (Figure 3), where r_p is the projected distance from the expansion center. For a homologous expansion of ejecta knots in G292.0+1.8, the 3D spatial velocities (v_{3D}) of individual ejecta knots are proportional to their physical distances or 3D radii (r_{3D}) from the expansion center. The constant relating this proportionality is $r_{3D}/v_{3D} = 0.1055\ ''/\mathrm{km\,s^{-1}}$, assuming an expansion age of 3000 yr (Winkler et al. 2009) and a distance to the SNR of 6 kpc (GW03). Knots at the same r_{3D} will differ in their r_p and v_r values depending on their projected locations. In Figure 3 we overlay four elliptical loci to relate v_r and r_p from the SNR's expansion center, assuming this proportionality constant. The smallest elliptical locus corresponds to a physical distance (r_{3D} from the expansion center) of ∼3.5 pc (at the projected angular distance ∼120″) and roughly represents the angular size of the radio PWN, GW03). The next two loci at ∼3.8 pc (at ∼130″) and ∼6.4 pc (at ∼220″) have been qualitatively estimated by eyeball inspection to contain the majority of the ejecta knots within a shell. The outermost locus at ∼7.7 pc (∼265″) corresponds to the FS (L10). We roughly estimate (by eyes) the velocity centroid at +150 km s^{-1}which is similar to that estimated in the optical band (Ghavamian et al. 2005). We show the projected positions for the 33 regional features and these elliptical loci in Figure 4.

2.5 DISCUSSION

Our estimated radial velocity range of -2300 $\lesssim v_r \lesssim$ 1400 km s^{-1} for X-ray ejecta knots is in plausible agreement with earlier optical measurements of ejecta velocities in G292.0+1.8. Ghavamian et al. (2005) reported ejecta radial velocities in the range of -1700 $\lesssim v_r \lesssim$ +1700 km s^{-1} for O-rich optical ejecta knots in G292.0+1.8. Winkler et al. (2009) conducted proper motion studies of O-rich knots in the optical band, and measured east-west velocities of -1800 $d_6 < v_x <$ 1490 d_6 km s^{-1} and north-south velocities in the range of -3570 $d_6 < v_y <$ 2340 d_6 km s^{-1}, where d_6 is the distance to G292.0+1.8 in units of 6 kpc. While X-ray and optical emissions originate from ejecta gas with different thermal conditions, and thus X-ray ejecta knots generally do not show optical counterparts, we detect some spatial correlations between X-ray and optical ejecta knots. The highly redshifted knot E7 shows positional coincidence with the largely redshifted optical "spur" in the southeast region of the SNR, and the blueshifted knots E5 and E11 are in similar positions to blueshifted optical knots in the northern parts of the SNR. Spatial correlation between X-ray and optical emission is also supported by the observation that several X-ray filamentary structures in the north coincide with optical knots located near their termini (Figure 13 in Ghavamian et al. 2005). Thus, in G292.0+1.8 the ejecta gas at various thermal states appears to share some bulk motion.

We detect a significantly larger number of blueshifted knots than redshifted ones (17 of 24 ejecta knots are blueshifted). For the blueshifted ejecta knots, we also estimate generally higher velocity magnitudes than the redshifted ones: e.g., seven blueshifted knots show $v_r >$ 1000 km s^{-1} while only one redshifted ejecta knot shows such a high v_r. A similar non-symmetric v_r distribution of ejecta in G292.0+1.8 was observed in the optical band, where a significantly larger number of blueshifted knots was detected, especially in the north (Ghavamian et al. 2005). Asymmetries

in v_r have also been seen in other O-rich SNRs, for which interpretations included asymmetric SN explosions and density variations in the CSM. SNR 1E 0102.2–7219, in the Small Magellanic Cloud, shows a larger number of blueshifted bright knots but the redshifted knots show generally higher v_r (Vogt & Dopita 2010). SNR 0540-69.3, in the Large Magellanic Cloud (LMC), shows a generally redshifted spectrum of ejecta (Kirshner et al. 1989). SNR N132D, also in the LMC, shows higher v_r in its blueshifted ejecta (Vogt & Dopita 2011). Cas A shows higher v_r in its redshifted ejecta (Milisavljevic & Fesen 2013 and references therein).

Possible origins for the observed v_r asymmetry in G292.0+1.8 may include several scenarios such as an asymmetric SN explosion, CSM density variations (near vs. far sides of the SNR) along the line-of-sight, a clumpiness variation of the ejecta, and self-absorption of redshifted emission. We discuss each of these scenarios below. An asymmetric SN explosion may have channeled more kinetic energy towards the Earth along the line-of-sight. Observational evidence supporting an asymmetric SN explosion for G292.0+1.8 has been reported in previous works: e.g., higher X-ray ejecta temperatures in the northwest than in the southeast regions (Park et al. 2007), the absence of Si emission in the southeast (Park et al. 2002; Ghavamian et al. 2012), higher proper motions of optical ejecta knots along the north-south than in the east-west directions (Winkler et al. 2009), and the $\gtrsim$1 pc displacement (to southeast from the SNR's expansion center) of the associated pulsar PSR J1124-5916 (e.g., Winkler et al. 2009). In such an asymmetric SN explosion, the energy output might have resulted in a larger amount of blueshifted fast-moving ejecta material as observed in X-rays (this work) and in optical (Ghavamian et al. 2005).

Another tentative scenario for the observed v_r asymmetry could be a non-uniform CSM. For instance, a significant CSM density variation between the near and far sides of the SNR might have created asymmetry in the RS structure, causing

a greater inward migration of the RS on the near side (if the CSM density is higher there) than the far side, thus interacting with more ejecta material to produce more blueshifted material. A CSM density variation in G292.0+1.8 is suggested by large filamentary structures such as the equatorial belt (Park et al. 2004; Lee et al. 2009; L10; Ghavamian et al. 2012), and by a non-uniform circumstellar environment as seen in the mid-infrared (Park et al. 2007). Some azimuthal CSM density variation has been observed in G292.0+1.8 with regions in the southeast showing lower CSM densities than other regions (L10). However, it is not clear if this azimuthal CSM density structure orginated from variation in the progenitor's wind density or from an asymmetric SN explosion. Also, a deeper migration of the RS on the near side of the SNR would create more blueshifted material with lower v_r from the heating of slower moving central ejecta regions. One would therefore expect to see a larger number of low v_r blueshifted ejecta regions projected near the SNR center, which is not clearly evident. Hence, the presence and contribution of a CSM density variation along the line-of-sight between the near and far sides of the SNR that would result in the observed blueshift-dominated ejecta in G292.0+1.8 is unclear, although it cannot be ruled out.

A selection effect due to a clumpiness variation of the metal-rich ejecta in the SNR might also have contributed to the observed blueshift predominance in G292.0+1.8. Since we are more likely to select small bright knots (for our v_r measurements) that would originate in clumpier regions than in smoother plasma, an SNR with a substantially larger number of clumpy ejecta features on the near side could result in the observed blueshift predominance. An asymmetric clumpy ejecta distribution has been proposed to explain observed optical emission line asymmetries in SNe 1993J (Spyromilio 1994) and 1990I (Elmhamdi et al. 2004), with further support in theoretical studies (e.g., Herrington et al. 2010).

The observed v_r asymmetry in G292.0+1.8 might have originated from self-absorption of redshifted emission by material within the SNR (e.g., ejecta dust, Ghavamian et al. 2009; 2012). However, there is no observational evidence for significant self-absorption of X-ray emission that could lead to the observed v_r asymmetry in G292.0+1.8: e.g., we find that the column density (N_H) for the highly redshifted knot E7 is consistent with that for blueshifted regions. In general the existing observational evidence appears to favor an asymmetric explosion scenario for the observed v_r asymmetry. However, the true origin remains elusive.

Most of the ejecta knots in our study occupy a thick shell in v_r–r_p space, corresponding to the RS-heated hot ejecta gas (solid diamonds in Figure 3). On the other hand, most of the CSM filaments occupy the low v_r region (open circles in Figure 3), and are positioned along the equatorial belt (Figure 4). Unless our 24 ejecta knots represent a heavily biased sample, the inner and outer radii of this ejecta shell may roughly correspond to the locations of the RS ($r_{in} \sim 130''$) and contact discontinuity (CD, $r_{out} \sim 220''$) respectively (the projected angular distances r_{in} and r_{out} are measured from the explosion site determined from the proper motions of optical ejecta knots (Winkler et al. 2009)). We find that nearly all of 62 fast-moving optical ejecta knots (Ghavamian et al. 2005) also lie within our X-ray-estimated ejecta shell (we estimate that only two of them are positioned at a slightly larger radius than our CD), further supporting our inferred location of the RS. We note that there are a few regions with large uncertainties in v_r, likely due to the relatively weak emission lines in these features. For example, v_r measurements for regions C28, E29, C31 and E33 were based on only one, relatively faint line (Si Heα, Table 2).

Our estimate of the RS location gives a ratio between the radii of the RS and FS, R_{RS}/R_{FS} $\sim$130″/265″ $\sim$ 0.5. This ratio is consistent with previous estimates at other wavelengths: $\sim$0.47 by Braun et al. (1986) based on radio and infrared

data, and ∼0.5 by GW03, based on radio data. This R_{RS}/R_{FS} ratio in G292.0+1.8 is similar to that seen in other young O-rich SNRs: e.g., ∼0.6-0.8 for Cas A (at age ∼ 330 yr, HL12) and ∼0.5-0.7 for 1E 0102.2–7219 (at age ∼ 1000 yr, Gaetz et al. 2000; Flanagan et al. 2004). A smaller ratio of ∼0.3 was estimated in N132D (age ∼ 2500 yr) suggesting a dynamically more evolved stage for this SNR, with its RS possibly accelerating towards the SNR center (Vogt & Dopita 2011). Our estimated R_{RS}/R_{FS} ratio for G292.0+1.8 is significantly smaller than the values predicted by self-similar solutions ($R_{RS}/R_{FS} > 0.7$, Chevalier 1982), suggesting that this SNR has evolved beyond the early ejecta-dominated phase. Truelove & McKee (1999) (TM99 hereafter) developed a hydrodynamic framework that extends the model to later times when the RS reaches the ejecta core region and the FS approaches the late-time Sedov-Taylor phase. They presented explicit results for the SNR evolution in a uniform density medium. Laming & Hwang (2003) and HL12 (LH03-HL12 hereafter) extended the TM99 model for SNRs expanding into stellar winds with radial mass density profile $\rho \propto r^{-2}$. Since G292.0+1.8 is expanding into an RSG wind (L10), we applied the LH03-HL12 model for G292.0+1.8 and successfully reproduce our estimated R_{RS}/R_{FS} ~ 0.5 at age = 3000 yr. The age of ∼3000 yr has been estimated for G292.0+1.8 based on kinematic studies (Ghavamian et al. 2005; Winkler et al. 2009), which is similar to the characteristic spin-down age of PSR J1124-5916 in G292.0+1.8 (2900 yr, Camilo et al. 2002). For these model calculations we assumed a canonical explosion energy $E_0 = 1 \times 10^{51}$ erg, and a preshock CSM density 0.1-0.3 cm^{-3} at $R_{FS} = 7.7$ pc (L10). Based on the LH03-HL12 model, assuming the power-law index of $5 \lesssim n \lesssim 14$ for the ejecta radial density profile in the outer layers (with an inner *constant* density core) and SNR age of $2890 \lesssim t \lesssim 3080$ yr (Winkler et al. 2009), we calculate the total ejecta mass $M_{ej} \lesssim 8\ M_\odot$. Combining our upper limit for M_{ej} with our previously determined averaged wind mass estimate of $M_w \sim 25\ M_\odot$ (L10), we suggest an upper

limit of ∼35 $M_\odot$ for the progenitor mass (M_{prog}) of G292.0+1.8. This upper limit provides a constraint on M_{prog} based on the observed dynamics of the SNR, and is in plausible agreement with previous nucleosynthesis-based estimates for M_{prog}: e.g., 25 $M_\odot$ (Hughes & Singh 1994; Park et al. 2004), 30-40 $M_\odot$ (Gonzales & Safi-Harb 2003), 30-35 $M_\odot$ (Kamitsukasa et al. 2014) and 25-30 $M_\odot$ (Yang et al. 2014).

Considering the sharp boundary between the PWN and the outer plateau in radio, GW03 suggested an RS-PWN interaction, probably in the very early stage where the RS has not compressed the PWN significantly. On the other hand, a large pressure difference between the PWN and the thermal gas in X-rays had suggested that the RS and PWN had not yet interacted (Park et al. 2004). Also, a large O/Ne mass ratio in the mid-infrared suggested that the inner explosive nucleosynthesis products might not have undergone significant mixing, and could still remain unshocked (Ghavamian et al. 2009), which generally supports a non-interaction between the RS and PWN. Our estimated RS location is overall close to the outer boundary of the radio PWN (Figure 4). The position of the X-ray PWN in G292.0+1.8 is generally consistent with its radio counterpart, and the projected angular extent of the X-ray PWN is smaller than that of the radio PWN (Figure 5). This X-ray-radio PWN size difference is consistent with the standard picture of more effective synchrotron loss of X-ray emission in the outer layers of PWNs (e.g., Gaensler & Slane 2006). Theoretical and observational studies suggest that late stages of PWN-RS interactions are characterized by irregular PWN morphologies. These studies also suggest that asymmetry in the RS structure of SNRs will result in displacement of PWNs relative to their PSRs, and inconsistencies in the sizes and positions of radio PWNs and their X-ray counterparts in late PWN-RS interaction stages (e.g., Gaensler & Slane 2006 and references therein). These signs of late-stage PWN-RS interactions are not clearly evident in G292.0+1.8. Therefore, a PWN-RS interaction, if it has started,

should be in an early stage in this SNR (as suggested by GW03). We note that Park et al. (2004) estimated the thermal pressure of the SNR using only a small region on the equatorial belt. The RS front in G292.0+1.8 may not be smooth or spherically symmetric after interacting with a non-uniform CSM. Then we consider that the large pressure difference between the PWN and thermal gas estimated by Park et al. (2004) might have been a local effect. X-ray thermal pressure measurements from extensive areas of the SNR would be helpful to test this discrepancy (which is beyond the scope of this paper, and will be included in our follow-up work on the ACIS-I data analysis). If the RS front is close to the PWN (and probably interacting with it), it may be nearing the SNR's central region where the Fe-rich ejecta might be expanding. A recent *Suzaku* detection of the Fe K-shell emission line in the hot ejecta gas of G292.0+1.8 (Kamitsukasa et al. 2014) may support this scenario, opening further avenues in the quest to decipher this complex remnant.

2.6 SUMMARY

Based on our ∼114 ks *Chandra* HETGS observation of G292.0+1.8, we measure v_r from Doppler line shifts for 33 bright knots in the SNR. Our measured v_r is in the range of -2300 $\lesssim v_r \lesssim$ 1400 km s^{-1}. We detect a v_r asymmetry with a larger number of blueshifted ejecta knots than redshifted ones. Our measured v_r range and observed blueshifted ejecta knot predominance are generally consistent with results from optical observations (Ghavamian et al. 2005). We find that the blueshifted X-ray ejecta knots generally show higher velocity magnitudes than the redshifted ones. Other O-rich SNRs have also been found to show v_r asymmetry. The cause for the v_r asymmetry in G292.0+1.8 may have been an asymmetric SN explosion, although environmental effects such as CSM density variations along the line-of-sight cannot be ruled out. Based on the distribution of the ejecta knots in v_r–r_p space, we

qualitatively locate the positions of the RS and CD. Our inferred RS position agrees with previous estimates based on radio and IR data, and with the hydrodynamic model for an SNR expanding into an RSG wind. Employing the SNR's dynamics we calculate the total ejecta mass of $\lesssim 8$ $M_\odot$, and propose an upper limit of $\sim$35 $M_\odot$ for the G292.0+1.8 progenitor mass. Our inferred location of the RS places it in close proximity to the outer boundary of the PWN, suggesting the possibility of early-stage PWN-RS interactions, and the possible onset of inner Fe-rich ejecta-heating by the RS.

This work was supported in part by the SAO through *Chandra* grant GO1-12077X. JB acknowledges support from the NASA Texas Space Grant Consortium. DD was supported by NASA through SAO contract SV3-73016 to MIT for support of the *Chandra* X-ray Center and Science Instruments.

REFERENCES

[Anders & Grevesse (1989)] Anders, E. & Grevesse, N. 1989, Geochim. Cosmochim. Acta, 53, 197

[Badenes (2006)] Badenes, C., Borkowski, K. J., Hughes, J. P., Hwang, U., & Bravo, E. 2006, ApJ, 645, 1373

[Borkowski et al.(2001)] Borkowski, K. J., Lyerly, W. J., & Reynolds, S. P. 2001, ApJ, 548, 820

[Braun et al.(1986)] Braun, R., Goss, W. M., Caswell, J. L., & Roger, R. S. 1986, A & A, 162, 259

[Camilo et al.(2002)] Camilo, F., Manchester, R. N., Gaensler, B. M., Lorimer, D. R., & Sarkissian, J. 2002, ApJ, 567, L71

[Chevalier (1982)] Chevalier, R. A. 1982, ApJ, 258, 790

[Chevalier (2005)] Chevalier, R. A. 2005, ApJ, 619, 839

[Canizares et al.(2000)] Canizares. C. R., Huenemoerder, D. P., Davis, D.S., et al. 2000, ApJ, 539, L41

[Dewey et al. (2008)] Dewey, D., Zhekov, S. A., McCray, R. & Canizares, C. R. 2008, ApJ, 676, L131

[Dewey (2010)] Dewey, D. 2010, SSRv, 157, 229

[Drake (1988)] Drake, G.W. 1988, Can. J. Physics 66, 586

[Elmhamdi et al. (2004)] Elmhamdi, A., Danziger, I. J., Cappellaro, E., et al. 2004, A & A, 426, 963

[Flanagan et al. (2004)] Flanagan, K. A., Canizares, C. R., Dewey, D., et al. 2004, ApJ, 605, 230

[Gaensler & Wallace (2003)] Gaensler, B. M. & Wallace, B. J. 2003, ApJ, 594, 326 (GW03)

[Gaensler & Slane (2006)] Gaensler, B. M. & Slane, P. O. 2006, ARA&A, 44, 17

[Gaetz et al. (2000)] Gaetz, T. J., Butt, Y. M., Edgar, R. J., et al. 2000, ApJ, 534, L47

[Ghavamian et al. (2005)] Ghavamian, P., Hughes, J. P., & Williams, T. B. 2005, ApJ, 635, 365

[Ghavamian et al. (2009)] Ghavamian, P., Raymond, J. C., Blair, W. P., et al. 2009, ApJ, 696, 1307

[Ghavamian et al. (2012)] Ghavamian, P., Long, K. S., Blair, W. P., et al. 2012, ApJ, 750, 39

[Gonzalez & Safi-Harb (2003)] Gonzalez, M. & Safi-Harb, S. 2003, ApJ, 583, L91

[Herrington (2010)] Herrington, J., Ignace, R. & Hole, T. K., 2010, JSARA, 4, 15

[Houck & Denicola (2000)] Houck, J. C. & Denicola, L. A. 2000, in ASP Conf. Ser. 216, Astronomical Data Analysis Software and Systems IX, ed. N. Manset, C. Veillet, & D. Crabtree, (San Francisco, CA:ASP), 591

[Hughes & Singh (1994)] Hughes, J. P. & Singh, K. P. 1994, ApJ, 422, 126

[Hughes et al. (2001)] Hughes, J. P., Slane, P. O., Burrows, D. N., et al. 2001, ApJ, 559, L153

[Hughes et al. (2003)] Hughes, J. P., Slane, P. O., Park, S., Roming, P. W. A., & Burrows, D. N. 2003, ApJ, 591, L139

[Hwang & Laming (2012)] Hwang, U. & Laming, J. M. 2012, ApJ, 746, 130 (HL12)

[Johnson & Soff (1985)] Johnson, W.R., & Soff, G. 1985, ADNDT, 33, 405

[Kamitsukasa et al. (2014)] Kamitsukasa, F., Koyama, K., Tsunemi, H., et al. 2014, PASJ, 66, 648

[Kirshner et al. (1989)] Kirshner, R. P., Morse, J. A., Winkler, P. F., & Blair, W. P. 1989, ApJ, 342, 260

[Laming & Hwang (2003)] Laming, J. M. & Hwang, U. 2003, ApJ, 597, 347 (LH03)

[Lazendic et al. (2006)] Lazendic, J. S., Dewey, D., Schulz, N. S., & Canizares, C. R. 2006, ApJ, 651, 250

[Lee et al. (2009)] Lee, H.-G., Koo, B.-C., Moon, D.-S., et al. 2009, ApJ, 706, 441

[Lee et al. (2010)] Lee, J.-J., Park, S., Hughes, J. P., et al. 2010, ApJ, 711, 861 (L10)

[Milisavljevic et al. (2013)] Milisavljevic, D. & Fesen, R. A. 2013, ApJ, 772, 134

[Park et al. (2002)] Park, S., Roming, P. W. A., Hughes, J. P. et al. 2002, ApJ, 564, L39

[Park et al. (2004)] Park, S., Hughes, J. P., Slane, P. O., et al. 2004, ApJ, 602, L33

[Park et al. (2007)] Park, S., Hughes, J. P., Slane, P. O., et al. 2007, ApJ, 670, L121

[Rutherford et al. (2013)] Rutherford, J., Dewey, D., Figueroa-Feliciano, E., et al. 2013, ApJ, 769, 64

[Smith (2001)] Smith, R. K., Brickhouse, N. S., Liedahl, D. A. & Raymond, J. C. 2001, ApJ, 556, L91

[Spyromilio (1994)] Spyromilio, J. 1994, MNRAS, 266, L61

[Truelove (1999)] Truelove, J. K., & McKee, C. F. 1999, ApJS, 120, 299

[Vogt & Dopita (2010)] Vogt, F. & Dopita, M. A., 2010, ApJ, 721, 597

[Vogt & Dopita (2011)] Vogt, F. & Dopita, M. A., 2011, Ap&SS, 331, 521

[Winkler & Long (2006)] Winkler, P. F. & Long, K. S. 2006, ApJ, 132, 360

[Winkler et al. (2009)] Winkler, P. F., Twelker, K., Reith, C. N., & Long, K. S. 2009, ApJ, 692, 1489

[Yang et al. (2014)] Yang, X.-J., Liu, X.-Q., Li, S.-Y., & Lu, F.-J. 2014, RAA, 14, 1279

Table 2.1. Emission Lines used for Doppler Shift Measurements

Ion/transition	Rest Wavelength[a] (Å)	Flux ratios	
		i/r [b]	f/r [b]
Ne IX r (Ne Heα r)	13.447	0.26	0.59
Ne IX i (Ne Heα i)	13.553	–	–
Ne IX f (Ne Heα f)	13.699	–	–
Ne X (Ne Lyα)	12.134	–	–
Mg XI r (Mg Heα r)	9.169	0.21	0.43
Mg XI i (Mg Heα i)	9.231	–	–
Mg XI f (Mg Heα f)	9.314	–	–
Mg XII (Mg Lyα)	8.421	–	–
Si XIII r (Si Heα r)	6.648	0.23	0.43
Si XIII i (Si Heα i)	6.688	–	–
Si XIII f (Si Heα f)	6.740	–	–

[a]The H-like Lyα line values are from Johnson & Soff 1985, and the He-like line values are from Drake 1988.

[b]The Ne IX and Si XIII ratios are based on the observed flux ratios for SN 1987A, and the Mg XI ratios are based on the observed flux ratios for Capella and SN 1987A (Canizares et al. 2000; Dewey et al. 2008). We assume a low-density gas which should also be the case for G292.0+1.8. The letters r, i and f indicate the resonance, intercombination and forbidden transitions respectively in the He-like ions.

Table 2.2. Radial Velocities of X-ray Emission Features in G292.0+1.8

Knot ID	Arc seconds (from center) [a]	Position angle (deg) [b]	v_r — km s^{-1} —	± 90%	χ^2/ν	Lines used [c]	Knot origin
E 1	125.8	102.4	41	± 297	1.59	1, 2, 3, 4	Ejecta
E 2	182.7	80.9	-496	± 289	1.87	1, 2, 3, 4	Ejecta
C 3	221.9	252.1	677	± 751	1.30	2, 3, 5	CSM
E 4	96.3	181.3	-2221	± 407	1.48	2, 3, 4	Ejecta
E 5	134.0	48.9	-981	± 435	1.60	2, 3, 4	Ejecta
C 6	62.5	90.0	-503	± 2810	1.34	1, 2	CSM
E 7	54.3	117.7	1396	± 271	1.68	1, 2, 3, 4	Ejecta
C 8	15.4	97.5	-792	± 655	1.94	2, 3, 5	CSM
C 9	43.1	276.7	-990	± 693	1.29	1, 2, 3, 5	CSM
E 10	92.1	248.9	-1822	± 719	1.30	1, 2, 3, 5	Ejecta
E 11	75.0	330.5	-1289	± 923	1.39	2, 5	Ejecta
E 12	69.7	306.2	-1623	± 342	1.40	1, 3, 5	Ejecta
E 13	156.0	324.8	-479	± 235	1.40	1, 2, 3, 4, 5	Ejecta
E 14	198.2	307.3	-269	± 633	1.88	2, 3, 4	Ejecta
E 15	172.1	301.2	-78	± 332	1.59	1, 2, 3, 4, 5	Ejecta
C 16	56.8	269.0	107	± 410	1.51	1, 2, 3, 5	CSM
E 17	203.2	333.2	320	± 413	1.57	2, 3, 4, 5	Ejecta
E 18	193.4	24.0	-115	± 603	1.15	3, 5	Ejecta
E 19	57.3	210.8	-453	± 712	1.57	2, 3, 4	Ejecta
E 20	209.9	9.0	785	± 1048	1.01	1, 2	Ejecta
E 21	147.3	289.9	381	± 657	1.66	1, 2, 3, 4	Ejecta
E 22	203.0	355.8	839	± 452	1.33	2, 3	Ejecta
E 23	140.9	143.0	-1346	± 313	1.05	2, 3, 4	Ejecta
E 24	145.1	144.0	-1074	± 271	1.14	1, 2, 3, 4	Ejecta
E 25	56.5	295.2	-1007	± 528	1.85	2	Ejecta
E 26	147.6	322.7	-610	± 246	1.29	1, 2, 3, 4	Ejecta
E 27	163.1	328.9	-230	± 389	1.19	2, 3, 4	Ejecta
C 28	123.3	264.4	-3087	± 1502	1.26	5	CSM
E 29	172.2	245.2	394	± 1763	1.15	5	Ejecta
C 30	85.6	265.3	-420	± 778	1.04	2	CSM

Table 2.2 (cont'd)

Knot ID	Arc seconds (from center) [a]	Position angle (deg) [b]	v_r — km s^{-1} —	± 90%	χ^2/ν	Lines used [c]	Knot origin
C 31	109.6	52.2	-811	± 1528	1.74	5	CSM
C 32	129.6	353.5	-405	± 765	1.57	1, 3	CSM
E 33	76.9	336.0	-2301	± 1799	1.39	5	Ejecta

[a] Angular distance from the the optical expansion center given by Winkler et al. 2009: R.A. = $11^h24^m34.4^s$, Decl. = $-59°15'51''$ (J2000);

[b] Measured counterclockwise, north to east;

[c] The lines used in fitting are: 1 = Ne IX, 2 = Ne X, 3 = Mg XI, 4 = Mg XII and 5 = Si XIII.

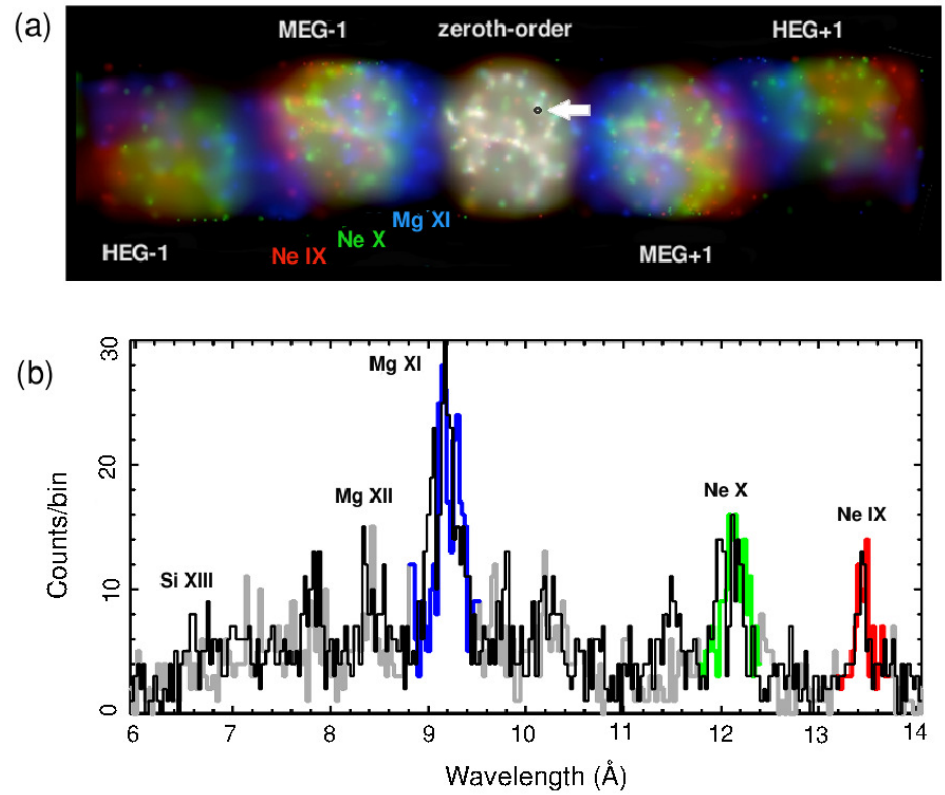

Figure 2.1 (*a*): Dispersed image of the spectrum for G292.0+1.8 showing the zeroth order in the center and the first order, color coded by energy. Red: Ne IX (0.90–0.93 keV), green: Ne X (1.02–1.06 keV) and blue: Mg XI (1.33–1.38 keV). (*b*): Combined MEG spectrum for knot E13 (identified by an arrow on the zeroth order image in (*a*)), showing the Si XIII, Mg XII, Mg XI, Ne X and Ne IX lines used in the Gaussian fit. Black: MEG -1, gray: MEG +1. For comparisons, the MEG +1 data (gray) corresponding to the Mg XI, Ne X and Ne IX lines in the lower panel are highlighted using the same color scheme as in the top panel.

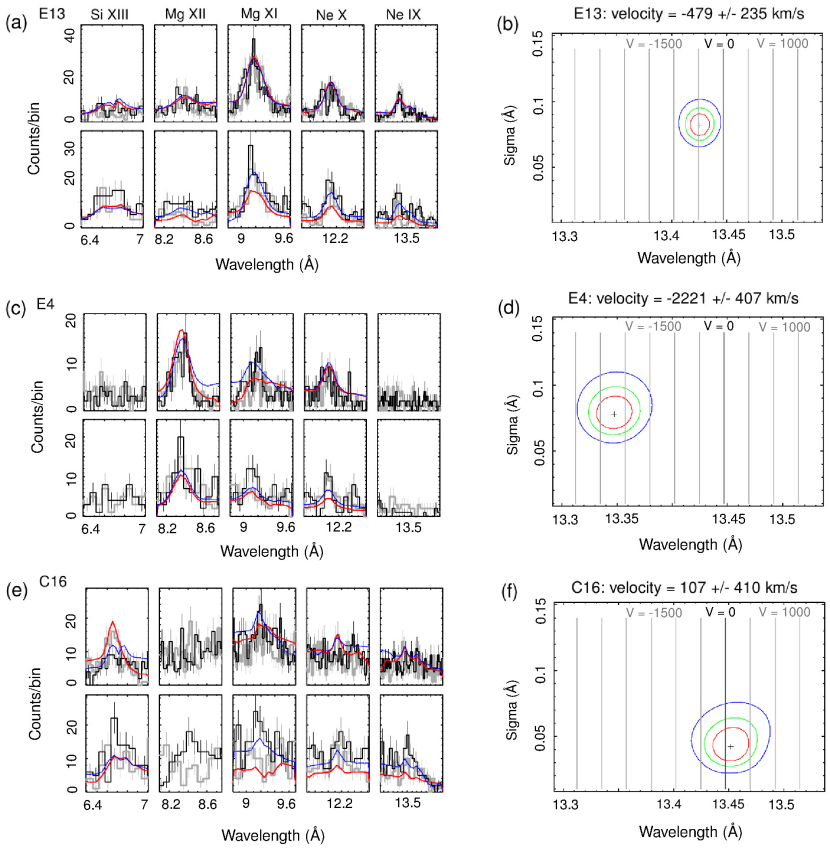

Figure 2.2 *Left* (*a, c, e*): Best-fit joint Gaussian model fits for detected lines (Si XIII, Mg XII, Mg XI, Ne X and Ne IX) for three sample regions. For each region MEG spectra are in the upper panel and HEG spectra are in the lower panel. Black: -1 order data, gray: +1 order data, blue: best-fit model for -1 order, red: best-fit model for +1 order. *Right* (*b, d, f*): confidence contour plots (68% (red), 90% (green), 99% (blue)) for the combined fitting of all detected lines. To make these contour plots we first fitted each of the five lines to detect a valid line feature. The detected lines (shown with red and blue model fit curves on the left), were then fitted jointly to estimate a common velocity shift. All of the lines in the model are scaled to the wavelength of the Ne IX model line. The wavelength of the Ne IX line center is plotted on the horizontal axis, and the common width of the lines is on the vertical axis. Starting at the top the regions are (*a, b*): knot E13, a region with a large radial distance and low velocity, (*c, d*): knot E4, a region with a small radial distance and high velocity, and (*e, f*): knot C16, a CSM filament located at the equatorial belt showing a low velocity.

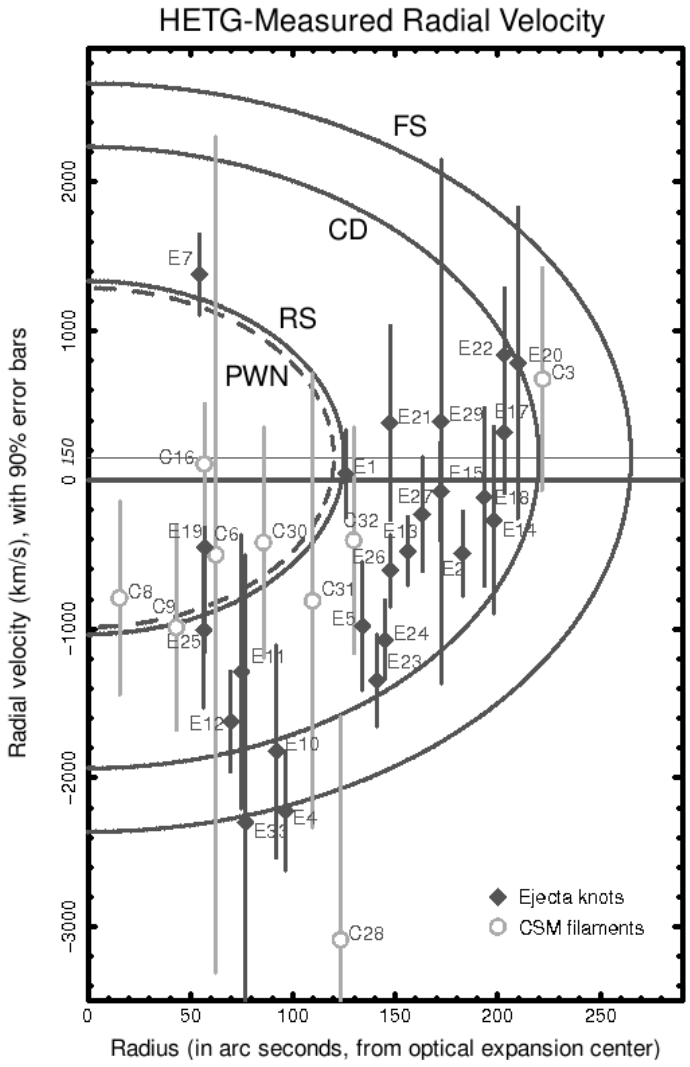

Figure 2.3 Radial velocity vs. projected distance from the optical expansion center for 33 knots. The error bars indicate the 90% confidence range. The elliptical loci represent expanding spherical shells of ejecta at different radial distances from the center in v_r–r_p space. Each curve is the locus of the same distance from the SNR expansion center, but with different v_r observed along the line-of-sight. Radius and velocity on these elliptical loci are related through a proportionality constant based on a homologous expansion age of 3000 yr. The line at +150 km s^{-1} is our estimate of the v_r centroid for the elliptical loci. The dashed line roughly shows the outermost boundary of the radio PWN. The next two solid lines mark the inferred locations of the RS and CD. The outermost line at 265″ marks the FS.

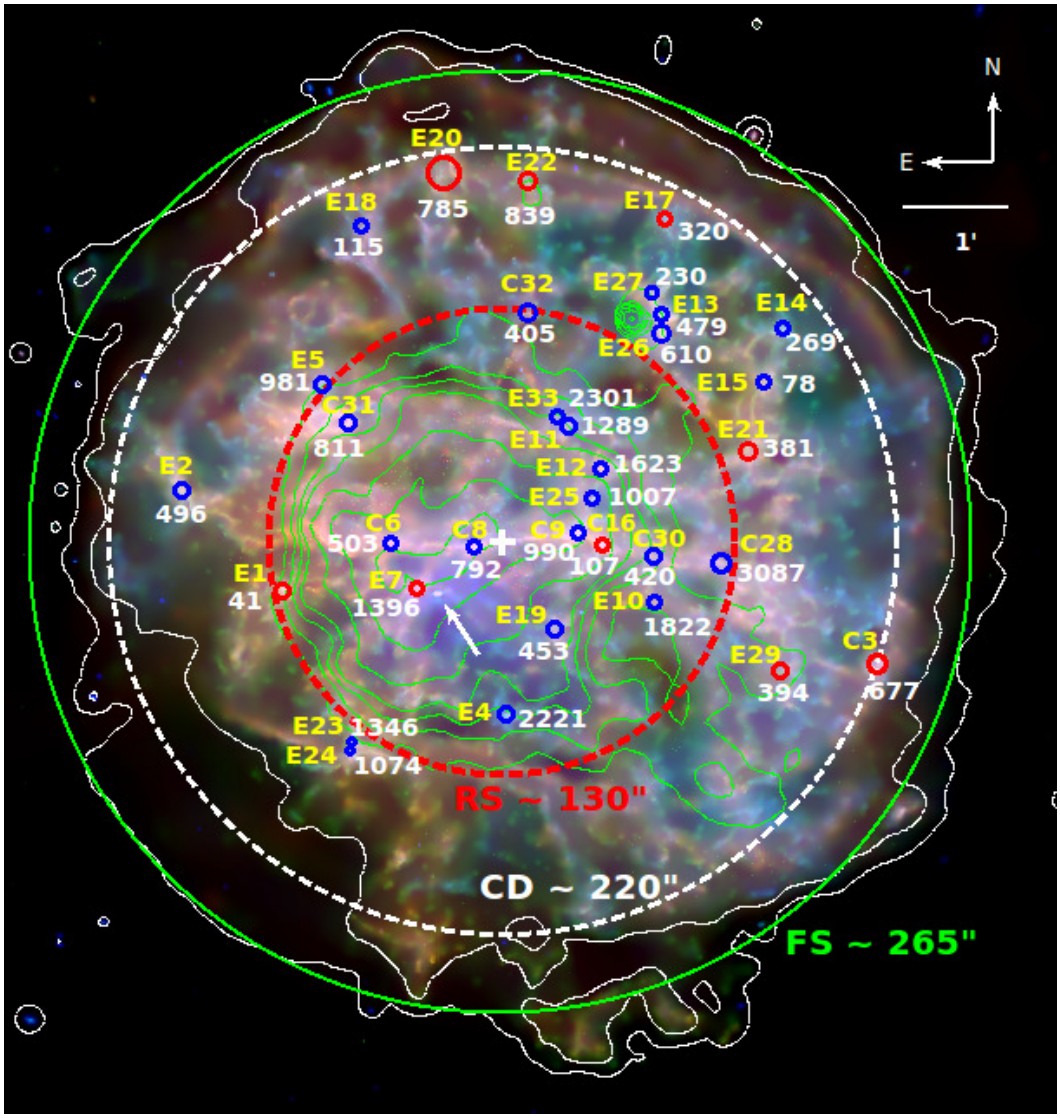

Figure 2.4 ACIS-I three-color image showing locations, identification numbers (yellow) and radial velocities (white) of 33 knots. Color codes for the image are: red = 0.3-0.8 keV, green = 0.8-1.7 keV and blue = 1.7-8.0 keV. The prefixes for the IDs are E for metal-rich ejecta, C for shocked CSM. Regions for blueshifted knots are marked with blue circles, while those for redshifed knots are marked with red circles. The optical expansion center is marked by a white cross and the pulsar PSR J1124-5916 by a white arrow. The dashed red and white circles show the locations of the RS and CD, respectively, that we infer from the ejecta distribution (Figure 3). The large green circle shows the location of the FS at 7.7 d_6 ($\sim$265″). The RS, CD and FS circles are all centered at the optical expansion center. The 20 cm map of the radio PWN is overlaid with green contours. The overlaid white contours are the outer boundary of the SNR in X-rays (based on the 0.3-8 keV broadband ACIS image).

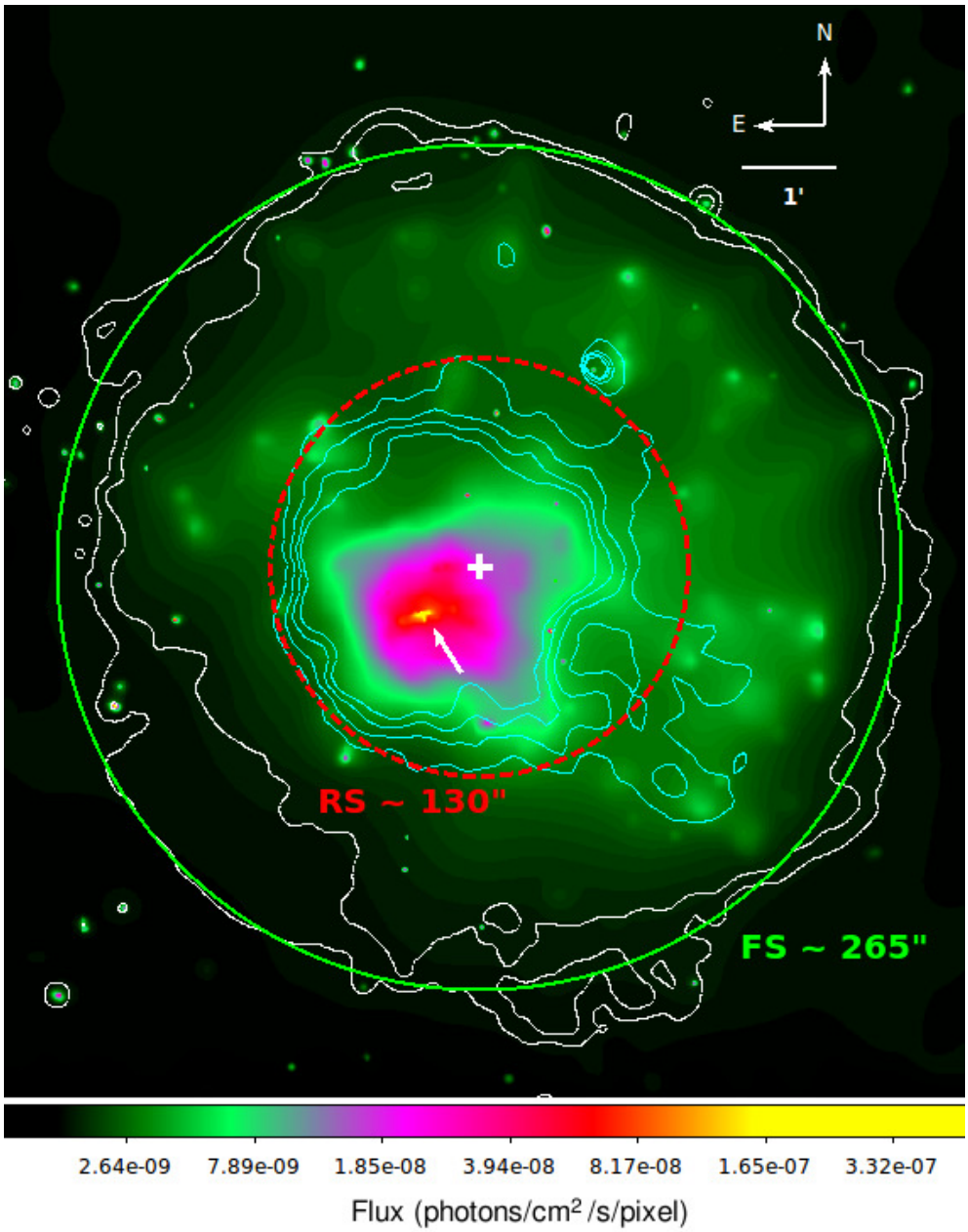

Figure 2.5 The 4-8 keV band ACIS-I image of G292.0+1.8. The image has been exposure corrected, binned by 2 × 2 pixels and adaptively smoothed. The arrow marks the pulsar PSR J1124-5916, and the cross indicates the optical expansion center. The inferred location of the RS (as marked in Figure 4) is represented by the dashed red circle at ∼130″ from the SNR's center, and the FS is indicated by a green circle at ∼265″. Overlaid are the outer contours of the 20 cm map of the radio PWN (cyan), and the X-ray contours (based on the 0.3-8 keV broadband ACIS image) marking the outer boundary of the SNR (white).

CHAPTER 3

Detailed X-ray Mapping of the Shocked Ejecta and Circumstellar Medium in the Galactic Core-Collapse Supernova Remnant G292.0+1.8

Jayant Bhalerao[1], Sangwook Park[1], Andrew Schenck[1], John P. Hughes,[2] and Seth Post[1]

[1] Department of Physics, University of Texas at Arlington, P.O. Box 19059, Arlington, TX 76019, USA

[2] Department of Physics and Astronomy, Rutgers University, 136 Frelinghuysen Road, Piscataway, NJ 08854-8019, USA

3.1 ABSTRACT

G292.0+1.8 (G292) is a young ($\sim$3000 yr), Galactic textbook-type core-collapse supernova remnant (CCSNR). It is marked by X-ray, optical and infrared emission from ejecta and circumstellar medium (CSM) features, and contains a pulsar (PSR J1124-5916) and pulsar wind nebula that have been observed in X-rays and radio. Previous studies reveal a complex, dynamically evolving, oxygen-rich remnant, a striking relic from the explosion of a massive star. Here, using our deep (530 ks) *Chandra* ACIS data, we present high-resolution maps of the shocked CSM and metal-rich ejecta in G292. We make the first *Chandra*-detection of Fe-rich ejecta in G292. We identify the X-ray counterpart of the northern equatorial belt, a component of a ring-like CSM structure identified earlier in the infrared band. We show the detailed spatial distributions of ejecta enriched in O, Ne, Mg, Si, S and Fe. We find that the bulk of the Si, S and Fe-rich ejecta are located in the northwestern hemisphere of the remnant, as opposed to the pulsar's projected angular displacement to the southeast from the SNR's center. This suggests that the pulsar's kick may have originated from gravitational and hydrodynamic forces during an asymmetric explosion, rather than from anisotropic neutrino emission. Based on abundance ratios and our estimated CSM and ejecta masses, we constrain the progenitor mass to 13 $M_{\odot} \lesssim M \lesssim 30\ M_{\odot}$

Key words: ISM: individual objects (G292.0+1.8) – ISM: supernova remnants – ejecta, CSM, circumstellar ring, mapping, iron, progenitor mass, nucleosysnthesis, asymmetry, neutron star – X-rays: ISM, individual (G292.0+1.8)

3.2 INTRODUCTION

Oxygen, a key component of life, is produced by nuclear fusion in the cores of massive stars and released into the interstellar medium when these stars explode as supernovae (SNe). G292.0+1.8 (G292 hereafter) is one of three known Galactic oxygen-rich core-collapse supernova remnants (CCSNR, Goss et al. 1979). The other two in this group are Cassiopeia A (Cas A) and Puppis A (e.g., Ghavamian et al. 2005 and references therein). These remnants are characterized by the detection of high oxygen abundances relative to other elements. The oxygen is produced by nuclear burning processes in the interiors of the massive progenitor stars that spawned these remnants. Oxygen and other nucleosynthesis products are ejected into interstellar space as SN ejecta when these stars explode as CCSN. Among these three Galactic oxygen-rich remnants, only G292 shows all the *textbook-type* features of a CCSNR: metal-rich ejecta, shocked circumstellar medium (CSM), a rotation-powered neutron star (NS or pulsar, PSR J1124-5916) and pulsar wind nebula (PWN) detected both in X-rays and in radio (Hughes et al. 2001, 2003; Camilo et al. 2002; Gaensler & Wallace 2003). In contrast, Puppis A is dominated by emission from shocked gas with a low-abundant CSM and/or ISM-like composition (Hwang et al. 2008; Katsuda et al. 2008; Luna et al. 2016). The NS in Puppis A has a weak magnetic field and is radio-quiet (Gotthelf & Halpern, 2009). Cas A differs in having ejecta that are unusually low in Ne and Mg abundance, and are dominated by Si, S and Fe (Vink et al. 1996; Dewey et al. 2007). The NS in Cas A does not pulsate and it is not surrounded by a PWN (e.g., Pavlov et al. 2000; Vink 2008). G292's textbook features make it very useful for studying the evolutionary processes of stars, massive-enough to eventually explode as "standard" CCSNe and create normal pulsars.

G292 is the result of an unrecorded SN explosion in an area of the southern sky marked by the bright constellation *Centaurus*. Its age of ∼3000 yr was estimated from

the observed expansion rates of fast-moving optical ejecta knots in the optical band (Ghavamian et al. 2005; Winkler et al. 2009) and from the Sedov interpretation of the its X-ray shell emission spectrum (Gonzalez & Safi-Harb 2003). This age estimate is consistent with the characteristic spin-down age of G292's pulsar (2900 yr, Camilo et al. 2002). The distance to G292 has been estimated to be $\gtrsim$6 kpc using H I absorption measurements (Gaensler & Wallace 2003). G292 has an angular size of $\sim 9'$ in X-ray (Park et al. 2007) and in radio (Gaensler & Wallace 2003), which corresponds to a diameter of $\sim$16 pc at $d = 6$ kpc.

The X-ray morphology of G292 exhibits a rich, and intricate pattern of ejecta and CSM structures. The ejecta form networks of knots and filaments distributed over the face of the entire remnant. Superimposed on the ejecta is the shocked CSM, which manifests as several distinctive morphological structures in X-rays: the equatorial belt, thin circumferential filaments, and the outermost diffuse, spectrally soft emission (Gonzalez & Safi-Harb 2003; Park et al. 2002, 2004, 2007). The equatorial belt is a dense, belt-like feature running along the SNR's "equator." It has been observed in the optical band (Ghavamian et al. 2005), in infrared (Lee et al. 2009; Ghavamian et al. 2012; Ghavamian & Williams 2016) and in X-rays (e.g., Tuohy et al. 1982; Hughes et al. 2001; Park et al. 2002, 2004, 2007). The thin circumferential filaments form narrow arcs of spectrally soft emission along the outer boundary of the SNR (Gonzalez & Safi-Harb 2003; Park et al. 2002, 2007). Finally, the CSM forms a diffuse, spectrally soft border along the outer edge of the SNR which marks the region where the forward shock (FS) is interacting with the red supergiant (RSG) winds of the progenitor (Park et al. 2007; Lee et al. 2010). The suggested origins for these CSM emission features may include relic structures from the outer atmosphere of a rotating progenitor star, and/or from binary interactions (e.g., Chevalier 1992; Chita et al. 2008; Morris & Podsiadlowski 2009; Smith et al. 2013).

The ejecta in G292 are characterized by high velocity ($v_{radial} \gtrsim 1000$ km s^{-1}) knots and filaments (Ghavamian et al. 2005; Bhalerao et al. 2015). The bulk of the shocked metal-rich ejecta in G292 is dominated by O, Ne and Mg (e.g., Park et al. 2004). Relatively weak Fe K-shell line emission from the Fe-rich ejecta gas has been detected in *Suzaku* data (Kamitsukasa et al. 2014; Yamaguchi et al. 2014), however the poor angular resolution of *Suzaku* ($\sim 2'$ HPD, Mitsuda et al. 2007) hindered its accurate spatial mapping. The location of the reverse shock (RS) close to the outer edge of the PWN in G292 (Gaensler & Wallace, 2004; Bhalerao et al. 2015) suggests that the interaction of the RS with the central ejecta may have recently started, therefore the bulk of the innermost ejecta, representing explosive nucleosynthesis products such as Fe, may not have been heated by the RS yet. Unlike Cas A, significant mixing and overturning of ejecta in G292 may not have occurred (Park et al. 2004; Ghavamian et al. 2012).

Previous studies have sampled a limited number of ejecta regions using *Chandra* data (Gonzales & Safi-Harb 2003; Park et al. 2004, 2007). More extensive regions of G292 have been analyzed using a regional grid (Yang et al. 2014), however, this study was based on *Chandra* Advanced CCD Imaging Spectrometer-S3 (ACIS-S3) data with incomplete coverage of the SNR because of the detector's smaller field of view ($8.3' \times 8.3'$, Weisskopf et al. 2005). In this paper, we use data collected with the *Chandra* ACIS-I array, which has a larger field of view ($17' \times 17'$) and covers the entire SNR. Furthermore, the ACIS-I data we use here has an order of magnitude longer exposure than the ACIS-S3 data.

Evidence for a strong link between asymmetric SN explosions and "NS-kicks" (forces imparted to the NS during the SN explosion) is emerging (e.g., Janka 2017 and references therein). In G292, evidence for an asymmetric explosion has been suggested. Si-rich ejecta gas is observed mainly in the north and northwest of the

SNR (Park et al. 2002; Ghavamian et al. 2012; Yang et al. 2014). Radial velocity measurements detect a significantly larger number of blueshifted knots compared to redshifted ones (Ghavamian et al. 2005; Bhalerao et al. 2015). Also, the radial velocity magnitudes of the blueshifted knots are generally higher than those of the redshifted ones (Bhalerao et al 2015). Oxygen-rich ejecta filaments in the optical band, show higher proper motions in the north-south direction than in the east-west direction (Winkler et al. 2009).

The detailed distribution of Fe-rich ejecta in G292 has not been known. Fe is a key explosive nucleosynthesis product, produced in the deepest layers of the SN, and its spatial distribution, especially asymmetric patterns, would be crucial for revealing the nature of the CCSN explosion (Woosley et al. 2002; Thielemann et al. 2007; Maoz & Graur 2017).

Here, using our deep *Chandra* ACIS-I data, we perform a detailed spectroscopic analysis of the entire remnant. This study is a direct expansion of our earlier studies of G292 based on the same *Chandra* data (Park et al. 2007; Lee et al. 2010). In this paper, we reveal G292's structure, morphology and distribution of the CSM and ejecta in unprecedented detail. We for the first time provide a high-resolution map revealing the spatial distribution of Fe-rich ejecta in G292. We also provide spatial distribution maps for O-, Ne-, Mg-, Si- and S-rich ejecta, and their thermodynamic parameters including the electron temperature and ionization timescale. We discuss these results in the context of recent CCSN hydrodynamic models, and their implications in understanding the nature of CCSN explosions.

3.3 OBSERVATIONS & DATA REDUCTION

Our G292 observation was performed between 2006 September 13 and 2006 October 20 using ACIS-I array. We used the ACIS-I array since it has a large field

of view ($17' \times 17'$, Weisskopf et al. 2005) and can cover the entire SNR (angular size $\sim 9'$, Park et al. 2007). The observation consisted of six individual ObsIDs with exposure times ranging from ∼40 ks to 160 ks (Table 1). The aim point was close to the position of the pulsar (PSR J1124-5916) at R.A. (J2000.0) = $11^h24^m39^s.1$, decl. (J2000) = -596′20″(Camilo et al. 2002; Hughes et al. 2003). We processed the data with standard data reduction methods for grade and hot pixel filtering using the Chandra Interactive Analysis of Observations (CIAO) software version 4.7, with calibration database CALDB 4.6.7. No significant background flaring was observed. The processed data had a total effective exposure time of ∼509 ks. We note that after we had completed our analysis for this work using our 2006 observation, additional ACIS-I data of G292 (with a total exposure of ∼300 ks, taken in 2016) became available in the archive. Considering the time-dependent quantum efficiency degradation of the ACIS-I detector, we estimate that these additional data would only marginally increase the photon statistics (by ∼40%), and thus would not affect our scientific conclusions. Thus, we do not include these additional *Chandra* archival data of G292 in this work.

3.4 ANALYSIS & RESULTS

3.4.1 Characterization of the Outermost Shocked CSM

We divided the remnant into a sub-regional grid using our adaptive mesh method (Schenck et al. 2016). This technique adaptively divides the SNR into small rectangular sub-regions, to contain a certain minimum number of counts per sub-region. We used the 0.3-8 keV band image of G292 to apply this method. To perform a statistically significant spectral analysis of each regional spectrum, we set each individual region to contain at least 5000 counts in the 0.3-8 keV band. Our

adaptive mesh results in 2147 regions (Fig. 1a). The sizes of the regions range from $\sim 2'' \times 4''$ for regions enclosing the bright filaments, to $\sim 30'' \times 50''$ for regions representing the faint outer boundary of the SNR. The average angular area of the regions is $\sim$115 arcsec^2.

To estimate mean elemental abundances in the shocked CSM in G292, we extracted X-ray spectra from several representative CSM emission regions identified in previous works (e.g., Lee et al. 2010; the spectrally-soft red diffuse regions near the outermost boundary of the SNR in Fig. 1b). We fitted these regional spectra using the absorbed non-equilibrium ionization (NEI) plane-parallel shock model (Borkowski et al. 2001) with varied abundances (*vpshock*, NEI version 3.0 with updated ATOMDB in XSPEC and ISIS software, Houck & Denicola 2000; Smith et al. 2001; Badenes et al. 2006; Foster et al. 2012). We varied the foreground column (N_H), normalization, electron temperature (kT, where k is the Boltzmann constant and T is the temperature), ionization timescale ($n_e t$, where n_e is the postshock electron number density and t is the time elapsed since the passage of the shock), and elemental abundances for O, Ne, Mg, Si, S and Fe. We fixed the abundances of all other elements to solar values (Anders & Grevesse 1989). The measured abundances and thermodynamic parameters did not show significant variation among the regions (within statistical uncertainties), therefore we took the average values to represent the CSM emission. These average values are consistent with previous estimates (Lee et al. 2010) and are listed in Table 2.

3.4.2 Origin of the Regional Emission (Ejecta vs. CSM)

To characterize the emission across the remnant, we extracted source emission spectra from all 2147 regions. We subtracted the background emission using spectra extracted from source-free regions outside the remnant. We fit spectra for all the

individual regions with an NEI plane shock model. For regions projected within or near the PWN, the contribution in the observed regional spectrum from the nonthermal synchrotron radiation from the PWN may be significant. Therefore, we added a power-law component in our spectral model fits for ∼310 regional spectra generally projected against the spectrally-hard central PWN feature (Fig. 1c) (Hughes et al. 2001; Park et al. 2007). For our spectral model fits, the parameters we varied are: N_H, normalization, kT, $n_e t$ and the abundances for O, Ne, Mg, Si, S and Fe. We fixed the abundances of all other elements to solar values (Anders & Grevesse 1989).

We classified regions as *ejecta-dominated* if the measured abundance for any fitted elemental abundance exceeded our measured CSM abundance values (listed in Table 2) by more than a 3σ confidence level. Using this method, we identify ∼1400 *ejecta-dominated* regions (white regions in Fig. 1c), and ∼700 *CSM-dominated* regions (brown regions in Fig. 1c). In the central regions of the SNR, ∼150 *CSM-dominated* regions and ∼160 *ejecta-dominated* regions are affected by synchrotron continuum emission from the PWN (Fig. 1c). These regions show a relatively high continuum flux in the 2-7 keV band (∼ 10%–60% of the total flux). They yielded fits with $\chi^2/\nu > 2$ and/or unrealistically high electron temperature ($kT \sim$ 3–10 keV) when no power-law component was included in the spectral model. After we added the power-law component, these PWN regions yielded improved fits with $\chi^2/\nu \sim 0.9$ to 1.5, and $kT \lesssim 0.7$ keV. The best-fit photon index is $\Gamma \sim$ 1–3 for these PWN regions, which is generally consistent with values estimated for G292's PWN regions in literature (Gonzalez & Safi-Harb 2003). Overall, our approach yields statistically acceptable fits ($\chi^2/\nu < 2$) for over 99% of the 2147 regions comprising the SNR (Fig. 5a). In Fig. 2, we show an example spectrum of an *ejecta-dominated* region (region "E" in Figs. 1a & 1c), and a *CSM-dominated region* (region "C" in Figs. 1a & 1c). Both these spectra were fitted with an NEI plane shock model assuming our measured

average CSM abundances (Table 2). The *ejecta-dominated* region gives a poor fit to this model ($\chi^2/\nu = 6.6$) due to excessive line fluxes originating form overabundant ejecta gas (primarily from the Ne K and Mg K lines at $E \sim 1.0$ keV and ~1.35 keV respectively). The CSM-dominated region, on the other hand, gives a good fit ($\chi^2/\nu = 1.2$).

3.4.3 Spatial Distribution of the Elemental Abundances and NEI Plasma Parameters

We show the measured abundance distributions of O, Ne, Mg, Si, S and Fe for the entire remnant in Fig. 3. For comparisons, we also show atomic line *equivalent width image* (EWI) maps for these elements in Fig. 3. We created these EWI maps using published methods (e.g., Hwang, Holt and Petre 2000; Park et al. 2002; Schenck et al. 2014). The line and continuum band energies used for making these maps are listed in Table 3. We binned the images by 2×2 pixels, and adaptively smoothed them before performing the EWI calculations. These EWI maps are updated versions of those we had published earlier (Park et al. 2002). Our previous EWI maps were based on ~43 ks of *Chandra* data taken on the ACIS-S3 wherein parts of the remnant were not imaged due to the small field of view of the ACIS-S3. Our new EWI maps provide improved spatial resolution (due to more than an order of magnitude higher count statistics), and they cover the entire SNR. In this work, we also provide EWI maps that have not been published before, namely those for Mg XII, S XV and Fe K (Fe Heα or Fe XXV). In our EWI maps, regions with strongly enhanced EWs are generally coincident with highly overabundant regions in our elemental abundance maps (Fig. 3), indicating that the strong line fluxes are primarily caused by the presence of overabundant ejecta gas.

In Fig. 4, we show abundance-ratio maps (for the *ejecta-dominated* regions) of O/(Si+S+Fe), Ne/(Si+S+Fe), Mg/(Si+S+Fe), Si/(O+Ne+Mg), S/(O+Ne+Mg)

and Fe/(O+Ne+Mg) that highlight the enhancements of lighter O-group elements and the heavier Si, S and Fe relative to each other. Figs. 3i–n and Figs. 4d–f illustrate the anti-alignment between the pulsar and the heavier Si-, S- and Fe-rich ejecta, with the heavier ejecta clearly localized in the north-northwestern regions of the SNR opposite to the projected location of the pulsar (see Section 4.4).

In Fig. 5, we show the spatial distributions of the NEI spectral parameters: N_H, kT, n_et, the *pseudo* electron density (n_{pseudo}), and the *pseudo* thermal pressure (P_{pseudo}). We calculate the pseudo density as $n_{pseudo} = \sqrt{EM/V}$, where EM is the volume emission measure and V is the emission volume (described in Section 4.2). We calculate the pseudo thermal pressure as $P_{pseudo} = n_{pseudo}kT$.

We constructed radial profiles for kT, n_et, and the abundances of O, Ne, Mg, Si, S and Fe along the NW and SE directions. Our intent is to reveal the detailed radial structure in the ionization state and ejecta elemental abundances of the shocked gas. For effectively studying such radial structures, we select the NW sector of the SNR, where the layering structure of abundances and the progressively ionizing ejecta features along the radial distance from the SNR center have been suggested (Park et al. 2002). For comparisons, we also perform a similar study in the opposite area of the SNR (the SE region). This "axis" along NW-SE is also intriguing in light of its alignment with the projected pulsar kick direction (Figs. 3, 4, Section 4.4). For these radial profiles, we divided the ejecta regions into radial intervals of $\sim$15″. We show these regions in Fig. 6a, and the radial profiles in Figs. 6b–i.

3.4.4 Fe-Rich Emission Regions

We note that the Fe-abundances (Fig. 3k) were measured primarily based on the Fe L-line complex ($E \sim$ 0.7-1.2 keV), since the Fe K-shell line (at $E \sim$ 6.6 keV) is weak or undetectable in most individual regional spectra. We fitted the

spectra extracted from Fe-rich regions, with a plane-parallel shock model, with the Fe-abundance fixed at our measured average CSM value (0.13× solar, Table 2), while varying the abundances of O, Ne, Mg, Si, S, Ar and Ca. The abundance of Ni is tied to Fe. We varied the N_H, normalization, kT and $n_e t$. These model fits result in strong residuals at $E \sim 1.2$ keV, consistent with excess emission from the Fe L complex (e.g., Vink 2012; Kamitsukasa et al. 2014 and references therein). We show an example spectrum with model fits for such a region (Region A in Fig. 7) in Figs. 8a & b. For comparisons, we show an example spectrum of an ejecta region with low Fe abundance, which shows no significant residuals off of the best-fit model at $E \sim$ 1.2 keV (Region B in Fig. 7) in Figs. 8c & d.

The Fe-enhancements are supported by our detection of Fe K-shell line in the integrated spectrum of larger areas over the Fe-enhanced regions with significantly higher photon statistics ($\sim 10^6$ counts). We show these large regions in Fig. 7 (regions 1 and 2) and their spectrum in Fig. 9a. For comparisons, the spectrum of an "Fe-poor" region, (region 3 in Fig. 7, containing $\sim 1.7 \times 10^6$ counts in the 0.3-8 keV band) shows significantly weaker Fe K-shell line emission (Fig. 9b). We estimate a 6σ confidence level detection of the Fe K-shell line in the Fe-rich region, while in the Fe-poor region's spectrum this line is detected at a marginal 3σ confidence level.

We measured the line center energy for the observed Fe K-shell line in G292 by Gaussian-fitting of the spectrum extracted from combining ∼30 Fe-overabundant northern regions. We varied the line center energy, line width and normalization in the Gaussian model. We measure a line center energy of 6.62 ±0.08 keV (90% confidence range) for the Fe K-shell emission line (Fig. 10). Our measured Fe K-shell line center energy agrees with earlier *Suzaku* measurements (Kamitsukasa et al. 2014; Yamaguchi et al. 2014), and is consistent with the detected values for other CCSNRs (Yamaguchi et al. 2014).

3.5 DISCUSSION

3.5.1 Spatial Structure of Ejecta Elements and NEI Plasma Parameters

The ejecta in G292 show striking differences between the spatial distributions of O, Ne and Mg (representing hydrostatic nucleosynthesis products), and Si, S and Fe (tracers for explosive nucleosynthesis, especially Fe). While O-, Ne-, and Mg-rich ejecta are widely scattered across the remnant, they appear to be particularly enhanced in the NW and SE quadrants (Figs. 3a–c). This preferred distribution is brought out in our O/(Si+S+Fe), Ne/(Si+S+Fe) and Mg/(Si+S+Fe) ratio maps (Figs 4a–c). In contrast to the abundances of the O-group elements, the abundances of the heavier elements, Si, S and Fe, are enhanced almost exclusively in the NW regions (Figs. 3i–n). This enhancement is also revealed in our Si/(O+Ne+Mg), S/(O+Ne+Mg) and Fe/(O+Ne+Mg) abundance ratio maps (Figs. 4d–f).

X-ray line emission for O, Ne, Mg, Si, S and Fe, shown in our line EW maps, reveal distributions that are generally consistent with our abundance maps (Fig. 3). A similarity between the spatial distribution patterns for the line EWs for O, Ne IX and Mg XI is observed (Figs. 3d–f). These line EWs are generally enhanced close to the projected position of the RS.[1] In the SE, the line EWs for O, Ne IX and Mg XI are enhanced in an area that is coincident with the optical "spur" (Ghavamian et al. 2005; Winkler and Long 2006; Winkler et al. 2009), and they are also generally coincident with our estimated RS position there. On the other hand, line emission for Ne X and Mg XII is not evident in the SE, and it peaks at larger radial distances in other

[1]The projected position of the RS at $r_{RS} \sim 130''$ and CD at $r_{CD} \sim 220''$ are 1D approximations, estimated based on G292's kinematic structure in X-rays (Bhalerao et al. 2015). r is the angular radius measured from the optical expansion center of the remnant at RA (2000.) = 11^h, 24^m, $34^s.4$, and decl. (2000.) = -59°, $15'$, $51''$(Winkler et al. 2009). The actual 3D positions of the RS and CD could differ in different parts of the remnant.

parts of the remnant, closer to the contact discontinuity (CD) and even extending to the outer boundary in some areas (Figs. 3g & 3h). This radially "layered" emission pattern is particularly emphasized in the NW. These high EW-regions in the NW are spatially coincident (in projection) with overabundant ejecta gas (Fig. 3). A similarly layered EW distribution for Ne IX and Ne X lines in the NW regions of G292 have been reported in previous work (Park et al. 2002). Based on our extensive spectral analysis, we show radially decreasing ionization timescale values for the shocked ejecta gas (from the CD to the RS) in the NW (Fig. 6c). This radial distribution of the ionization timescale supports the suggested progressive ionization of the ejecta gas by the RS on its migration towards the center of the remnant. A similar progressive ionization structure for O- and Ne-rich ejecta gas was observed in the young (age $\sim$ 1000 yr) O-rich SNR 1E 0102.2–7219 (Gaetz et al. 2000; Flanagan et al. 2004; Alan et al. 2018). The weak EWs for the highly-ionized Ne X and Mg XII in the SE (Figs. 3g & 3h) are consistent with the generally lower values of the ionization timescale there ($n_e t \sim 5{\times}10^{11}$ cm^{-3} s) compared to those in the NW ($n_e t \sim 10^{12}$ cm^{-3} s). Regions in the NW located just within our identified CD show the highest $n_e t$. These high $n_e t$ regions are followed by regions where $n_e t$ decreases radially inwards towards the RS (Figs. 5d & 6c).

In our radial profiles, O, Ne and Mg peak closer to the CD at about an angular distance of 170″-200″ from the center of the SNR. On the other hand, Si, S and Fe abundances peak at a smaller radial distance of about 130″-150″ from the SNR's center (Figs. 6d–6i). This provides further evidence for a layered ejecta-structure in the NW, where the classical "onion-shell" nucleosynthesis-configuration at the core of the massive progenitor appears to have been preserved in the SNR. However, this layering of the ejecta elements is not clearly evident in other directions. For example, abundances for O and Fe peak at about the same radial distance ($r \sim 130''$) in the

SE (blue curves in Figs. 6d–i). This may suggest some mixing of the ejecta in the SE and/or projection effects caused by O-rich regions that are physically located at larger radial distances than the Fe-rich regions, but are projected closer to the SNR center along the line of sight.

Our electron temperature map shows a general range between 0.5 to 1 keV across the remnant (Fig. 5c), but there are regions in the N and NW with significantly higher electron temperature ($kT \sim$ 2-4 keV). These high-temperature regions are also enriched in Fe (Fig. 3k). The detection of Si, S and Fe (especially the Fe K line) in this region may be due to its hot gas temperature. The higher electron temperatures in the N and NW are generally consistent with the results reported by Park et al. 2007.

The absorbing column (N_H) does not show significant variations across the remnant (Fig. 5b). There are a few regions in the S and SW (near the outermost boundary of the SNR) with higher N_H ($\sim 8 \times 10^{21}$ cm^{-2}). Although the higher N_H in the S and SW is not statistically significant, an excess N_H in this part of the SNR cannot be ruled out. This is suggested by the enhanced dust emission observed from these regions in the far-infrared (e.g., Park et al. 2007; Ghavamian & Williams 2016). There may be superposed H II regions in the SW (as suggested by Rodgers et al. 1960), or a molecular cloud complex projected along and outside the southwestern boundary of G292 (as suggested by Ghavamian & Williams 2016). Detailed maps and distances to these molecular cloud structures are not known, and the presence of a higher column in the S and SW will need further investigation.

3.5.2 Ejecta Mass

We estimated the ejecta masses for the elements based on our estimated volume emission measure (e.g., Lopez et al. 2009 and references therein):

$$EM_x = n_e n_i V f \tag{3.1}$$

where n_i is the ion number density, V is the volume of the region, f is the filling factor which characterizes the clumpiness of the emission, and the subscript x designates the element or ion being evaluated. To estimate V we assume a distance of $d = 6$ kpc to the SNR. We assume that the ejecta knots and filaments represent localized volumes of X-ray-emitting gas, for which the line of sight depth is of the order of the angular extent of each rectangular region.

We calculate the electron number density:

$$n_e = \sqrt{\frac{EM_x B_x X_x N_x}{V}} \tag{3.2}$$

where B_x is the best-fit abundance, X_x is the solar number abundance and N_x is the average number of electrons lost by a given ion. We estimate N_x using a simple approximation for O-rich SNR gas (Lazendic et al. 2006):

$$N_x = \begin{cases} Z, & \text{for } Z \leq 9 \\ Z - 2, & \text{for } 10 \leq Z \leq 16 \\ Z - 10, & \text{for } Z \geq 17 \end{cases} \tag{3.3}$$

where Z is the atomic number of the element. Using this approximation we get the following N_x: O = 8, Ne = 8, Mg = 10, Si = 12, S = 14, Fe = 16. To calculate N_x for Fe, we assume that the Fe XVII ion is the dominant contributor to the Fe L complex detected at $E \sim$ 0.7-1.2 keV in G292 (e.g., Kamitsukasa et al. 2014, and this work). We note that assuming the higher ionized state of Fe XXV ($N_x = 24$),

corresponding to the observed Fe K-shell line emission at $E = 6.6$ keV (e.g., Vink 2012 and references therein, Vink 2017), does not significantly alter our estimated Fe ejecta masses.

We calculate the mass of the element in each ejecta region:

$$M_x = n_i A_x m_u V f \tag{3.4}$$

where, $n_i = n_e/N_x$, A_x is the atomic mass for the dominant isotope and m_u is the atomic mass unit in grams (1 amu = 1.66×10^{-24} g).

We calculate the total ejecta mass for each element by summing the calculated masses for all ejecta regions. We list our calculated ejecta masses for O, Ne, Mg, Si, S, Fe for the entire remnant, and the total ejecta mass in Table 4. We estimate a total shocked ejecta mass of $\sim 1.29^{+0.49}_{-0.28}\ f^{1/2}\ d_6^{3/2}$ M$_\odot$. In Fig. 11 we show the "quadrants" and "hemispheres" we use to investigate asymmetries in the ejecta elemental distributions. We list the calculated ejecta masses for these quadrants and hemispheres in Table 4.

We estimate that a total of $\sim 0.03 \pm 0.01\ f^{1/2}\ d_6^{3/2}$ M$_\odot$ of Fe ejecta has been shocked by the RS to emit X-rays. This is significantly less than the Fe-yield of ∼0.07-0.1 M$_\odot$ predicted for a wide range of progenitors (M = 13–40 M$_\odot$), metallicity (Z = 0–0.02) and explosion energy (E = 1–30 $\times 10^{51}$ ergs)(Nomoto et al. 2006). Similarly, we estimate that $\sim 0.06 \pm 0.01\ f^{1/2}\ d_6^{3/2}$ M$_\odot$ of Si ejecta, and $\sim 0.02 \pm 0.01\ f^{1/2}\ d_6^{3/2}$ M$_\odot$ of S ejecta have been shocked the RS (Table 4). Thus, ∼10-80% of Si, and ∼30-80% of S ejecta may still remain unshocked in the SNR (based on yields predicted for progenitors with mass 13–40 M$_\odot$, $Z = 0.02$ and $E = 1 \times 10^{51}$ ergs, Nomoto et al. 2006, also see Section 4.5). This suggests that only the outskirts of the central ejecta gas may have been shocked by the RS. This scenario is supported by the undistorted morphology of the PWN, an indication that the RS may have just reached the central

regions of the SNR where the Si-, S- and Fe-rich ejecta are expanding (Gaensler & Wallace 2003; Gaensler & Slane 2006; Bhalerao et al. 2015).

3.5.3 Properties of the CSM

We identify the *CSM-dominated* regions in G292 based on their low abundances estimated by our regional spectral model fits. Our *CSM-dominated* regions in Fig. 1c trace the various CSM features identified in earlier works (see Section 1). These include the thin circumferential filaments and the spectrally soft diffuse emission at the outer boundary. The origin of the thin circumferential filaments is unclear. They may be the result of the blast wave interacting with stellar wind structures produced during late evolutionary stages of the G292 progenitor (e.g. RSG and blue supergiant phases, Park et al. 2002). The spectrally soft diffuse emission at the outer boundary generally conforms to our estimated CD location, marking the boundary between the CSM and ejecta (Fig. 1c). It also may be projected over the face of the entire SNR, "filling in" the regions between the spectrally-hard ejecta filaments.

A prominent CSM feature is the central equatorial "belt" (Park et al. 2002, 2004; Ghavamian et al. 2005). Based on their multiband infrared *AKARI* observations, Lee et al. (2009) proposed that this feature is actually a ring-like structure that in projection presents as two long filaments, a northern filament and a southern filament, that run east-west in the central regions of the SNR (Fig. 1d). Only the bright southern filaments of this structure were previously identified in X-rays (Park et al. 2002). In Fig. 1c we show that the regions corresponding to the northern filament of the equatorial ring (ER), in addition to those for its southern filaments are generally coincident with our identified *CSM-dominated* regions. These filaments appear to connect into a closed loop on the eastern side, but are more fragmented on the western side (Figs. 1b–d, 5e & f).

The ER is composed of dense gas, and both the northern and southern filaments clearly stand out in our n_{pseudo} and P_{pseudo} maps (Figs. 5e & 5f). This ring-like structure may have originated from pre-SN mass loss at the equator of the rotating progenitor and/or from interactions in a binary system (e.g., Collins et al. 1999; Chevalier 2000; Morris & Podsiadlowski 2009; Langer 2012). The northern filament of the ER is about 2-3 times fainter than the southern filament. This may be consistent with the northern filament being located at the far side of the remnant, while the southern filament is located at the near side, with the distance between them similar to the diameter of the SNR ($\sim$15 pc, Lee et al. 2010). This is based on assuming a circular geometry for the ER. Absorption and scattering of emission from the northern filament by material within the SNR may account for its fainter appearance. Based on the ratio of the ring's N-S angular separation ($\sim$75″) to its E-W diameter ($\sim$295″), we estimate that the normal to the ring is inclined to the plane of the sky by an angle of $\alpha \sim 15° \pm 5°$. If the ER was shed by the progenitor's equatorial winds before the SN explosion, then this inclination angle would correspond to the inclination angle of the progenitor's rotation axis. This is consistent with the N-S alignment of the spin axis of the embedded pulsar (J1124–5916) inferred from the observed N-S orientation of its jet (Park et al. 2007). The rotation axis of the progenitor appears to have been preserved in the neutron star after the SN explosion.

We estimate the CSM mass in G292, by assuming a fully ionized plasma with 10% He, giving the relationship $n_e = 1.2 n_H$. To estimate the volumes of the ER regions we assume the ER has a ring-like geometry with a line of sight depth similar to its N-S angular thickness ($\sim$15″). Based on this geometry we estimate the total volume of the ER $\sim 8 \times 10^{54}\ f\ d_6$ cm^3. To estimate the volume of the outer spherical CSM, we assume it has a shell-like structure with a line of sight depth similar to its angular thickness ($\sim$45″). We calculate the total CSM mass by summing the

masses for all ∼700 CSM regions. We list our estimates for the CSM mass in Table 5. We estimate a shocked CSM mass of $\sim 9.98^{+2.72}_{-1.00}\ f^{1/2}\ d_6^{3/2}\ M_\odot$. This is close to the lower bound of the previous estimates based on the radial density profile of the progenitor star's RSG winds (∼15–40 $M_\odot$, Lee et al. 2010). The ER comprises ∼16% of the total estimated shocked CSM mass (Table 5). This may suggest that a significant pre-SN mass loss occurred through the progenitor's equatorial winds. The ER is reminiscent of similar ring-like circumstellar features observed, in SN 1987A (e.g., Frank et al. 2016 and references therein) and the B-type supergiant SBW1 (Smith et al. 2013). Such structures may originate from mass loss facilitated by the rapid rotation of the progenitor, binary interactions, confinement of the shed mass by magnetic fields, and possible combinations of these factors (e.g., Kurfurst et al. 2018 and references therein).

We estimate an average thermal pressure of $\sim 5\times10^{-9}$ ergs cm^{-3} for the CSM at the outer boundary of the remnant. This is comparable to the estimated ram pressure of the PWN ($2.6\times10^{-9}\ d_6^{-2}$ ergs cm^{-3}, Hughes et al. 2003). This may support the interaction between the RS and PWN as suggested by Bhalerao et al. (2015). An early-stage RS-PWN interaction scenario has also been suggested by Gaensler & Wallace (2003), based on the close juxtaposition between the PWN and the overlying shell in radio and X-rays. We note that previously it had been suggested that the RS may not have reached the PWN (Park et al. 2004). This was based on the estimation of a large pressure difference between the ER and the PWN. Our pseudo thermal pressure map (Fig. 5f), shows a range of about two orders of magnitude over the SNR. Thus the high pressure difference estimated by Park et al. (2004) may have been due to the selection of a high-pressure region on the ER (Region 1 in Park et al. 2004), rather than a region with typical gas pressure generally found between the FS and RS.

3.5.4 Ejecta Asymmetry in the Remnant

CCSN explosions involve a complex interaction of several physical processes, the details of which are not fully understood (e.g., Janka et al. 2012; Burrows 2013; Couch 2017). Observations indicate that a property common to many CCSNe is explosion asymmetry (e.g., Wang et al. 2001, 2003; Leonard et al. 2006; Wang & Wheeler 2008; Lopez et al. 2011; Vink 2012; Lopez & Fesen 2018 and references therein). Recent theoretical studies have suggested that asymmetries in CCSNe can originate from hydrodynamic instabilities during the SN explosion (Janka 2017 and references therein). These studies show that the bulk of intermediate mass elements (Si, S, Ar, Ca and Ti) and the heavier iron-group elements (Cr, Fe, Ni) are ejected opposite to the direction in which the NS is kicked. A direct correlation is also found between NS-kick velocities and ejecta asymmetries (Wongwathanarat et al. 2013, 2017).

This anti-alignment or "antipodal" asymmetry between NSs' and the ejecta has been observed in several CCSNRs. Analysis of *Chandra* and *ROSAT* data with the power-ratio method showed evidence for such an asymmetry in five CCSNRs: G292, CTB 109, Cas A, PKS 1209–51 and Puppis A (Holland-Ashford et al. 2017). However, in the study by Holland-Ashford et al. (2017), X-ray emission was examined in the 0.5–2.1 keV energy range (thus contributions from the heavier elements such as S and Fe were not included), and a separation between emission originating from ejecta-rich regions as opposed to that from the CSM was not made. Katsuda et al. (2018a) applied an image-decomposition method to *Chandra* and *XMM-Newton* data to find that the elements Si, S, Ar and Ca were predominantly ejected opposite to the direction of NS motion in six CCSNRs: G292, Cas A, Puppis A, Kes 73, RCW 103, and N49. High-energy X-ray studies of Cas A using *NuSTAR* revealed that ^{44}Ti, which is made by explosive nucleosynthesis from Si in the inner regions of the

exploding star, is distributed opposite to the direction of the NS-motion (Grefenstette et al. 2014). ^{44}Ti asymmetry in the form of redshifted ^{44}Ti emission lines was also detected in SN 1987A, suggesting that its yet-undetected compact remnant may have been kicked towards the front of the remnant (Boggs et al. 2015; Wongwathanarat et al. 2017).

To investigate the ejecta spatial asymmetry in G292, we divided the ejecta regions into quadrants and hemispheres (Fig. 11). These divisions were made with reference to the optical expansion center of the SNR (RA (2000.) = 11^h, 24^m, $34^s.4$ and decl. (2000.) = -59°, 15′, 51″, Winkler et al. 2009), and the presumed direction of the pulsar's kick to the SE (Park et al. 2007; Winkler et al. 2009). We list the ejecta masses estimated for the quadrants and hemispheres in Table 4, and we show their fractional mass distributions in Figs. 12 & 13. We list the average abundances for the ejecta regions in the entire remnant, as well as for the ejecta regions in the quadrants and the hemispheres in Table 6.

The estimated ejecta masses of Si, S and Fe are significantly higher in the NW than in the SE. The NW hemisphere accounts for ∼90% of the total Si-ejecta mass, ∼100% of the total S-ejecta mass, and ∼60% of the total Fe-ejecta mass (Table 4, Fig. 12). This non-uniform ejecta distribution may originate from an asymmetric RS-structure, where the RS may not have migrated deep-enough in the SE to heat the heavier Si-, S- and Fe-rich ejecta. However, in the SE, the abundances of O, Ne, Mg, Fe and the ionization timescale are generally enhanced between ∼120″ and ∼170″ from the SNR center. Thus in the SE, the RS may be located at ∼120″ from the SNR center, which is similar to that in other parts of the remnant. While Fe is enhanced in the NW regions of the SNR, the overall projected distribution of the Fe-rich ejecta detection over the SNR appears to be nearly circular in shape, generally coincident with the circular outline of the RS (Fig. 3k). Thus, we propose that the

apparent "lack' of heavy elements in the SE regions of G292 is probably caused by an intrinsically asymmetric distribution of Si-, S- and Fe-rich ejecta gas rather than by a significantly asymmetric RS structure.

Most of the Si, S and Fe ejecta are enhanced in regions opposite to the currently projected position of the pulsar (PSR J1124-5916, Figs. 1b & 3). The pulsar is displaced $\sim$46$''$ from the presumed SN explosion center (RA (2000.) = 11^h, 24^m, $34^s.4$ and decl. (2000.) = -59°, 15$'$, 51$''$, Winkler et al. 2009). This displacement corresponds to an average transverse velocity of $\sim$440 km s^{-1} at d = 6 kpc and age $\sim$ 3000 yr (Hughes et al. 2001, 2003; Winkler et al. 2009). This suggested motion of the pulsar is likely the result of a "kick" to the newly-formed NS during the SN explosion (Lai 2001; Park et al. 2007; Winkler et al. 2009). Recent 2D and 3D numerical simulations demonstrate that significant NS-kicks in the range of a few hundred to $\sim$1000 km s^{-1} can be produced by asymmetric SN explosions in which the bulk of intermediate and iron-group elements (e.g., Si and Fe) are ejected in the opposite direction to the NS-kick (e.g., Wongwathanarat et al. 2013, 2017; Janka 2017 and references therein). Consequently, the NS and the bulk of the inner ejecta (the explosive nucleosynthesis products) would migrate into opposite directions of each other in the resulting SNR. The kick imparted to the NS mainly originates from gravitational and hydrodynamic forces exerted by the asymmetric ejecta on the NS, and from momentum conservation. Anisotropic neutrino emission plays only a minor role (Scheck et al. 2006; Wongwathanarat et al. 2013; Janka 2017). The NS is accelerated by the gravitational forces exerted by the slower, denser ejecta found in the hemisphere opposite to the stronger explosion. The acceleration of the NS can last several seconds, so that while the NS is pulled into one hemisphere, explosive nucleosynthesis of Fe-group elements proliferates in the opposite hemisphere (Scheck

et al. 2006; Nordhaus et al. 2010, 2012; Wongwathanarat et al. 2013, 2017; Janka 2017).

In this study, we provide the first observational evidence that the bulk of Fe was ejected opposite to the NS's kick (e.g., Figs. 3k, 3n, 4f, 9a & 12). This spatial distribution of the Fe-rich ejecta is in close agreement with 3D simulations which predict that ^{56}Ni, the parent-isotope of ^{56}Fe, is mainly formed and ejected opposite to the NS's kick vector (Wongwathanarat et al. 2013, 2017). Along with Fe, we also show that the bulk of Si and S was ejected opposite to the NS's kick (e.g., Figs. 3, 4 & 12).

Our results suggest an explosion axis generally oriented NW-SE. We find that the X-ray-emitting O-, Ne- and Mg-rich ejecta are generally enhanced along NW-SE direction (Fig. 3). To test the explosion kinematics projected across the plane of the sky (as suggested by this ejecta mass distribution), we estimate the O-, Ne- and Mg-rich ejecta mass along the main shell of the SNR (regions between our estimated RS and CD, Fig. 13). We excluded regions projected within the RS for this comparison, since these ejecta may have their main kinematics along the line of sight. The combined NW+SE shell-regions account for a significantly higher fraction of the ejecta mass for O, Ne and Mg ($\sim$60%–65%, Fig. 13 and Table 7).

3.5.5 Progenitor Mass

To estimate the G292 progenitor mass, we compared the elemental abundance ratios for ejecta regions from the entire SNR to those predicted by CCSN nucleosynthesis models (Woosely & Weaver 1995). In Fig. 14 we show those modeled values of elemental abundance ratios for which the progenitor masses are relatively well-discriminated. We compare these modeled ratios to the our estimated mean

abundance ratios for G292. From these comparisons, we place an upper limit to the G292 progenitor mass of $\lesssim$ 30 $M_{\odot}$.

From our measured Si/Fe ratio for the *ejecta-dominated* regions in G292, we obtain a progenitor mass estimate of ∼13–15 $M_{\odot}$ (Fig. 14b). Our measured O/Fe ratio for the *ejecta-dominated* regions in G292 corresponds to a progenitor mass of ∼15-25 $M_{\odot}$ (Fig. 14a). These two ratios suggest a lower limit to the G292 progenitor mass of $\gtrsim$ 13 $M_{\odot}$. Recently, Katsuda et al. (2018b) propose that both of these ratios (Fe/O and Fe/Si) are more reliable indicators of the CCSN progenitor mass than the traditionally used abundance ratios of the other alpha elements to Si (e.g., O/Si, Ne/Si, Mg/Si, and S/Si). This is based on their comparisons of the progenitor mass-distributions of 41 CCSNRs in the Milky Way and the Large and Small Magellanic Clouds, to the standard Salpeter initial mass function. Based on G292's Fe/Si ratio measured previously with *Suzaku* data (Kamitsukasa et al. 2014), they estimated a progenitor mass of $\lesssim$15 $M_{\odot}$. Our estimated lower limit is consistent with this estimate by Katsuda et al. (2018b). Thus, our abundance ratios suggest a progenitor mass in the range of 13 $M_{\odot} \lesssim M \lesssim$ 30 $M_{\odot}$ (Fig. 14).

If we combine our calculated mass for the shocked ejecta ($\sim 1.29^{+0.49}_{-0.28}\ f^{1/2}\ d_6^{3/2}$ $M_{\odot}$, Table 4), the shocked CSM ($\sim 9.98^{+2.72}_{-1.00}\ f^{1/2}\ d_6^{3/2}$ $M_{\odot}$, Table 5) with a typical neutron star mass of ∼1.4 $M_{\odot}$ and a dust mass of ∼0.023 $M_{\odot}$ estimated for G292 (Ghavamian & Williams 2016), we obtain total mass of $\sim 13.0^{+3.2}_{-1.3}$ $M_{\odot}$. This mass is close to the lower bound of our estimated progenitor mass range based on the ejecta elemental abundance ratios. The progenitor mass would be higher than this calculated value depending on the mass of the unshocked ejecta, and the unshocked CSM mass lost prior to the explosion through stellar winds and binary interactions. It is not clear if the bulk of the O, Ne and Mg ejecta have already been shocked in G292. Turbulence and mixing may have retained ejecta for these lighter elements

close to the center of the explosion. There could also be reserves of unshocked Si-, S- and Fe-rich ejecta close to the SNR's center (see Section 4.2). We estimate that there could be the following amounts of unshocked ejecta in G292: O $\lesssim$ 2.8 $M_\odot$, Ne $\lesssim$ 0.4 $M_\odot$, Mg $\lesssim$ 0.15 $M_\odot$, Si $\lesssim$ 0.2 $M_\odot$, S $\lesssim$ 0.1 $M_\odot$, and Fe $\lesssim$ 0.07 $M_\odot$ (based on yields calculated for progenitors with mass 13–30 $M_\odot$, $Z = 0.02$ and $E = 1{\times}10^{51}$ ergs, Nomoto et al. 2006). Thus there could be $\lesssim$ 4 $M_\odot$ of ejecta that have not yet been shocked by the RS in G292.

We compared our measured elemental ejecta-mass yields to those predicted for CCSN nucleosynthesis models (Fig. 15, Nomoto et al. 2006, for $Z = 0.02$ and $E = 1{\times}10^{51}$ ergs). Since our estimated total ejecta mass is only the shocked component (and thus represents a lower limit of the total ejecta mass), this comparison allows us to rule out progenitor masses with elemental ejecta yields less than our estimated values. The yields of O, Ne and Mg suggest a progenitor with a mass $\gtrsim$ 20 $M_\odot$, and with a lower limit of $\gtrsim$ 15 $M_\odot$ (Fig. 15). We note that predicted yields are model-dependent, and are sensitive to several parameters such as metallicity and rotation rate of the progenitor, and specifics of the explosion (e.g., Hirschi 2017; Fryer et al. 2018).

Theoretical calculations generally favor the production of a black hole rather than a NS for a progenitor of mass $\gtrsim$ 25 $M_\odot$ (e.g., Woosely et al. 2002). Exceptions to this "traditional" limit may exist; for example, recent CCSN explosion models indicate that black holes can result from progenitor explosions of M $\gtrsim$ 15 $M_\odot$, and NSs can form from progenitors as massive as 120 $M_\odot$ (Sukhbold et al. 2016). Various factors such as the progenitor's metallicity, the presence of stellar companions, rotation rate of the progenitor, explosion energy and nucleosynthesis history can affect the outcome of the explosion. For example, a significant mass loss by a massive progenitor (with M $\gtrsim$ 25 $M_\odot$) to its companion in a binary system, may lead to the formation of a NS

rather than a black hole (e.g., Belczynski & Taam 2008 and references therein). The presence of the ER in G292 suggests that its progenitor star may have been part of a binary and/or rapidly rotating (see Section 4.3). Thus if the G292 progenitor was more massive than ∼20–25 $M_{\odot}$, the formation of the observed pulsar rather than a black hole may be the result of significant mass loss of the progenitor star due to its binary interaction prior to the SN explosion. Based on the results from our elemental abundance ratios and ejecta yield estimates, we propose a conservative estimate of 13 $M_{\odot} \lesssim M \lesssim 30\ M_{\odot}$ for the G292 progenitor mass.

3.6 SUMMARY & CONCLUSIONS

Based on our deep *Chandra data*, we study the detailed structure of the shocked ejecta and CSM gas in the textbook-type supernova remnant G292.0+1.8. Our results are based on the systematic spectral analysis of over ∼2000 regions covering the entire remnant. We identify the spatial distribution of Fe-rich ejecta in G292 for the first time, based on our detection of enhanced Fe L and Fe K-shell line emission. We provide spatial distribution maps for O-, Ne-, Mg- Si-, S- and Fe-rich ejecta. For the first time we identify the X-ray counterparts of the entire equatorial ring-like dense CSM, whose components had previously been detected in infrared. Based on elemental abundance ratios, and estimates of the ejecta and CSM masses, we estimate the G292 progenitor star's main sequence mass of 13–30 $M_{\odot}$. Our ejecta maps reveal a preferred NW-SE distribution axis for the elements O, Ne, Mg, Si, S and Fe. Furthermore, Si-, S- and Fe-rich ejecta are primarily found in the northwestern hemisphere. This provides the first clear observational evidence that the inner ejecta in G292, consisting of key explosive nucleosynthesis products such as Fe, were predominantly expelled opposite to the direction of the neutron star's kick during the SN explosion. This anti-alignment between the neutron star and the heavier inner ejecta is con-

sistent with theoretical CCSN calculations in which the neutron star-kick originates from gravitational and hydrodynamic forces exerted by the asymmetric ejecta on the NS, and from momentum conservation.

Acknowledgments

This work was supported in part by the SAO through *Chandra* grant GO1-12077X. JB acknowledges support from the NASA Texas Space Grant Consortium. We thank Dr. Daniel Dewey, and Dr. Thomas G. Pannuti for valuable discussions. We also thank the MIT *Chandra* HETG group for useful ISIS scripts and plotting routines.

REFERENCES

[Anders & Grevesse (1989)] Anders, E. & Grevesse, N. 1989, Geochim. Cosmochim. Acta, 53, 197

[Alan (2018)] Alan, N., Park, S. & Bilir, S. 2018, ApJ, Submitted

[Badenes (2006)] Badenes, C., Borkowski, K. J., Hughes, J. P., Hwang, U., & Bravo, E. 2006, ApJ, 645, 1373

[Belczynski & Taam (2008)] Belczynski, K. & Taam, R. E. 2008, ApJ, 685, 400

[Bhalerao et. al. (2015)] Bhalerao, J., Park, S., Dewey, D. et al. 2015, ApJ, 800, 65

[Boggs (2015)] Boggs, S. E., Harrison, F. A., Miyasaka, H. et al. 2015, Science, 348, 670

[Borkowski et al.(2001)] Borkowski, K. J., Lyerly, W. J., & Reynolds, S. P. 2001, ApJ, 548, 820

[Burrows (2013)] Burrows, A. 2013, RvMP, 85, 245

[Camilo et al.(2002)] Camilo, F., Manchester, R. N., Gaensler, B. M., Lorimer, D. R., & Sarkissian, J. 2002, ApJ, 567, L71

[Chevalier (1992)] Chevalier, R. A. 1992, Nature, 355, 691

[Chevalier (2000)] Chevalier, R. A. 2000, ApJ, 538, L151

[Chevalier (2005)] Chevalier, R. A. 2005, ApJ, 619, 839

[Chita et al. (2008)] Chita, S. M., Langer, N., van Marle, A. J. et al. 2008, A & A, 488, L37

[Couch(2017)] Couch, S. M. 2017, RSPTA, 375, 60271

[Collins(1999)] Collins, T. J. B., Frank, A., Bjorkman, J. E. & Livio, M. 1999, ApJ, 512, 322

[Dewey et al. (2007)] Dewey, D., DeLaney, T. and Lazendic, J. S. 2007, RevMexAA, 30, 84

[Flanagan et al. (2004)] Flanagan, K. A., Canizares, C. R., Dewey, D., et al. 2004, ApJ, 605, 230

[Foster et al. (2012)] Foster, A. R., Ji, L., Smith, R. K., & Brickhouse, N. S. 2012, ApJ, 756, 128

[Frank et al. (2016)] Frank, K., Zhekov, S. A., Park, S. et al. 2016, ApJ, 829, 40

[Fryer et al. (2018)] Fryer, C. L., Andrews, S., Wesley, E. et al. 2018, ApJ, 856, 6

[Gaensler & Wallace (2003)] Gaensler, B. M. & Wallace, B. J. 2003, ApJ, 594, 326

[Gaensler & Slane (2006)] Gaensler, B. M. & Slane, P. O. 2006, ARA&A, 44, 17

[Gaetz et al. (2000)] Gaetz, T. J., Butt, Y. M., Edgar, R. J., et al. 2000, ApJ, 534, L47

[Ghavamian et al. (2005)] Ghavamian, P., Hughes, J. P., & Williams, T. B. 2005, ApJ, 635, 365

[Ghavamian et al. (2009)] Ghavamian, P., Raymond, J. C., Blair, W. P., et al. 2009, ApJ, 696, 1307

[Ghavamian et al. (2012)] Ghavamian, P., Long, K. S., Blair, W. P., et al. 2012, ApJ, 750, 39

[Ghavamian & Williams (2016)] Ghavamian, P. & Williams, B. J. 2016, ApJ, 831, 188

[Gonzalez & Safi-Harb (2003)] Gonzalez, M. & Safi-Harb, S. 2003, ApJ, 583, L91

[Goss et al. (1979)] Goss, W. M., Shaver, P. A., Zealey, W. J., et al. 1979, MNRAS, 188, 357

[Gotthelf & Halpern (2009)] Gotthelf, E. V. & Halpern, J. P. 2009, ApJ, 695, L35

[Grefenstette et al. (2014)] Grefenstette, B. W., Harrison, F. A., Boggs, S. E., et al. 2014, Nature, 506, 339

[Hirschi (2017)] Hirschi, R. 2017, in Handbook of Supernovae, ed. A. Alsabti & P. Murdin. (Cham, Switzerland: Springer International Publishing AG), 1879

[Holland-Ashford (2017)] Holland-Ashford, T., Lopez, L., Auchettl, K., et al. 2017, ApJ, 844, 84

[Houck & Denicola (2000)] Houck, J. C. & Denicola, L. A. 2000, in ASP Conf. Ser. 216, Astronomical Data Analysis Software and Systems IX, ed. N. Manset, C. Veillet, & D. Crabtree, (San Francisco, CA:ASP), 591

[Hughes et al. (2001)] Hughes, J. P., Slane, P. O., Burrows, D. N., et al. 2001, ApJ, 559, L153

[Hughes et al. (2003)] Hughes, J. P., Slane, P. O., Park, S., Roming, P. W. A., & Burrows, D. N. 2003, ApJ, 591, L139

[Hwang (2000)] Hwang, U., Holt, S. S. & Petre, R. 2000, ApJ, 537, L119

[Hwang (2008)] Hwang, U., Petre, R. and Flanagan, K. A. 2008, ApJ, 676, 378

[Jakobsen (1991)] Jakobsen, P., Albrecht, R., Barbieri, C. et al. 1991, ApJ, 369, L63

[Janka et al. (2012)] Janka, H.-T., Hanke, F., Hudepohl, L., et al. 2012, PTEP, 2012, aA309J

[Janka (2017)] Janka, H.-T. 2017, ApJ, 837, 84

[Kamitsukasa et al. (2014)] Kamitsukasa, F., Koyama, K., Tsunemi, H., et al. 2014, PASJ, 66, 648

[Katsuda et al. (2008)] Katsuda, S., Mori, K., Tsunemi, H., Park, S., Hwang, U., Burrows, D. N., Hughes, J. P. and Slane, P. O. 2008, ApJ, 678, 297

[Katsuda et al. (2018a)] Katsuda, S., Morii, M., Janka, H.-T., et al. 2018a, ApJ, 856, 18

[Katsuda et al. (2018b)] Katsuda, S., Takiwaki, T., Tominaga, N. et al. 2018b, arXiv:1807.03426, ApJ accepted

[Kurfurst et al. (2018)] Kurfurst, P., Feldmeier, A. & Krticka, J. 2018, A&A, 613, 75

[Lai (2001)] Lai, D. 2001, LNP, 578, 424

[Langer (2012)] Langer, N. 2012, ARA&A, 50, 107

[Lazendic et al. (2006)] Lazendic, J. S., Dewey, D., Schulz, N. S., & Canizares, C. R. 2006, ApJ, 651, 250

[Leonard et al. (2006)] Leonard, D., Filipenko, A. V., Ganeshalingam, M., et al. 2006, Nature, 440, 505

[Lee et al. (2009)] Lee, H.-G., Koo, B.-C., Moon, D.-S., et al. 2009, ApJ, 706, 441

[Lee et al. (2010)] Lee, J.-J., Park, S., Hughes, J. P., et al. 2010, ApJ, 711, 861

[Lopez et al. (2009)] Lopez, L. A., Ramirez-Ruiz, E., Pooley, D. A. & Jeltema, T. E. 2009, ApJ, 691, 875

[Lopez et al. (2011)] Lopez, L. A., Ramirez-Ruiz, E., Huppenkothen, D., et al. 2011, ApJ, 732, 18

[Lopez & Fesen (2018)] Lopez, L. A. & Fesen, R. A. 2018, SSRv, 214, 44

[Luna et al. (2016)] Luna, G. J. M., Smith, M. J. S, Dubner, G., Giacani, E. and Casteletti, G. 2016, A&A, 590, A70

[Maoz & Graur (2017)] Maoz, D. & Graur, O. 2017, ApJ, 848, 25

[Mitsuda et al. (2007)] Mitsuda, K., Bautz, M., Inoue, H. et al. 2007, PASJ, 59, S1

[Morris & Podsiadlowski (2009)] Morris, T. & Podsiadlowski, Ph. 2009, MNRAS, 399, 515

[Nomoto et al. (2006)] Nomoto, K., Tominaga, N., Umeda, H. et al. 2006, NuPhA, 777, 424

[Nordhaus et al. (2010)] Nordhaus, J., Brandt, T. D., Burrows, A., et al. 2010, PhRvD, 82, 103016

[Nordhaus et al. (2012)] Nordhaus, J., Brandt, T. D., Burrows, A., et al. 2012, MNRAS, 423, 1805

[Park et al. (2002)] Park, S., Roming, P. W. A., Hughes, J. P. et al. 2002, ApJ, 564, L39

[Park et al. (2004)] Park, S., Hughes, J. P., Slane, P. O., et al. 2004, ApJ, 602, L33

[Park et al. (2007)] Park, S., Hughes, J. P., Slane, P. O., et al. 2007, ApJ, 670, L121

[Pavlov et al. (2000)] Pavlov, G. G., Zavlin, V. E., Aschenbach, B. et al. 2000, ApJ, 531, L53

[Rodgers et al. (1960)] Rodgers, A. W., Campbell, C. T. & Whiteoak, J. B. 1960, MNRAS, 121, 103

[Scheck (2006)] Scheck, L., Kifondis, K., Janka, H.Th. & Muller, E. 2006, A&A, 457, 963

[Schenck (2014)] Schenck, A., Park, S., Burrows, D. N. et al. 2014, ApJ, 791, 50

[Schenck (2016)] Schenck, A., Park, S. & Post, S. 2016, AJ, 151, 161

[Smith (2001)] Smith, R. K., Brickhouse, N. S., Liedahl, D. A. & Raymond, J. C. 2001, ApJ, 556, L91

[Smith et al. (2013)] Smith, N., Arnett, W. D., Bally, J. et al. 2013, MNRAS, 429, 1324

[Sukhbold (2016)] Sukhbold, R., Ertl, T., Woosley, S. E. et al. 2016, ApJ, 821, 38

[Thielemann (2007)] Thielemann, F. -K., Frohlich, C., Hirschi, R., et al. 2007, PrPNP, 59, 74

[Tuohy et al. (1982)] Tuohy, I. R., Clark, D. H. & Burton, W. M. 1982, ApJ, 260, L65

[Vink et al. (1996)] Vink, J., Kaastra, J. S. and Bleeker, J. A. M. 1996, A&A, 307, L41

[Vink (2008)] Vink, J. 2008, AdSpR, 41, 503

[Vink (2012)] Vink, J. 2012, A&ARv, 20, 49

[Vink (2017)] Vink J. 2017, in Handbook of Supernovae, ed. A. Alsabti & P. Murdin. (Cham, Switzerland: Springer International Publishing AG), 2063

[Wang et al. (2001)] Wang, L., Howell, A., Hoflich, P. et al. 2001, ApJ, 550, 1030

[Wang et al. (2003)] Wang, L., Baade, D., Hoflich, P. & Wheeler, J. C. 2003, 592, 457

[Wang & Wheeler (2008)] Wang, L. & Wheeler, J. C. 2008, ARA&A, 46, 433

[Weisskopf et al. (2005)] Weisskopf, M. C., Aldcroft, T. L., Bautz, M. et al. 2005, CIBu, 162, 5

[Winkler & Long (2006)] Winkler, P. F. & Long, K. S. 2006, ApJ, 132, 360

[Winkler et al. (2009)] Winkler, P. F., Twelker, K., Reith, C. N., & Long, K. S. 2009, ApJ, 692, 1489

[Wongwathanarat et al. (2013)] Wongwathanarat, A., Janka, H.-Th. & Muller, E. 2013, A&A, 552, 126

[Wongwathanarat et al. (2017)] Wongwathanarat, A., Janka, H.-T., Muller, E., Pllumbi, E. & Wanajo, S. 2017, ApJ, 842, 13

[Woosley & Weaver (1995)] Woosley, S. E. & Weaver, T. A. 1995, ApJS, 101, 181

[Woosley et al. (2002)] Woosley, S. E., Heger, A. & Weaver, T. A. 2002, RvMP, 74, 1015

[Yang et al. (2014)] Yang, X.-J., Liu, X.-Q., Li, S.-Y., & Lu, F.-J. 2014, RAA, 14, 1279

[Yamaguchi et al. (2014)] Yamaguchi, H., Badenes, C., Petre, R., et al. 2014, ApJ, 785, L27

Table 3.1. *Chandra* Observations of G292

ObsID	Date	Exposure (ks)	Roll Angle[a] (°)
6680[b]	2006 Sep 13	39	180
6678	2006 Oct 2	44	157
6679	2006 Oct 3	154	157
8447	2006 Oct 7	48	157
6677	2006 Oct 16	159	140
8221	2006 Oct 20	65	140

[a]The roll angle describes the orientation of the *Chandra* Observatory in the sky, as it is rotated about the viewing axis to optimally align its solar panels with the Sun.

[b]ObsID 6680 included two ACIS-S chips in addition to four ACIS-I chips. This observation was affected by telemetry saturation which reduced the exposure time by ∼25%. The 5 subsequent observations used the four ACIS-I chips only, and were not affected by telemetry saturation.

Table 3.2. Average CSM Abundances

$N_{\rm H}$ (10^{22} cm^{-2})	kT (keV)	$n_e t$ (10^{12} cm^{-3} s)	EM (10^{56} cm^{-3})	O	Ne	Mg	Si	S	Fe
$0.43^{+0.02}_{-0.02}$	$0.82^{+0.14}_{-0.03}$	$0.24^{+0.05}_{-0.03}$	$1.37^{+0.13}_{-0.16}$	$0.33^{+0.06}_{-0.03}$	$0.48^{+0.05}_{-0.03}$	$0.24^{+0.03}_{-0.02}$	$0.21^{+0.03}_{-0.02}$	$0.34^{+0.08}_{-0.08}$	$0.13^{+0.03}_{-0.02}$

Note. — Abundances are with respect to solar (Anders & Grevesse 1989). Uncertainties are at the 90% confidence level.

Table 3.3. Line and Continuum Energy Ranges for the EWI Images

Element/Ion	Line (eV)	Low[a] (eV)	High[a] (eV)
O Heα & Lyα (O VII & O VIII)	510 – 740	300 – 510	740 – 870
Ne Heα (Ne IX)	890 – 970	740 – 870	1120 – 1160
Ne Lyα (Ne X)	1000 – 1100	740 – 870	1120 – 1160
Mg Heα (Mg XI)	1290 – 1420	1250 – 1290	1620 – 1700
Mg Lyα (Mg XII)	1430 – 1510	1390 – 1430	1520 – 1630
Si Heα (Si XIII)	1750 – 1930	1620 – 1700	2020 – 2120
S Heα (S XV)	2300 – 2600	2000 – 2100	2610 – 2750
Fe Heα (Fe XXV)	6300 – 6850	5500 – 5900	6950 – 7250

[a]Low and high energy ranges used to estimate the underlying continuum.

Table 3.4. Estimated Ejecta Masses

Element	Entire SNR ($M_\odot$)	NW ($M_\odot$)	NE ($M_\odot$)	SE ($M_\odot$)	SW ($M_\odot$)	NW Hem.* ($M_\odot$)	SE Hem.* ($M_\odot$)
O	$0.47^{+0.23}_{-0.12}$	$0.13^{+0.06}_{-0.03}$	$0.09^{+0.03}_{-0.02}$	$0.08^{+0.05}_{-0.03}$	$0.08^{+0.05}_{-0.03}$	$0.20^{+0.09}_{-0.05}$	$0.17^{+0.10}_{-0.05}$
Ne	$0.57^{+0.18}_{-0.10}$	$0.16^{+0.04}_{-0.03}$	$0.10^{+0.02}_{-0.01}$	$0.08^{+0.03}_{-0.02}$	$0.11^{+0.05}_{-0.03}$	$0.27^{+0.07}_{-0.04}$	$0.19^{+0.08}_{-0.04}$
Mg	$0.13^{+0.04}_{-0.03}$	$0.06^{+0.02}_{-0.01}$	$0.04^{+0.01}_{-0.01}$	$0.03^{+0.01}_{-0.01}$	$0.04^{+0.02}_{-0.01}$	$0.10^{+0.02}_{-0.02}$	$0.07^{+0.03}_{-0.02}$
Si	$0.06^{+0.01}_{-0.01}$	$0.01^{+0.003}_{-0.002}$	$0.008^{+0.002}_{-0.001}$	$0.001^{+0.0001}_{-0.0001}$	$0.005^{+0.002}_{-0.001}$	$0.02^{+0.005}_{-0.004}$	$0.002^{+0.0006}_{-0.0006}$
S	$0.02^{+0.01}_{-0.01}$	$0.003^{+0.001}_{-0.001}$	$0.002^{+0.0003}_{-0.0003}$	0.0	$0.0003^{+0.0001}_{-0.0001}$	$0.005^{+0.001}_{-0.001}$	0.0
Fe	$0.03^{+0.01}_{-0.01}$	$0.008^{+0.003}_{-0.001}$	$0.005^{+0.001}_{-0.001}$	$0.003^{+0.002}_{-0.001}$	$0.005^{+0.003}_{-0.002}$	$0.01^{+0.004}_{-0.002}$	$0.008^{+0.004}_{-0.002}$
Total	$1.29^{+0.49}_{-0.28}$	$0.37^{+0.13}_{-0.07}$	$0.24^{+0.06}_{-0.04}$	$0.19^{+0.10}_{-0.06}$	$0.25^{+0.12}_{-0.06}$	$0.61^{+0.20}_{-0.11}$	$0.44^{+0.21}_{-0.12}$

Note. — Ejecta masses are in terms of $f^{1/2}d_6^{3/2}M_\odot$, where d_6 is the distance to the SNR in units of 6 kpc. The mass for the entire SNR is the sum of the six elemental masses calculated for all 1435 ejecta regions. The masses for the NW, NE, SE and SW quadrants and the NW and SE hemispheres are for regions where the given element's abundance was higher than the CSM abundance by at least a 3σ level of confidence.

Table 3.5. Estimated CSM Masses

Component	Mass ($M_\odot$)
Equatorial ring	$1.59^{+0.10}_{-0.14}$
Spherical CSM	$8.39^{+2.62}_{-0.86}$
Total	$9.98^{+2.72}_{-1.00}$

Note. — The masses are in terms of $f^{1/2}d_6^{3/2}M_\odot$, where d_6 is the distance to the SNR in units of 6 kpc. The "spherical CSM" includes all the regions with spectrally soft, diffuse emission projected across the face of the SNR, as well as CSM regions at the outer boundary.

Table 3.6. Average Ejecta Abundances

Region	O	Ne	Mg	Si	S	Fe
Entire SNR:	$1.63^{+0.05}_{-0.02}$	$2.63^{+0.03}_{-0.01}$	$1.24^{+0.01}_{-0.01}$	$0.84^{+0.01}_{-0.01}$	$1.55^{+0.06}_{-0.04}$	$1.26^{+0.07}_{-0.02}$
NW quadrant:	$1.82^{+0.09}_{-0.03}$	$3.18^{+0.06}_{-0.02}$	$1.47^{+0.03}_{-0.01}$	$0.89^{+0.02}_{-0.01}$	$1.74^{+0.10}_{-0.08}$	$1.51^{+0.15}_{-0.03}$
NE quadrant:	$1.43^{+0.05}_{-0.02}$	$2.44^{+0.04}_{-0.02}$	$1.12^{+0.02}_{-0.01}$	$0.96^{+0.03}_{-0.02}$	$1.64^{+0.10}_{-0.08}$	$1.54^{+0.08}_{-0.02}$
SE quadrant:	$1.75^{+0.17}_{-0.05}$	$2.38^{+0.14}_{-0.04}$	$1.20^{+0.05}_{-0.02}$	$0.65^{+0.11}_{-0.09}$	$1.35^{+1.08}_{-0.74}$	$0.83^{+0.21}_{-0.06}$
SW quadrant:	$1.51^{+0.09}_{-0.04}$	$2.22^{+0.05}_{-0.02}$	$1.08^{+0.02}_{-0.01}$	$0.68^{+0.02}_{-0.01}$	$1.16^{+0.08}_{-0.07}$	$0.78^{+0.09}_{-0.06}$
NW Hemisphere:	$1.68^{+0.06}_{-0.02}$	$2.76^{+0.04}_{-0.01}$	$1.29^{+0.02}_{-0.01}$	$0.87^{+0.02}_{-0.01}$	$1.63^{+0.06}_{-0.05}$	$1.63^{+0.11}_{-0.02}$
SE Hemisphere:	$1.56^{+0.08}_{-0.03}$	$2.42^{+0.06}_{-0.02}$	$1.16^{+0.02}_{-0.01}$	$0.65^{+0.03}_{-0.03}$	$0.92^{+0.13}_{-0.12}$	$0.82^{+0.07}_{-0.03}$

Note. — Abundances are with respect to solar (Anders & Grevesse 1989). Uncertainties are averages of the 90% confidence level uncertainties. The locations of the quadrants and hemispheres are shown in Fig. 11.

Table 3.7. Estimated Ejecta Masses - Shell Regions

Element	NW ($M_\odot$)	NE ($M_\odot$)	SE ($M_\odot$)	SW ($M_\odot$)
O	$0.10^{+0.05}_{-0.03}$	$0.06^{+0.02}_{-0.01}$	$0.04^{+0.02}_{-0.01}$	$0.02^{+0.01}_{-0.01}$
Ne	$0.13^{+0.03}_{-0.02}$	$0.07^{+0.02}_{-0.01}$	$0.05^{+0.02}_{-0.01}$	$0.05^{+0.01}_{-0.01}$
Mg	$0.05^{+0.01}_{-0.01}$	$0.02^{+0.005}_{-0.003}$	$0.02^{+0.006}_{-0.004}$	$0.02^{+0.004}_{-0.003}$
Si	$0.006^{+0.002}_{-0.001}$	$0.006^{+0.001}_{-0.001}$	$0.0004^{+0.0001}_{-0.0001}$	$0.005^{+0.001}_{-0.001}$
S	$0.002^{+0.001}_{-0.001}$	$0.001^{+0.0002}_{-0.0002}$	0.0	$0.0003^{+0.0001}_{-0.0001}$
Fe	$0.005^{+0.002}_{-0.001}$	$0.003^{+0.001}_{-0.001}$	$0.002^{+0.0003}_{-0.0004}$	$0.002^{+0.001}_{-0.001}$
Total	$0.29^{+0.10}_{-0.06}$	$0.16^{+0.04}_{-0.02}$	$0.11^{+0.05}_{-0.03}$	$0.10^{+0.03}_{-0.02}$

Note. — Ejecta masses are in terms of $f^{1/2}d_6^{3/2}M_\odot$, where d_6 is the distance to the SNR in units of 6 kpc. The masses are calculated for ejecta regions where the given element's abundance was higher than the CSM abundance by at least a 3σ level of confidence. Only regions projected between the estimated positions of the RS and CD (Bhalerao et al. 2015) are included in this table. These "shell" regions are shown in Fig. 13a.

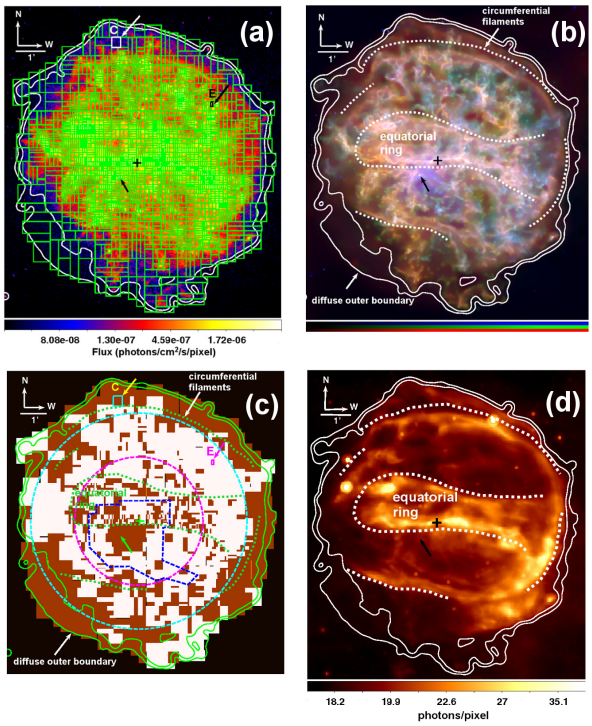

Figure 3.1 **(a)** ACIS-I broadband image of G292 (0.3-8 keV) overlaid with the 2147 regions (green boxes) made with our adaptive mesh method. Each region contains ∼5000 counts. White contours mark the outer boundary of the SNR in the X-ray band. The optical expansion center is marked with a cross (Winkler et al. 2009), and the pulsar (PSR J1124-5916) with an arrow. **(b)** ACIS-I three-color image of G292 (red = 0.3-0.8 keV, green = 0.8-1.7 keV and blue = 1.7-8.0 keV). White contours are the outer boundary of the SNR in X-rays based on the 0.3-8 keV band ACIS-I image. The black cross and arrow mark the positions of the optical expansion center and pulsar respectively as in Fig. 1a. The dashed curves mark the CSM features identified in X-ray and mid-infrared (Figs. 1c & d). **(c)** Ejecta and CSM map constructed based on measured abundances for O, Ne, Mg, Si, S and Fe. Ejecta-dominated regions are white, while CSM dominated regions are brown. Green contours are the outer boundary of the SNR. The cross marks the optical expansion center, and the green arrow marks the pulsar position. The overlaid dashed circles are our estimated locations of the reverse shock (RS, magenta) and contact discontinuity (CD, cyan), whose positions were inferred from radial velocity measurements of ejecta knots (Bhalerao et al. 2015). The green dashed curves highlight the locations of the thin circumferential filaments and equatorial ring which were previously identified as candidate CSM regions in X-ray (Gonzalez & Safi-Harb, 2003; Park et al. 2002, 2007) and infrared studies (Lee et al. 2009; Ghavamian et al. 2012). The blue-dashed line marks the location of the 312 PWN regions.**(d)** 24 μm *Spitzer* image of G292 (Ghavamian et al. 2012). The optical expansion center is marked with a black cross and the pulsar position with a black arrow. The white contours are the 0.3-8 keV band X-ray contours marking the outer boundary.

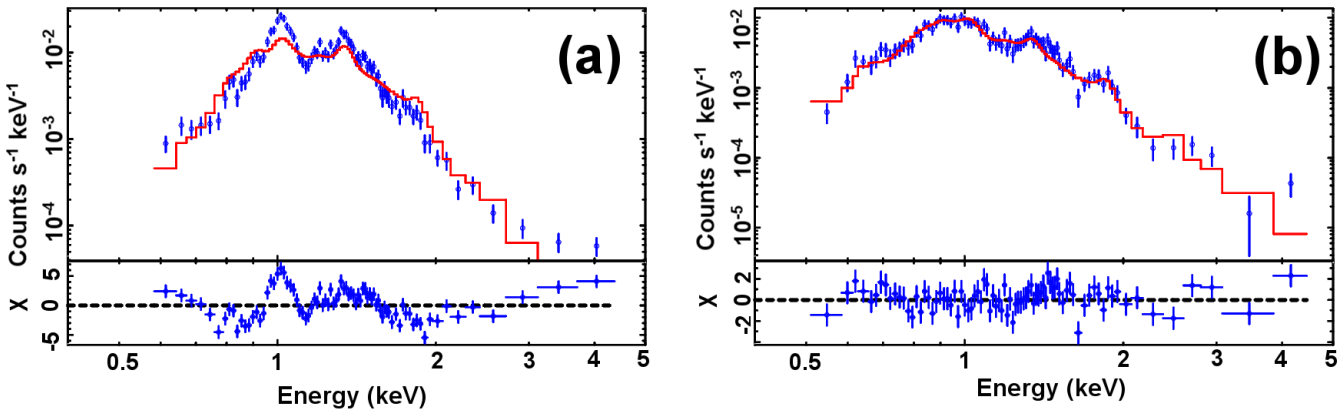

Figure 3.2 **(a)** An example spectrum of an ejecta region (region "E" marked in Figs. 1a & c), showing strong emission lines for Ne and Mg. The red line is the fitted plane shock model assuming CSM abundances. The large residuals (bottom panel) indicate a poor fit resulting in a high χ^2/ν value of 6.6 for this region. **(b)** An example spectrum of a CSM-dominated region near the outer boundary (region "C" marked in Figs. 1a & c) showing low abundances and thus giving a good fit ($\chi^2/\nu = 1.2$) to the CSM model.

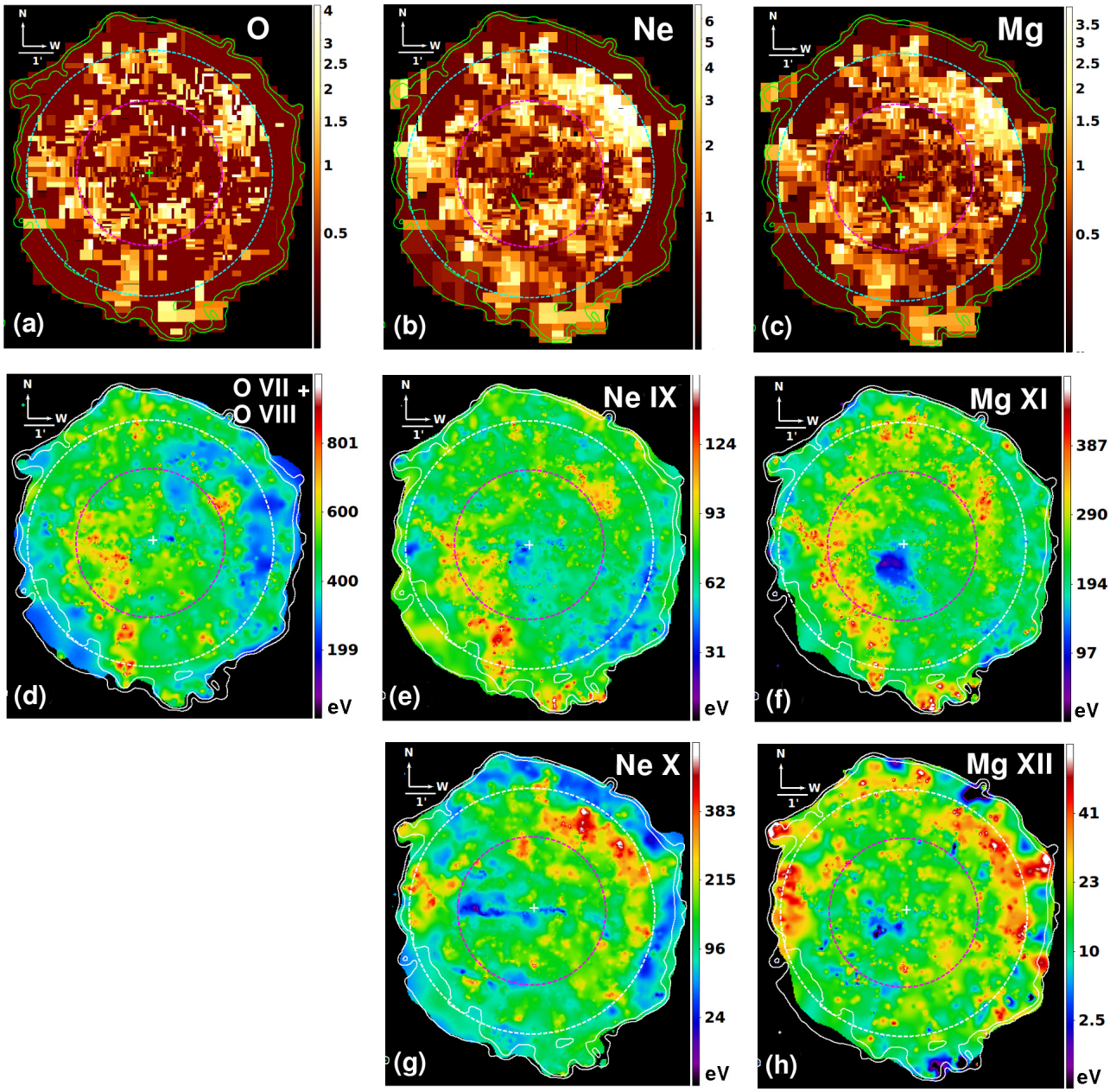

Figure 3.3 (continued on the next page)

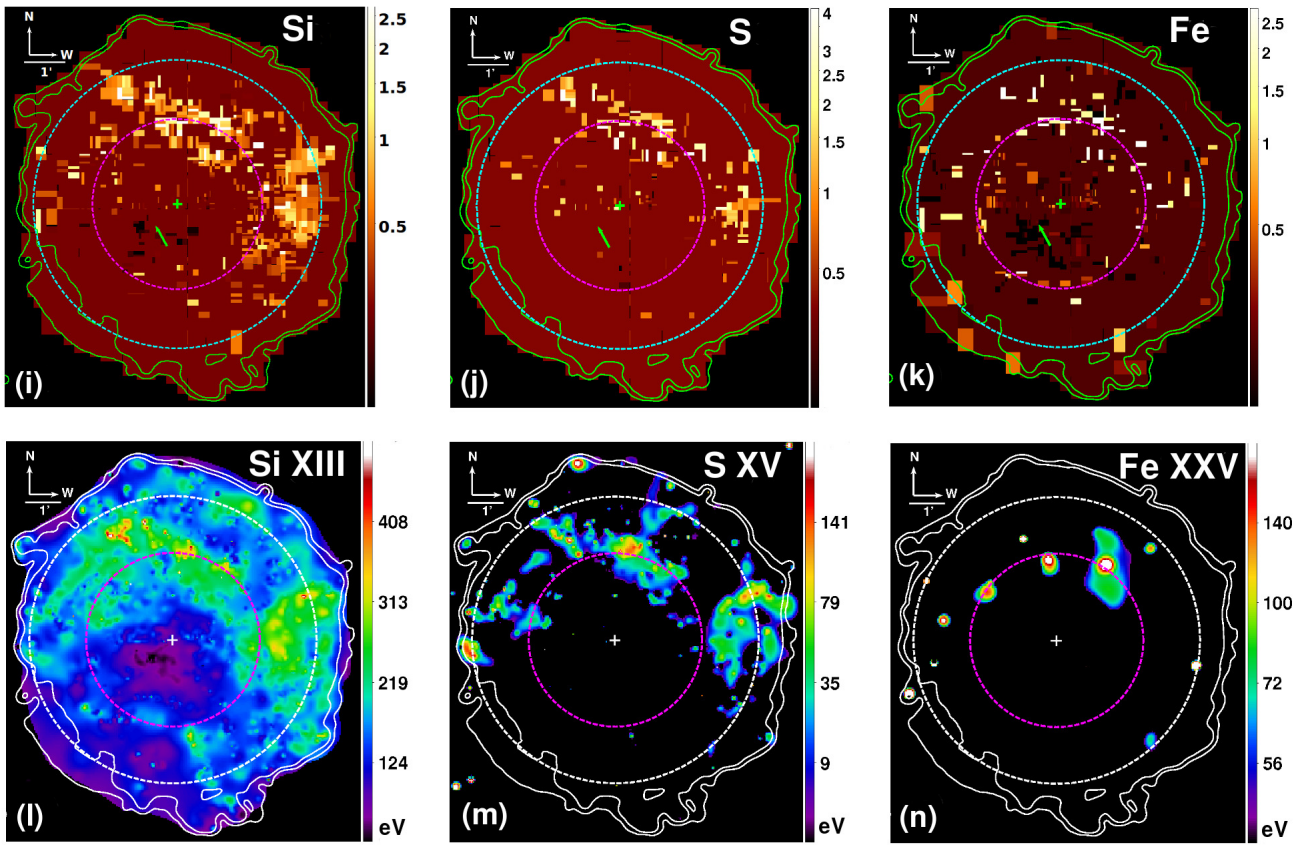

Figure 3.3 **Top panels (a, b, c, i, j & k):** O, Ne, Mg, Si, S and Fe abundances (in units of solar, Anders & Grevesse, 1989). The magenta and cyan dashed-circles represent the estimated locations of the RS and CD respectively (Bhalerao et al. 2015). The green contours mark the outer boundary of the SNR in the X-ray band. The cross marks the optical expansion center (Winkler et al. 2009), and the arrow marks the pulsar (PSR J1124-5916). **Lower panels (d, e, f, g, h, l, m & n):** O, Ne, Mg, Si, S and Fe line EW maps (including updated versions of those in Park et al. 2002 based on our deep ACIS-I data). The magenta and white dashed-circles represent the estimated locations of the RS and CD respectively.

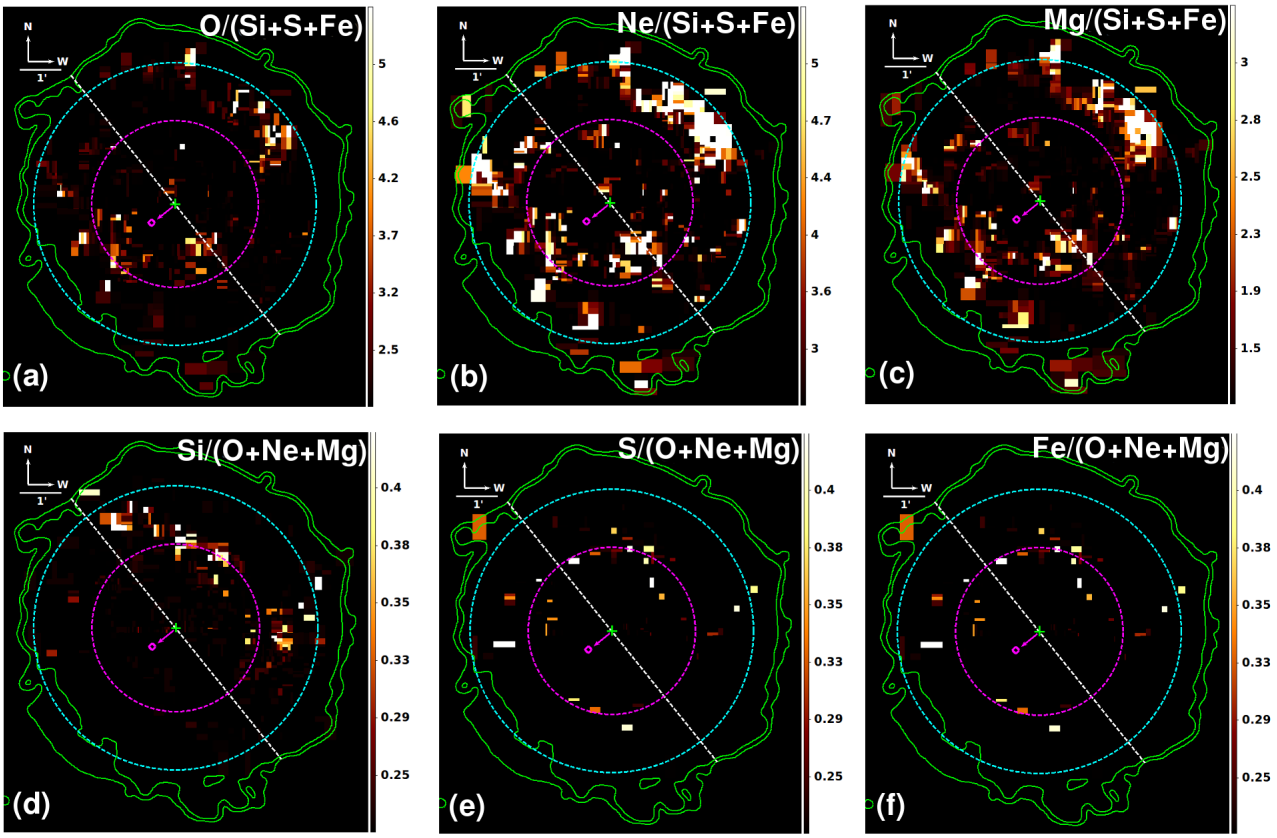

Figure 3.4 Abundance ratio maps for the *ejecta-dominated* regions. The green cross marks the optical expansion center (Winkler et al. 2009) and the magenta diamond marks the position of the pulsar. The magenta arrow indicates the direction of the pulsar's kick. The white dashed-line is perpendicular to the direction of the pulsar's kick and divides the remnant into the northwestern and southeastern hemispheres. The dashed magenta circle represents the estimated position of the RS, and the dashed-cyan circle represents the estimated position of the CD (Bhalerao et al. 2015). Green contours are the outer boundary of the SNR in X-rays based on the 0.3-8 keV band ACIS-I image.

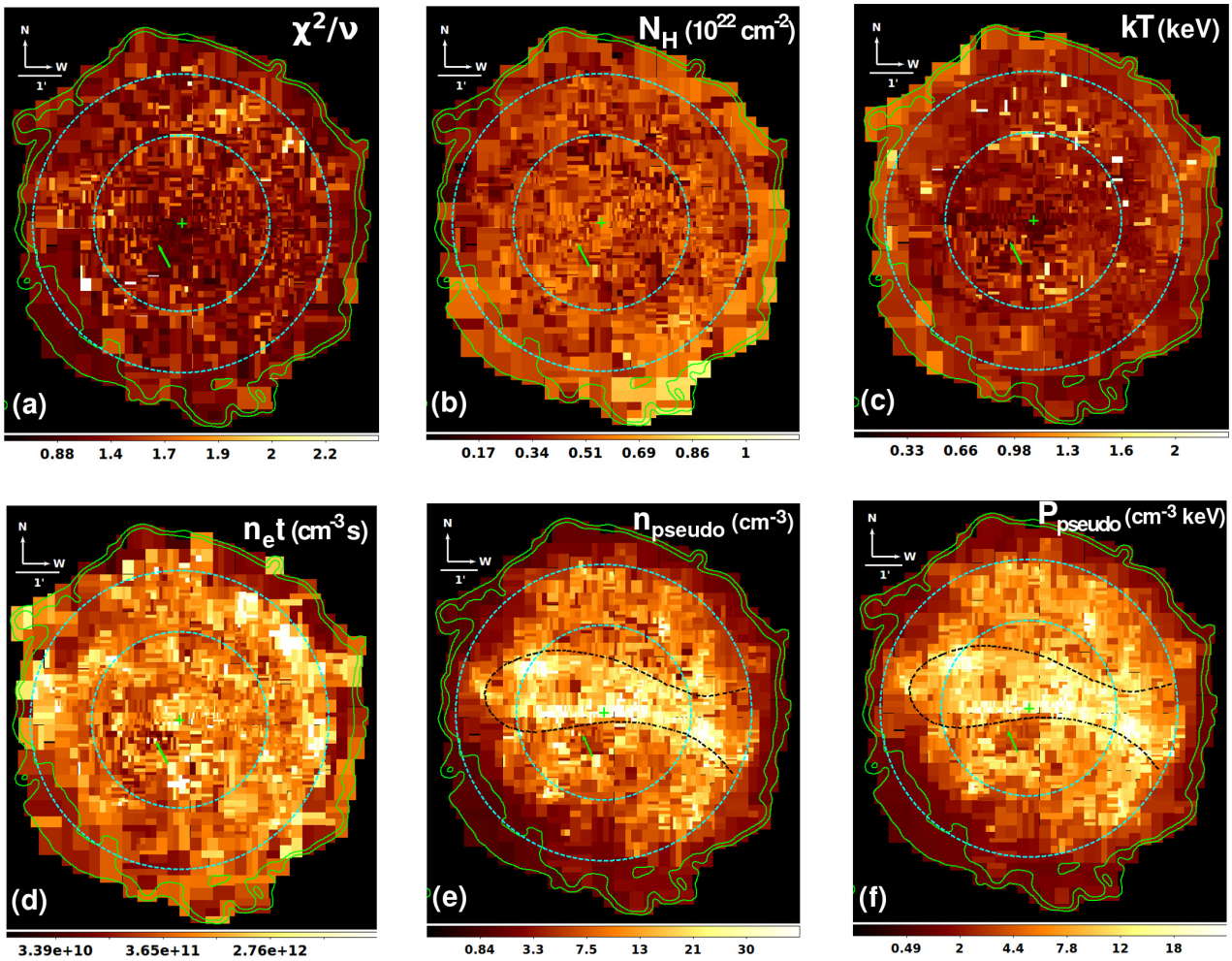

Figure 3.5 **(a):** Reduced chi^2 (χ^2/ν), **(b):** foreground column (N_H), **(c):** electron temperature (kT), **(d):** ionization timescale ($n_e t$), **(e)**: pseudo electron density (n_{pseudo}) and **(f):** pseudo thermal pressure (P_{pseudo}) distribution maps. For all these maps, the green contours mark the outer boundary of the SNR in the X-ray band, the green cross marks the optical expansion center, the green arrow marks the pulsar, the inner and outer cyan circles mark the estimated positions of the RS and CD respectively (Bhalerao et al. 2015).

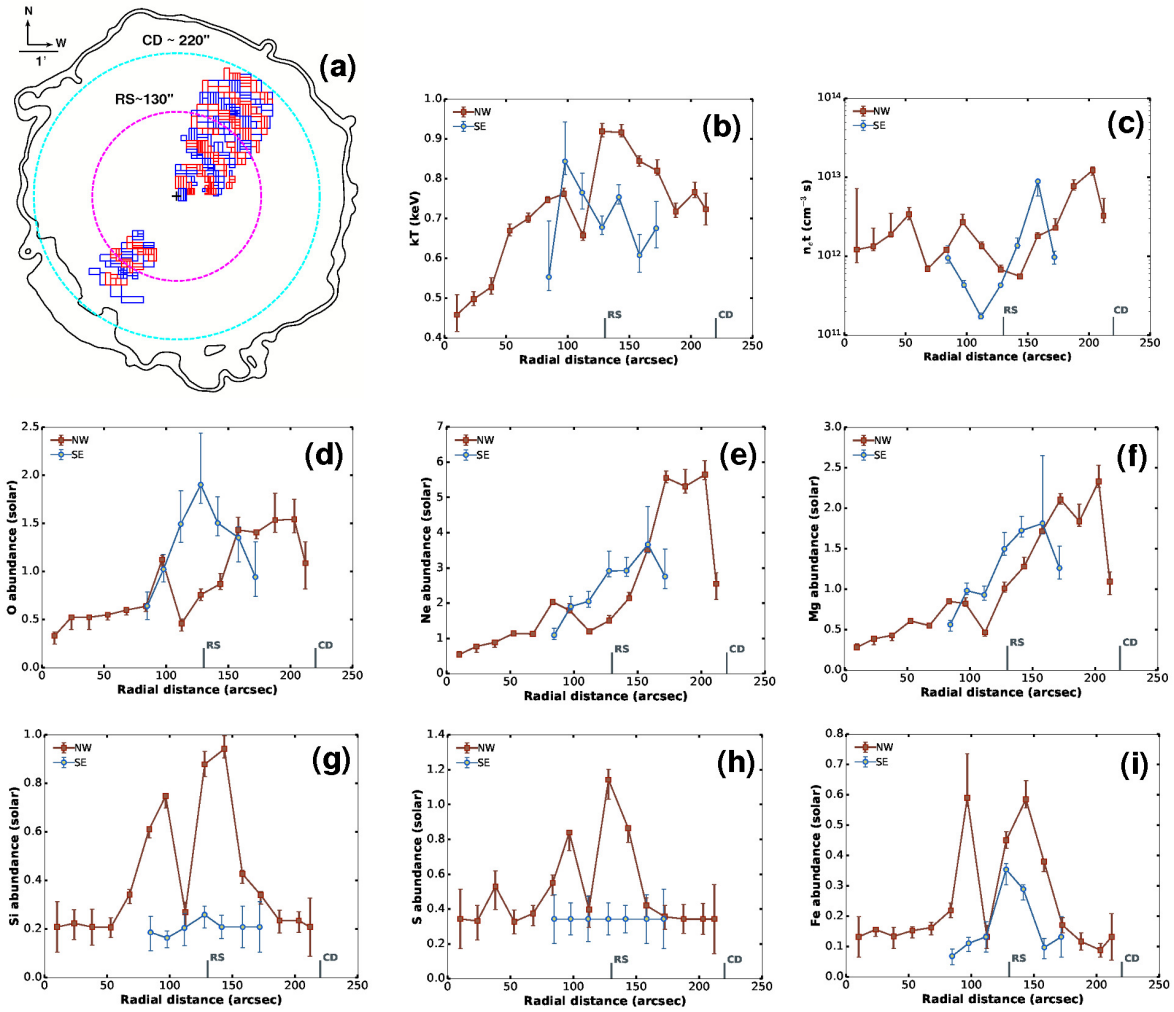

Figure 3.6 **(a)** Outline of G292 showing the ejecta regions used for making the radial profiles. The regions were divided into 15″ sections starting at the center and moving outwards radially. These sections are shown in alternating blue and red colors. Black contours are the outer boundary of the SNR in X-rays based on the 0.3-8 keV band ACIS-I image. The magenta and cyan dashed-circles represent the estimated locations of the RS and CD respectively based on the overall ejecta's kinematic structure in X-rays (Bhalerao et al. 2015). The positions of these loci are 1D approximations and their actual 3D positions may differ in different parts of the remnant. Average parameter values from each radial section are plotted against the distance from the expansion center (marked with a black cross). The NW regions are plotted in brown, and the SE regions in blue. The plotted parameters are: **(b)**: kT (keV), **(c)**: $n_e t$ (cm^{-3} s), **(d)**: O, **(e)**: Ne, **(f)**: Mg, **(g)**: Si, **(h)**: S & **(i)**: Fe abundance . The short vertical lines on the horizontal axes (labeled "RS" and "CD") represent the estimated locations of the RS and CD respectively.

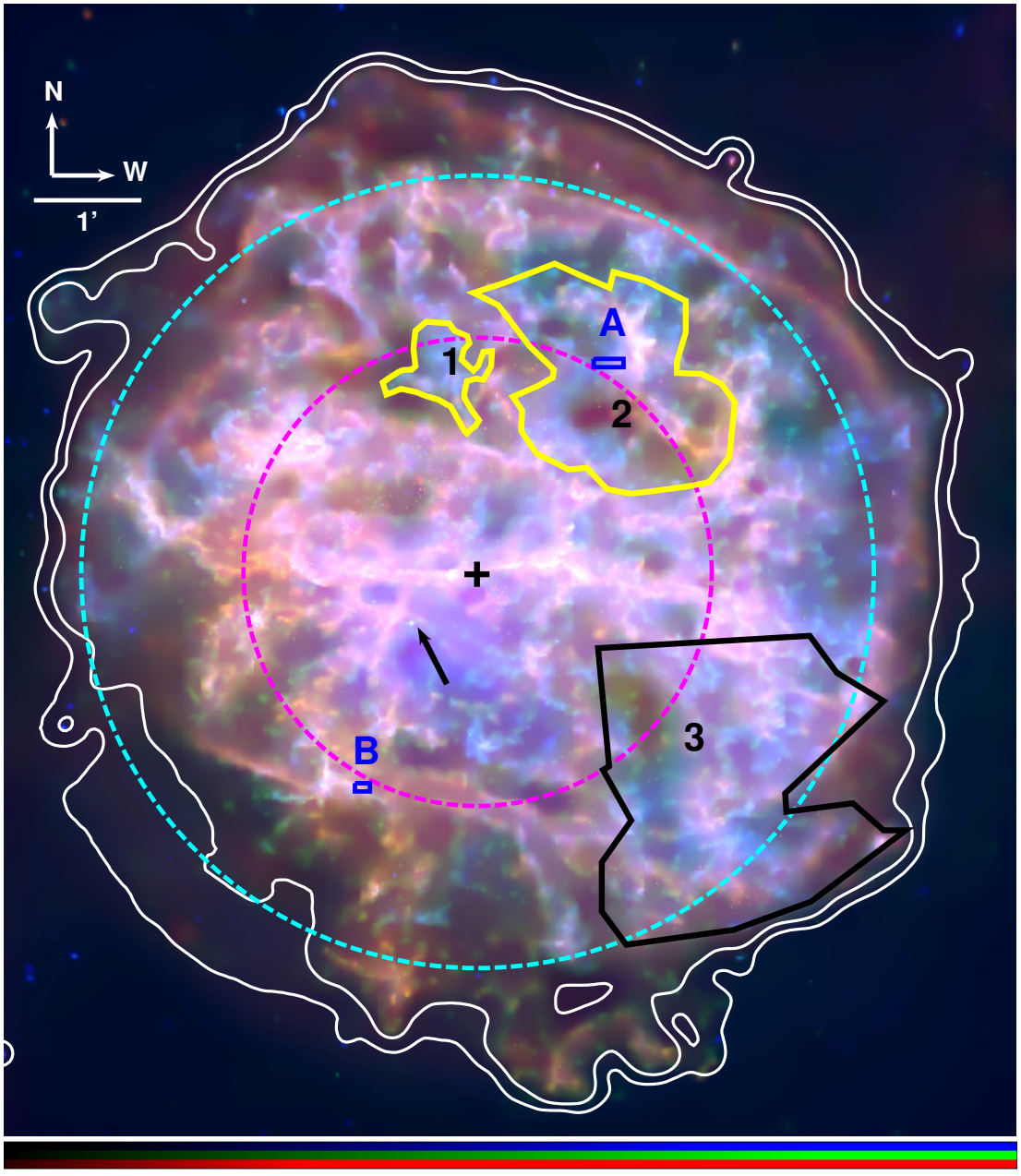

Figure 3.7 ACIS-I three-color image of G292 showing the extraction regions for detecting Fe emission. Red = 0.3-0.8 keV, green = 0.8-1.7 keV and blue = 1.7-8.0 keV. White contours are the outer boundary of the SNR in X-rays based on the 0.3-8 keV band ACIS-I image. The black cross and arrow mark the positions of the optical expansion center and the pulsar respectively. The dashed magenta circle represents the estimated position of the RS, and the dashed-cyan circle represents the estimated position of the CD (Bhalerao et al. 2015).

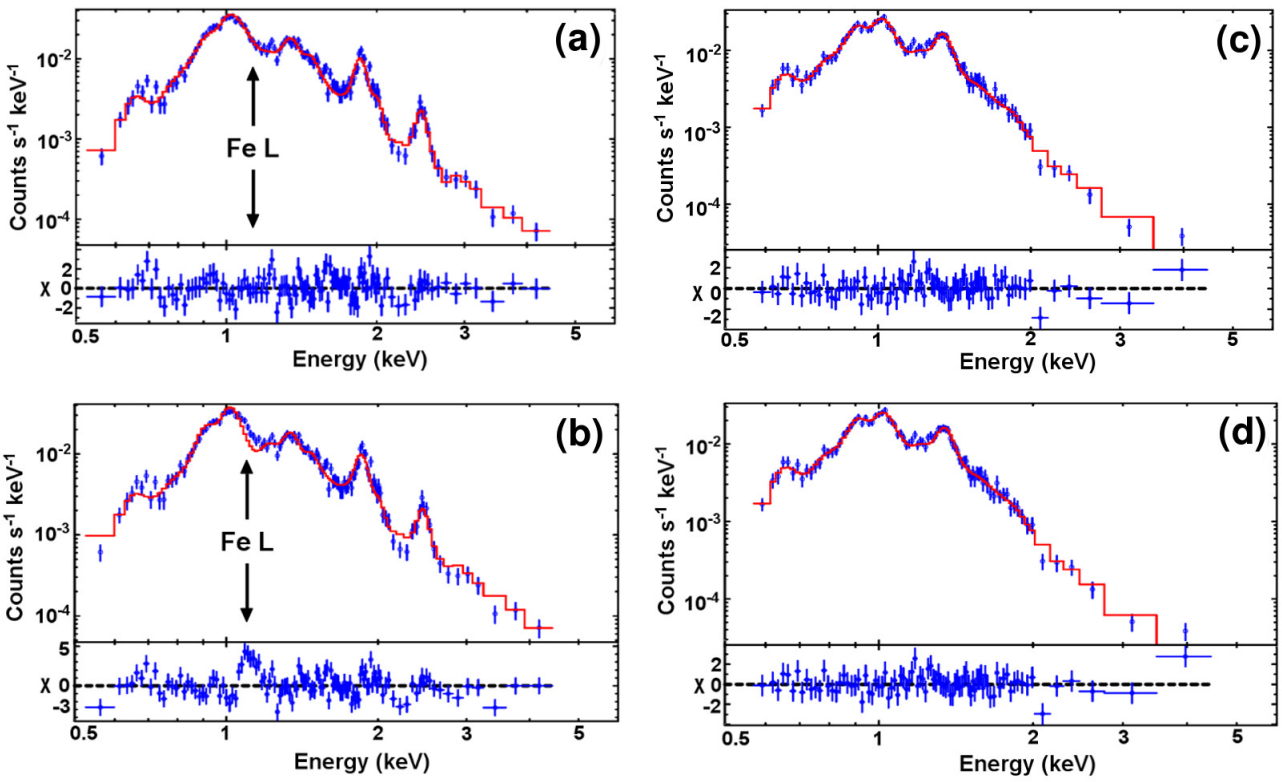

Figure 3.8 **(a & b)**: Spectral model fits to the X-ray spectrum of a small Fe-rich region (region A identified in Fig. 7). In (a) the Fe abundance is varied, and the best-fit value is $9.8^{+15}_{-7.0}\times$ solar). In (b), for comparison, we fixed the Fe abundance at the average CSM value (0.13× solar), resulting in large residuals at $E \sim 1.2$ keV for the Fe-L line complex. The abundances of the other elements (O, Ne, Mg, Si, S, Ar and Ca) are free and the abundance of Ni is tied to that of Fe in both model fits. The red line is the fitted plane shock model, the blue markers represent data. Fixing Fe increases χ^2/ν from 1.4 (a) to 2.4 (b). **(c & d)**: Spectral model fits to the X-ray spectrum of an Fe-poor region (region B in Fig. 7). In (c) we varied the Fe abundance, and the best-fit value is $0.25^{+0.29}_{-0.14}\times$ solar, which is consistent with the average CSM value. In (d), for comparisons, we fixed the Fe abundance at the CSM value (0.13× solar), which is not statistically distinguished from the model fit shown in (c).

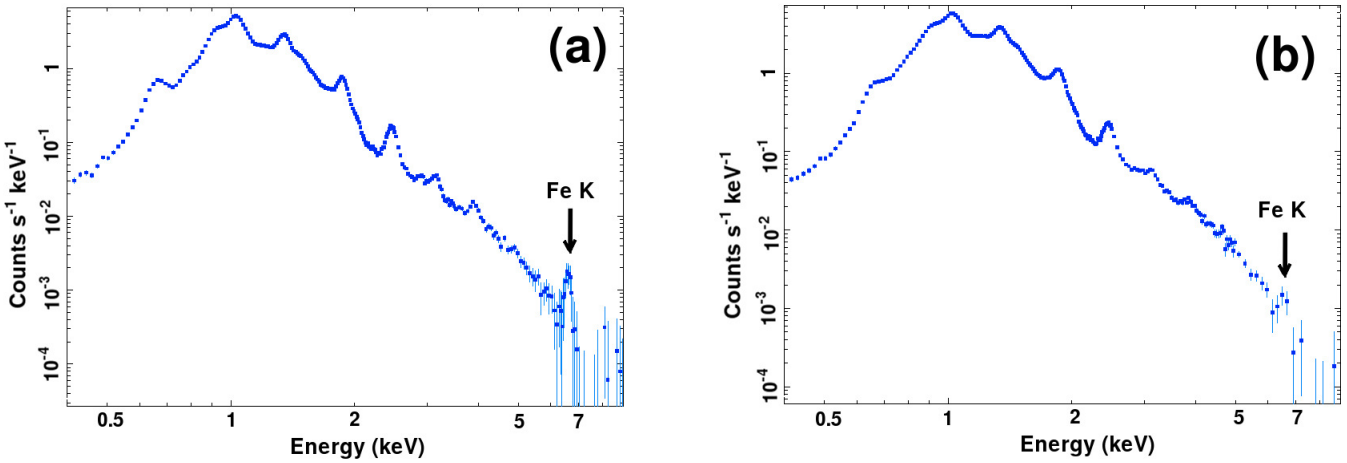

Figure 3.9 **(a):** X-ray spectrum extracted from the combined regions labeled 1 and 2 in Fig. 7 showing the Fe K-shell line at 6.6 keV. These two regions combined have a total of $\sim 1.2 \times 10^6$ counts. **(b)**: X-ray spectrum of an *ejecta-dominated* region in the southwest (region 3 in Fig. 7) in which the Fe K-shell line emission is negligible. This regional spectrum has $\sim 1.7 \times 10^6$ counts, which are comparable to those in Fig. 9a.

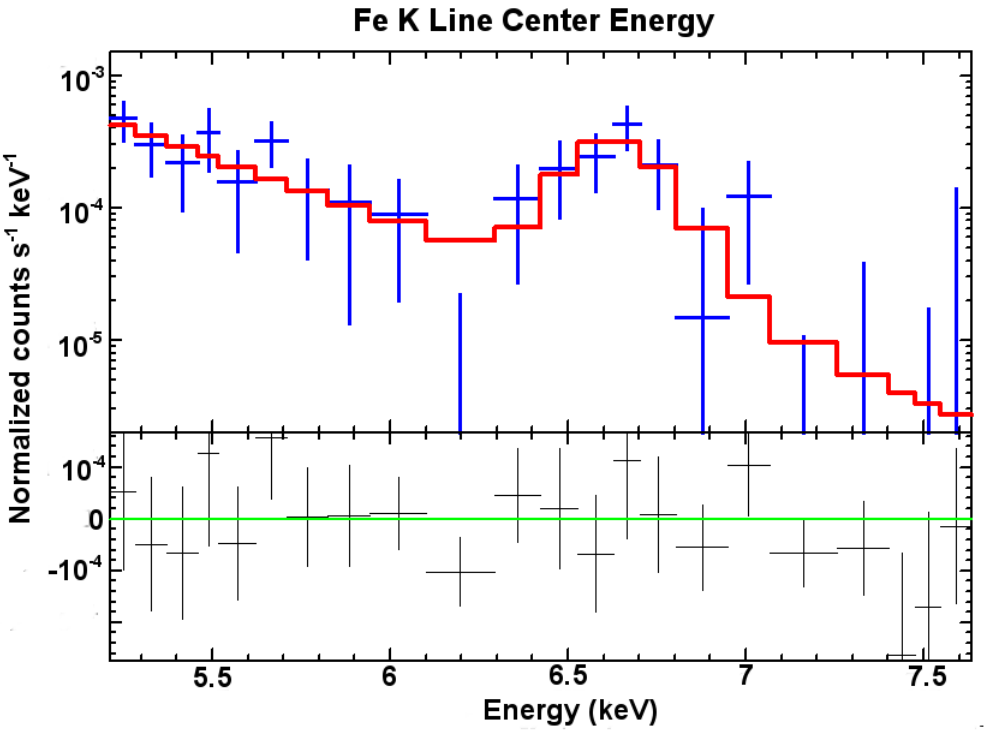

Figure 3.10 X-ray spectrum of 31 combined Fe-rich northern regions (seen as white boxes in Fig. 3k). The spectrum was binned at 20 counts per bin, and fitted with a Gaussian model. Data bins are in blue, and the model showing the fitted line center energy at 6.62 keV is in red. The bottom panel shows the residuals ($\chi^2/\nu \sim 1$).

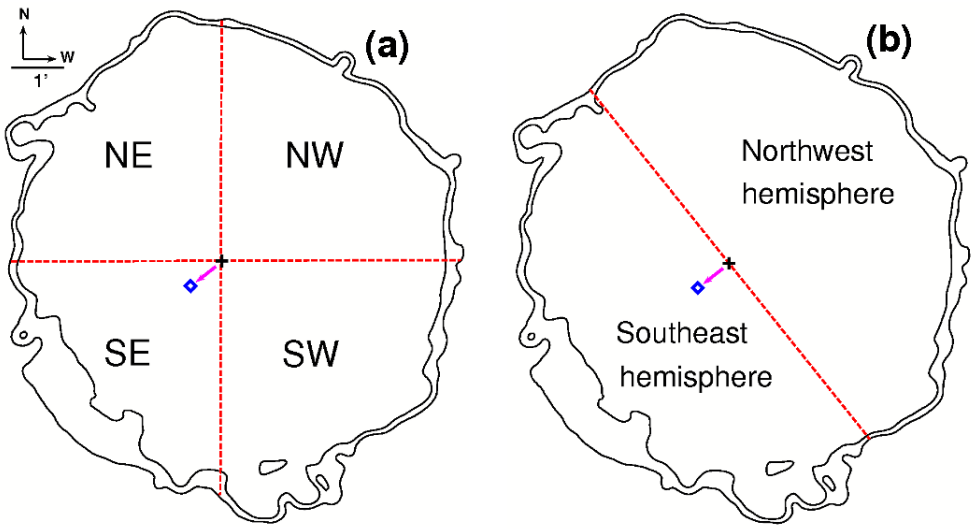

Figure 3.11 **(a):** Division of G292 into four quadrants: NW, NE, SE and SW **(b):** division of G292 into two hemispheres: the northwestern hemisphere, and the southeastern hemisphere to which the pulsar (PSR J1124-5916) has apparently been displaced. Black contours are the outer boundary of the SNR in X-rays based on the 0.3-8 keV band ACIS-I image. The black cross marks the position of the optical expansion center of the SNR (Winkler et al. 2009). The location of pulsar is shown by a blue diamond and the presumed direction of the pulsar's kick is shown by a magenta arrow. The red dashed-line dividing the northwestern and southeastern hemispheres is perpendicular to the direction of the pulsar's presumed kick.

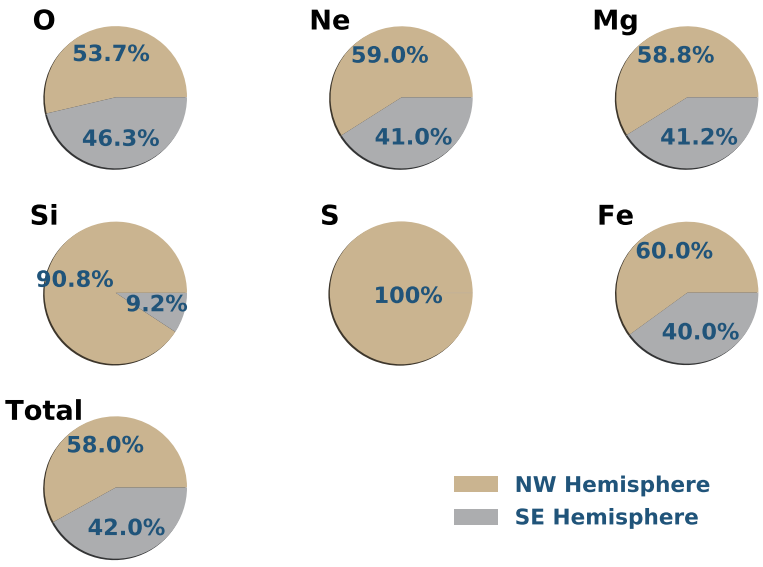

Figure 3.12 Pie charts showing the fractional distribution of ejecta masses for O, Ne, Mg, Si, S, Fe and the total of these six elements, between the northwestern hemisphere and the southeastern hemisphere (as shown in Fig. 11b). Ejecta regions that had the abundance of a given element greater than the CSM abundance by at least a 3σ confidence level were considered for this plot. The northwestern hemisphere dominates the southeast especially for Si, S, and Fe, where it accounts for $\gtrsim 60\%$ of the ejecta mass. The uncertainties in the mass fraction estimates are $\lesssim \pm 15\%$.

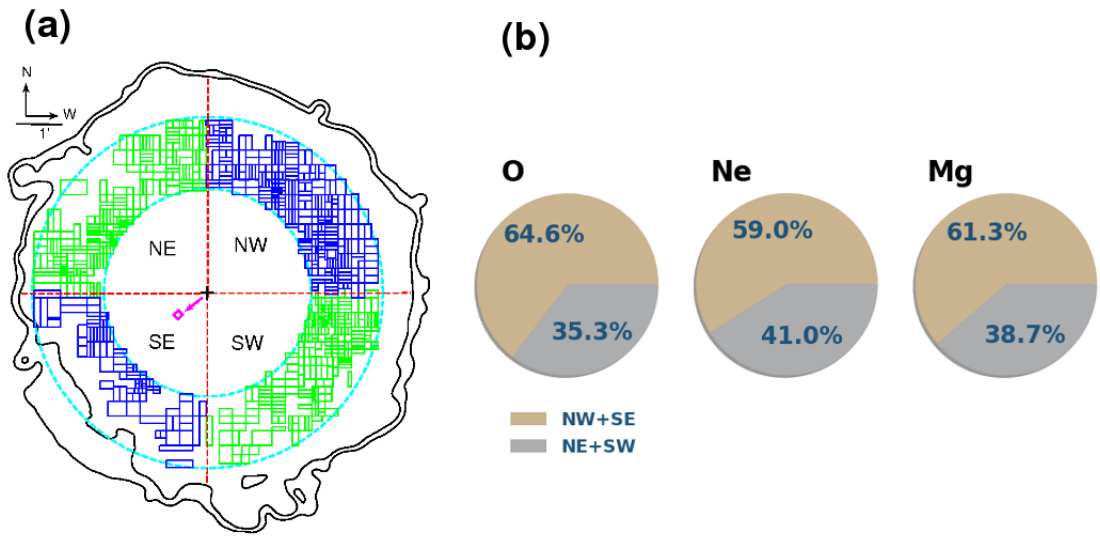

Figure 3.13 Pie charts showing the fractional distribution of ejecta masses for O, Ne and Mg between the combined NW and SE quadrants (blue regions in (a)), and the combined NE and SW quadrants (green regions in (a)). In order to exclude regions projected towards the central regions of the SNR, only ejecta regions between the estimated locations of the RS and CD (inner and outer dashed-cyan circles respectively) were used in this comparison. Ejecta regions that had the abundance of a given element greater than the CSM abundance by at least a 3σ confidence level were considered for this plot. The elemental ejecta masses for these "shell" regions are listed in Table 7. The uncertainties in the mass fraction estimates are $\lesssim \pm 20\%$.

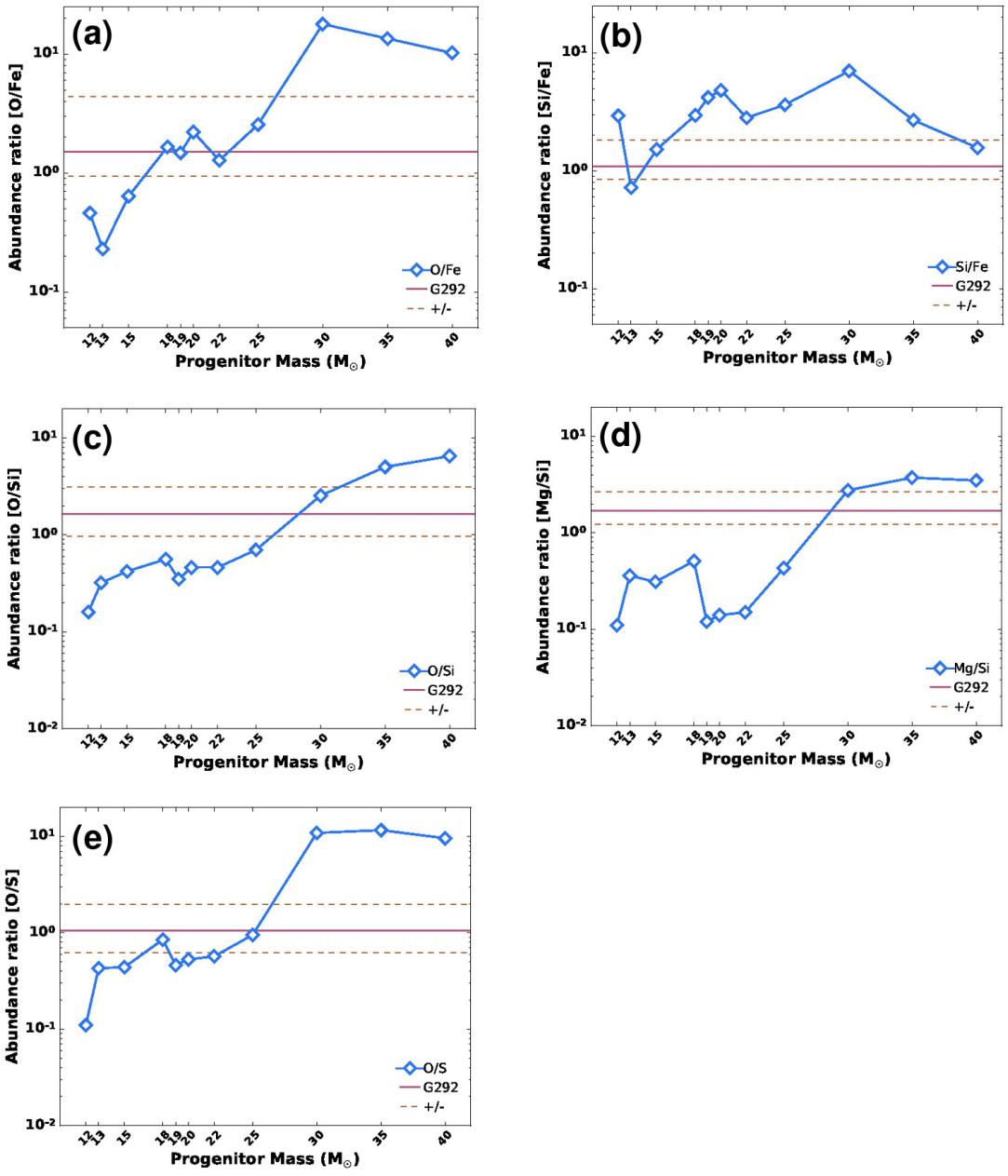

Figure 3.14 Average elemental abundance ratios for ejecta regions across the entire SNR (solid magenta line), compared to ratios predicted for CCSN nucleosynthesis models (blue curves, Woosely & Weaver 1995). The plots represent the abundance ratios: **(a)** O/Fe, **(b)** Si/Fe and **(c)** O/Si, **(d)** Mg/Si and **(e)** O/S. The dashed lines represent the uncertainties in the measured abundance ratios for G292. Only regions with abundances $>$ 1x solar, for both the elements in a given ratio, are considered when calculating these ratios.

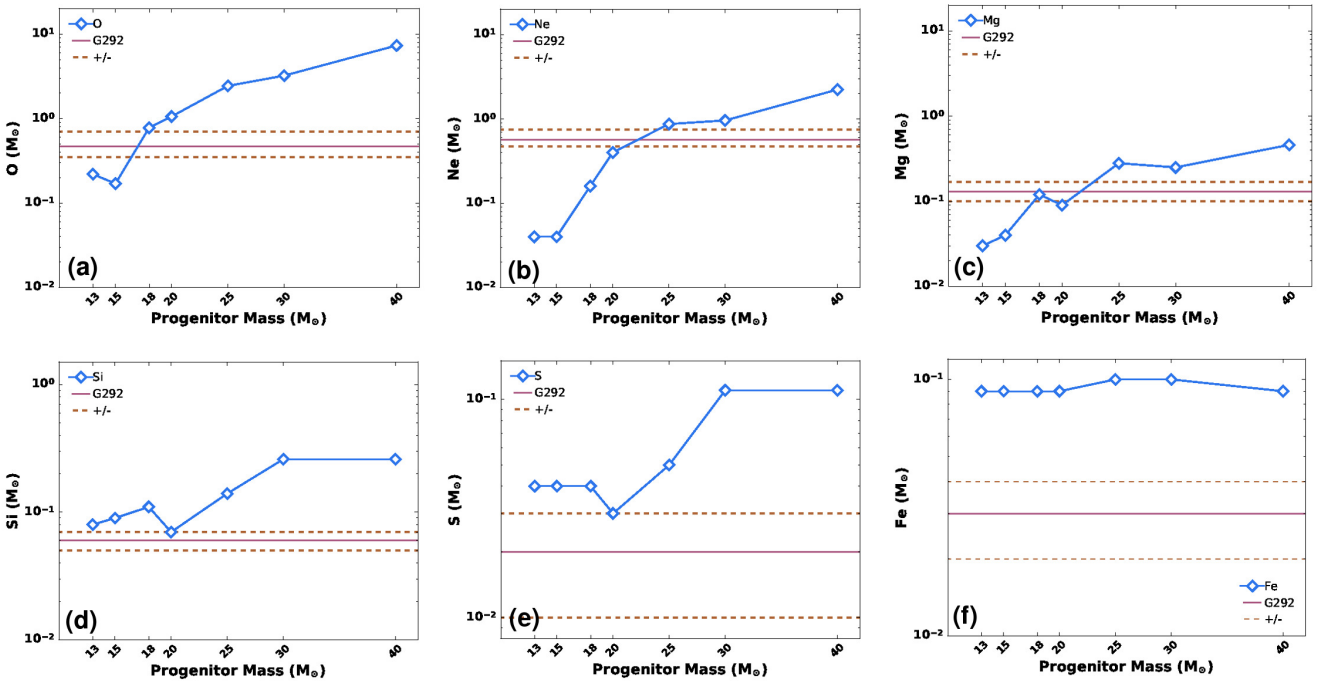

Figure 3.15 Elemental ejecta masses, estimated for ejecta regions across the entire SNR (solid magenta line) compared to yields predicted for CCSN nucleosynthesis models (blue curves, $Z = 0.02$, $E = 1{\times}10^{51}$ ergs, Nomoto et al. 2006). The estimated ejecta masses for G292 are in terms of $f^{1/2}d_6^{3/2}M_\odot$, where d_6 is the distance to the SNR in units of 6 kpc. The dashed lines represent the uncertainties in the estimated ejecta masses. The plotted elemental masses are **(a)** O, **(b)** Ne, **(c)** Mg, **(d)** Si, **(e)** S and **(f)** Fe.

CHAPTER 4

Summary & Conclusions

We present, in unprecedented detail, a comprehensive analysis of the Galactic core-collapse supernova remnant G292. We use data collected with the HETG grating spectrometer onboard NASA's *Chandra* X-ray Observatory (∼114 ks exposure), to probe the remnant's 3D-structure. We probe this 3D structure by measuring radial velocities (v_r) of its dense, localized, knot-like, emission features. We measure v_r in the range of -2300 $\lesssim v_r \lesssim$ 1400 km s^{-1} indicating a young, dynamically evolving remnant. We identify an asymmetry in the v_r-distribution of the ejecta. We detect a larger number of blueshifted-ejecta knots as compared to redshifted ones (∼70% of the ejecta knots are blueshifted). The blueshifted ejecta knots also have higher v_r magnitudes in general ($v_r > 1000$ km s^{-1}), than the redshifted ejecta knots.

Based on our measured v_r-distribution, we qualitatively locate the positions of the RS and CD at ∼130″(∼4 pc) and ∼220″ (∼6.4 pc) from the remnant's center respectively. The FS in G292 is at the outer boundary of the remnant at an angular distance of ∼ 265″(∼7.7 pc) from the center. Our deduced RS location is consistent with previous estimates in radio and infrared. Based on the remnant's dynamic evolution (RS/FS ratio and age ∼ 3000 yr), we place an upper limit to the total ejecta mass of $\lesssim$8 M$_\odot$. We also propose an upper limit to the progenitor mass of $\lesssim$ 35 M$_\odot$.

In the second part of this thesis, we perform a detailed analysis of G292 with our deep (530 ks) *Chandra* data collected using the ACIS-I detector. We apply our adaptive mesh method to perform a detailed "microscopic" exploration of the rem-

nant. With this method we divide the remnant into 2147 small rectangular regions, with a minimum of ∼5000 counts and an average area of ∼115 arcsec^2. We perform NEI plane-parallel shock model fits to spectra extracted from all of these small sub-regions. Our spectral analysis provides a detailed view of the structural, chemical and physical properties of the remnant. Based on our measured abundances of O, Ne, Mg, Si, S and Fe, we identify the spatial distribution of the ejecta and CSM in G292. We identify ∼1400 *ejecta-dominated* regions (regions with elemental abundances greater than the CSM value by at least a 3σ confidence level), and ∼700 *CSM-dominated* regions.

We present maps showing the detailed spatial distribution of the abundances of O, Ne, Mg, Si, S and Fe, the absorbing column (N_H), and the plasma physical parameters: electron temperature (kT), ionization timescale (n_et), and equivalents of the electron density (n_e), and thermal pressure (P). We identify the spatial distribution of Fe-rich ejecta in G292 using high-resolution *Chandra* data for the first time. Fe is a key explosive nucleosynthesis product, produced in the innermost regions of the progenitor star, and provides crucial insight into the SN explosion and its nucleosynthesis. We observe that the Fe is enhanced in the direction opposite to the pulsar's displacement. The Fe-rich ejecta regions locate close to the RS and generally trace its circular shape. This may suggest that the RS in G292 may not be significantly deformed and may retain an overall spherical structure. This also suggests that there could be more unshocked Fe-rich ejecta in the inner regions of the remnant.

Our abundance maps highlight an intriguing asymmetry in the spatial distribution of the ejecta in G292. The lighter O-, Ne- and Mg-rich ejecta appear to be enhanced in the northwest-southeast (NW-SE) direction. On the other hand, the heavier elements Si, S and Fe are almost exclusively enhanced in the NW with hardly any in the SE. These heavier elements are located in the direction opposite to the

associated pulsar's displacement. The pulsar (PSR J1124-5916) has been displaced $\sim$46″ from the center of the remnant, which corresponds to a transverse velocity of $\sim$440 km s^{-1}, and indicates a "kick" during the explosion. Our observed anti-alignment between the inner ejecta and the NS in G292 is consistent with theoretical predictions for the outcomes of hydrodynamically-induced NS-kicks.

In the northwest, O, Ne and Mg, are enhanced at larger projected radial distances than the Si-, S- and Fe-rich ejecta. This suggests "layering" of the ejecta in the northwest, with the lighter elements on the outside, likely preserving the original "onion-shell" nucleosynthesis configuration of the progenitor. The northwest also shows signs of progressive ionization by the RS. The highest ionization timescale ($n_e t$) values are found at larger radial distance just within our estimated location of the CD, followed by decreasing $n_e t$ values in the direction of the RS. Evidence for progressive ionization is also seen in our EWI maps where, in the northwestern and eastern parts of the remnant, line emission from higher ionization states of Ne and Mg (Ne X and Mg XII) is detected at larger projected radial distances than that from the lower ionization states (Ne IX and Mg XI).

Based on our maps, we for the first time identify the entire equatorial ring in X-rays, including its northern filaments. We estimate that the ring accounts for $\sim$16% of the total CSM mass and suggest that it may have originated from the equatorial winds of the progenitor. This substantial mass loss at the SNR's equator may have been caused by the rotation of the progenitor star, and/or from binary interactions.

By comparing our measured elemental abundance ratios and elemental ejecta yields to those predicted by standard CCSN nucleosynthesis models, we estimate a progenitor mass of 13 $M_\odot \lesssim M \lesssim 30\ M_\odot$.